Concepts from Non-Linear Dynamics and Statistical Physics Applied to Complex Networks in the Life Sciences

Dissertation zur Erlangung des Doktorgrades
der Fakultät für Mathematik und Physik
der Albert-Ludwigs-Universität Freiburg im Breisgau

vorgelegt von
Martin Peifer
Dezember 2006

Leiter der Arbeit: Prof. Dr. J. Timmer

Publications

1. H.H. von Grünberg, M. Peifer, J. Timmer, and M. Kollmann. Variations in substitution rate in human and mouse genomes. *Phys. Rev. Lett.,* 93:208102, 2004.

2. M. Peifer, B. Schelter, M. Winterhalder, and J. Timmer. Mixing properties of the Rössler system and consequences for coherence and synchronization analysis. *Phys. Rev. E,* 72:0262134, 2005.

3. B. Schelter, M. Winterhalder, J. Timmer, and M. Peifer. Testing for phase synchronization. *Physics Lett. A,* (accepted for publication).

4. M. Peifer and J. Timmer. Parameter estimation in ordinary differential equations for biochemical processes using the method of multiple shooting. *IET Proc. Systems Biology,* (accepted for publication).

5. M. Peifer, J. Timmer, and H.U. Voss. Non-parametric identification of non-linear oscillating systems. *J. Sound & Vib.,* 267:1157-1167, 2003.

6. H.U. Voss, M. Peifer, W. Horbelt, H. Rust and J. Timmer. Identification of chaotic systems from experimental data. In G. Gousebet, S. Meunier-Guttin-Cluzel, and O. Menard, editors, *Chaos and its Reconstruction,* pages 245-286. Nova Sciences Publishers, New York, 2003.

7. M. Peifer, B. Schelter, B. Guschlbauer, B. Hellwig, C.H. Lücking, and J. Timmer. On studentising and blocklength selection for the bootstrap on time series. *Biometrical J.,* 47:346-357, 2005.

8. B. Schelter, M. Winterhalder, M. Eichler, M. Peifer, B. Hellwig, B. Guschlbauer, C.H. Lücking, R. Dahlhaus, and J. Timmer. Testing for directed influences among neural signals using partial directed coherence. *J. Neuroscinece Meth.,* 152:210-219, 2005.

9. V. Petrov, M. Peifer, and J. Timmer. Bistability and self-oscillations in cell cycle control. *Int. J. Bif. & Chaos* 16,1057-1066, 2006.

10. V. Petrov, M. Peifer, J. Timmer Constructing a dynamical model of cell cycle control. *Comptes Rendus de l'Acad. Bulg. Sci.,* 57:15-22, 2004.

11. J. Karro, M. Peifer, R.C. Hardison, M. Kollmann, and H.H. von Grünberg. Neutral substitution rate variation in mammalian genomes and its relationship to GC isochores. *Genome Res.,* (under review)

12. M. Peifer, J. Karro, J. Timmer, R.C. Hardison, M. Kollmann, and H.H. von Grünberg. Quantifying neutral substitution rate variation across mammalian genomes. *Genome Res.,* (under review)

Conference Contributions

1. Variations in Substitution Rates in Human and Mouse Genomes, ISNB/ECCB 2004 Glasgow, Scotland.

2. Parameter Estimation in Signalling Pathways using Multiple Shooting, ISNB/ECCB 2004 Glasgow, Scotland.

3. Studentised Blockwise Bootstrap for Testing Hypotheses on Time Series, Compstat 2004, Prague, Czech Republic.

4. A Hybrid Optimization Method for Parameter Estimation is Systems Biology, Mathmod 2006, Vienna, Austria.

5. System Identification and Time Delays, Cosbics Workshop, Vigo, Spain.

6. Variation in Substitution Rate and GC Content in Mammalian Genomes, SBMC 2006, Heidelberg, Germany.

7. Testing for Phase Synchronization, Dynamics Days Europe 2006, Hersonissos, Greece.

Contents

1

Preface

A partial reversal of this bizarre partition of the world into the living and the nonliving came with the proofs that living forms are not, in fact, constant, but over the long range have evolved and that the family of this evolution can be traced.

Max Delbrück, Nobel Lecture

The enormous success of describing real-world phenomena with mathematical models becomes eminently apparent in physics. This success is due to the discovery of fundamental symmetries such as the Lorenzian invariance of the state space, local gauge symmetries, etc. which can be formulated in a mathematical precise way. The aim of theoretical concepts in physics is to reduce the complexity of observed phenomena to fundamental principles. However, this can only be achieved with an interplay of experiments and theory. Results from experiments may lead to a refinement of the theory, whereas theoretical predictions are often the driving-force for initiating new experiments. Limitations in either experimental or theoretical methods, in fact, hamper the identification of the underlying principles.

The separation of the world into the living and the unliving parts, as Max Delbrück notes in his Nobel lecture, arose during the Renaissance with the ascendance of physics as being science in our modern sense. In fact, it seems to be natural that the mode of describing the laws of nature significantly differs between the life sciences and physics. This difference can be expressed following J. Knight in [1] by: "Physics uses mathematics to represent the laws of nature; molecular biology relies on words and diagrams to describe the function of living things. The essence of physics is to simplify, whereas molecular biology strives to tease out the smallest details." With the foundation of molecular biology, about 50 years ago, the aforementioned separation of the world into the living and the unliving parts can be regarded as being obsolete. During the last decade, the accomplishment of genome sequencing for several species, the possibility of performing single cell measurements,

and the development of other high throughput measurement techniques offered an immense richness of detailed experimental facts to the life sciences. Like in physics, those experimental results have to be condensed into a comprehensive theory in order to uncover the underlying principles. Thus, out of the need for a mathematical theory, systems biology recently emerged as interdisciplinary field of research.

Since the complexity of living things is enormous, only an interdisciplinary approach is feasible to formulate a theory which is useful to disentangle the underlying principles. In detail, the rich experience of modelling complex systems can be obtained from physics, whereas new mathematical theory is provided by mathematicians. Most importantly, the background and the conductance of further experiments is devoted to the biologists. However, like each interdisciplinary approach, every participating discipline is enriched by the others with new ideas and concepts. The best example for this mutual enrichment is the strong interdisciplinary connection of mathematics and physics. For instance, the formulation of the theory of general relativity, on one side, heavily influenced the development of differential geometry. On the other side, the formulation of the Einstein equations would have been impossible without Riemannian geometry. Systems biology can thus be regarded as an attempt to attach the life sciences to the preexisting interdisciplinary conglomerate of mathematics and physics in order to tackle the complexity of life. Also essential for this endeavor, as noted in a recent editorial of Nature Cell Biology [2], is the interplay of experiments and theory.

In the following, concepts from statistical physics and nonlinear dynamics are consulted to develop theoretical methods for the life sciences. To this end, a route is chosen which leads from synchronization of macroscopic systems over biochemical reaction networks to the evolution of the DNA on a microscopic scale. In Chapter 2, concepts for synchronization analysis are developed. Synchronization of non-linear self-sustained oscillating systems not only occur in physics, as Josephson contacts in electromagnetic fields or organ pipes but increasingly many in life science. Here, prominent examples are the synchronous behavior of neurons in the brain or the synchronization of the circadian oscillator (day-night rhythm) with sun light, see e.g. [3]. The principle of synchronization is, in fact, an important concept for studying complex systems. If a mathematical description of two oscillating systems is given, synchronous behavior between these systems can often be derived analytically. However, in the case where only partial or no mathematical models are at hand, one would like to infer synchronization on the basis of measurements. For this purpose, a statistical test is derived in Chapter 2 using phase synchronization, which is the weakest type of synchronization and can be observed for deterministic as well as for stochastic systems. This offers the possibility to apply the derived test statistics for a wide range of data. The only limitation is that statistical dependencies have to vanish between distant phases in time of the underlying processes. This property is called mixing and is, beside ergodicity, one of the most important features of dynamical systems. A process where this mixing property is in doubt is the Rössler system. In Chapter 3, this system is examined in detail, where consequences for synchronization and spectral analysis resulting from a lack of mixing are discussed.

Biochemical reaction schemes can be represented by complex networks, graphs. Vertices of these graphs represent biochemical substances, whereas reactions between substances are

expressed by the edges. For example, an edge between vertex i and j shows that substance i is transformed to substance j by a biochemical reaction. However, these graphs are not static in time, but changing by the biological evolution. Of course, complex networks are not uniquely linked to biochemical reactions but can also be found throughout various scientific disciplines. In physics graphs arise naturally by the loop-expansion in quantum field theory or in statistical mechanics. Evolving networks, such as the biochemical reaction network, can be studied in the limit where the amount of vertices is infinite. In this limit, the degree distribution of a randomly chosen vertex is an important feature in graph theory. Here, the degree is defined by the number of edges leaving or approaching a vertex. Over an ensemble of randomly generated graphs, the degree distribution often scales like a power law. These graphs are called scale-free, where graphs which scale faster than a power law are called scale-rich. Based on a proposed measure which captures the interior statistical dependency structure of graphs, conditions for the emergence of scale-rich networks are derived in Chapter 4. The obtained results can be regarded as a first step toward a central limit theorem for random graphs and clarifies the predominant occurrence of scale-free networks.

From a biochemical reaction network, a mathematical model can often be formulated to describe the dynamics of the reactions itself using ordinary differential equations. Since chemical reactions of several proteins are too complex to be treated, e.g., with quantum chemistry, all of these models are phenomenological and contain unknown reaction rates. To validate and to predict the behavior of the models, the problem of estimating the unknown parameters arises. This leads to an optimization problem which in general contains multiple local optima. In Chapter 5, a parameter estimation method of ordinary differential equations is formulated which outperforms the standard approach in terms of convergence to the global optimum. In addition, the proposed method is numerically efficient; this offers the possibility to treat high dimensional systems. As an application, a biochemical signal transduction network is analyzed. The chosen system is of great importance, e.g., in medicine, since a dysfunction in this process may lead to the development of cancer. It is therefore an important component in order to understand the mechanisms of this disease.

The neutral rate of evolution in mammalian DNA is an important, but poorly understood, component of genomic structure. It is accepted that this rate is not constant over a genome, but varies across chromosomes and over time; characterization of this variation is thus invaluable in the study of genomic evolution, the identification of functional regions of the genome, and the development of further analysis tools. In Chapter 6, a new technique for analyzing the time-resolved pattern of the substitution rate variation across any mammalian genome is proposed. This analysis allows to trace the evolution of the substitution rate pattern for the last 150 million years, which also offers the possibility to study the conservation of the rate pattern. An inter-species comparison of the substitution rate variation and its relation to other genomic features sheds new light on the origin of this variation.

2

Testing for Phase Synchronization

2.1. Introduction

The field of nonlinear dynamics has brought various novel concepts, ideas, and techniques in order to analyze, and characterize complex dynamical systems. Synchronization analysis is one of these techniques which is designed to detect interactions between nonlinear self-sustained oscillators. Especially in physics and the life sciences, synchronization analysis has made its way into the daily routine in many investigations, e.g. [4, 5]. Following the pioneering work of Huygens, synchronization has been observed in a variety of different systems, ranging from processes exhibiting a limit cycle, via chaotic oscillators, to stochastic processes. For these systems, different types of synchronization have been observed, such as phase synchronization as weakest type of synchronization, lag synchronization, and complete synchronization [6-9]. Thereby, phase synchronization analysis has gained particular interest since it relies only on weak coupling between the oscillators. Different measures have been proposed to quantify phase synchronization [10-12]. The most frequently used measure is a measure based on entropy, the so called mean phase coherence which is based on circular statistics [13]. In fact, both measures quantify the sharpness of peaks in the distribution of the system's phase differences. In the this Chapter, we concentrate on the mean phase coherence.

The mean phase coherence is normalized such that it can only attain values in $[0, 1]$. A value of 1 indicates the highest state of phase synchronization. In spite of the necessity for a proper statistical assessment of the results obtained by phase synchronization analysis, hardly any work takes the statistical properties of the mean phase coherence into account. Due to the presence of noise on the data, either being observation noise or being dynamic noise, extreme values of zero and one are hardly observable. For a reliable application of phase synchronization analysis to empirical data, a statistical test is needed to decide whether the analyzed systems are in a state of synchronization or not. To this end, the calculation of

the distribution of the fluctuations superimposed to the mean phase coherence is desired for this statistical inference problem. Furthermore, the derived distribution should be as process unspecific as possible to achieve a high degree of applicability. Several approaches are possible that might be able to infer phase synchronization. Such an approach, e.g., might be realized to test for peaks in the distribution of the phase difference between both systems. This might be realized by comparing the distribution of the phase difference with a uniform distribution. The uniform distribution of the phase difference, however, is characteristic for unsynchronized systems. Deviations from this uniform distribution are due to the presence of phase synchronization. A statistical test to achieve this task might, e.g., be the Kolmogrov-Smirnov test [14]. Another alternative might, e.g., a test suggested by [15] which is based on the asymptotic distribution of the mean phase coherence. But for the latter two inference methods the test statistics is derived under the assumption of independent samples. Therefore, they are not expected to work properly in the case of dynamical systems or in other words, the process class for these tests is too small for our purpose.

In the following a theoretical approach utilizing the asymptotic properties of the estimator of the mean phase coherence is proposed. These theoretical considerations lead directly to a derivation of the distribution of the mean phase coherence under the hypothesis that the data generating processes itself are not phase synchronized. This distribution is necessary to build a statistical test for phase synchronization. It then allows detection of phase synchronization for a broad spectrum of data generating processes. Similarities to the test statistics presented in [16] are discussed. Finally, the performance of the derived test is studied in an application to stochastic synchronizing Rössler oscillators.

This Chapter is organized as follows. After the introduction of the mean phase coherence in Section 2.2, the methodology of statistical hypothesis testing is briefly described and alternative naïve tests that fail for our purposes are discussed in Section 2.3. Then the asymptotic distribution of the mean phase coherence under the hypothesis of absent phase synchronization is derived in Section 2.5. Due to the central limit theorem on functional spaces, the rigorous derivation of this distribution is possible for a wide range of data generating processes. The process dependent parameters that emerge during the derivation can be estimated from data in a numerical efficient way. This issue is addressed in Section 2.6, followed by the application of the proposed significance level to a coupled system of Rössler oscillators in Section 2.7.

2.2. Mean Phase Coherence

In order to detect phase synchronization between two coupled self-sustained oscillatory systems, a suitable definition of phase and amplitude of a real-valued observed signal is required. This can be realized if the considered oscillations are characterized by a narrow frequency band [17, 18]. Let $x(t)$ be the real-valued signal satisfying the mentioned property. The analytic signal is then given by

$$\psi(t) = x(t) + i\hat{x}(t) = A(t)e^{i\varphi(t)} \,, \tag{2.1}$$

where $A(t)$ is the amplitude and $\varphi(t)$ the phase. The imaginary part of the analytic signal can be obtained by the Hilbert transform [19]

$$\hat{x}(s) = \pi^{-1} \text{ P.V.} \int \frac{x(t)}{s-t}\, dt \tag{2.2}$$

of the signal, in which P.V. refers to Cauchy's principle value. The phase $\varphi(t)$ now yields a suitable basis for the synchronization analysis.

Phase synchronization of two coupled, oscillatory systems occurs if the $n : m$ phase locking condition is satisfied [6]

$$|n\varphi_x(t) - m\varphi_y(t)| = |\Phi_{n,m}| < const\ ,$$

where $\varphi_x(t)$ and $\varphi_y(t)$ denote the phases of the time series $x(t)$ and $y(t)$, respectively, and n, m are suitable integers. Since the phase is defined between $[-\pi; \pi]$ and in order to correct for phase jumps in the estimated phase which are induced by the presence of dynamical or observation noise, not the phase difference $\Phi_{n,m}$ itself but $\Psi_{n,m} = \Phi_{n,m} \mod 2\pi$ is investigated. A sharp peak in the distribution of $\Psi_{n,m}$ can be associated with a synchronized state between the oscillators. Here, a commonly used quantity, measuring the sharpness of the distribution of $\Psi_{n,m}$ is the mean phase coherence [13]

$$R^2_{n,m} = E\left[\cos(\Phi_{n,m})\right]^2 + E\left[\sin(\Phi_{n,m})\right]^2\ , \tag{2.3}$$

where $E[\cdot]$ denotes the expectation value. The mean phase coherence is $R^2_{n,m} = 1$ for a constant phase difference between the two processes and $R^2_{n,m} = 0$ for a uniformly distributed phase difference in case of non-synchronized oscillators. It has been shown that this quantity is considerably different from zero even in the case of weak coupling, which occurs in the case of phase synchronization.

Let ϕ_i, $i = 1, \cdots, N$ be equidistantly sampled data of $\Psi_{n,m}$, where the time span between the observations is Δt. For a discrete set of data points x_i an estimate of the Hilbert transform, Eq. (2.2), is given by the following procedure: let $\mathcal{F}, \mathcal{F}^{-1}$ denote the discrete Fourier transformation, and its reverse transformation. Moreover, $\theta(\cdot)$ represents the Heaviside function, being zero for all negative arguments and one for positive arguments. The empirical Hilbert transform can now be determined by calculating the Fourier transform of x_i, truncating the negative frequencies, and transforming twice the obtained process back into the time domain. This procedure can be formulated mathematically by

$$\psi_i = \mathcal{F}^{-1}\left\{2\ \theta(\omega)\ \mathcal{F}\{x\}(\omega)\right\}_i\ .$$

The above mentioned decomposition, Eq. (2.1), can be proceeded for ψ_i and yields the empirical process φ_i for the phase of the signal. For sake of simplicity we suppress the subscript n, m in the following. Assuming that underlying processes are ergodic it follows that the

phase difference ϕ_i is also ergodic. An estimate of R^2 in Eq. (2.3) is then given by

$$\begin{aligned}\hat{R}^2_N &= \left(N^{-1}\sum_{i=1}^{N}\cos(\phi_i)\right)^2 + \left(N^{-1}\sum_{i=1}^{N}\sin(\phi_i)\right)^2 \\ &= N^{-2}\sum_{i,j=1}^{N}\left(\cos(\phi_i)\cos(\phi_j) + \sin(\phi_i)\sin(\phi_j)\right) \\ &= N^{-2}\sum_{i,j=1}^{N}\cos(\phi_i - \phi_j)\ . \end{aligned} \tag{2.4}$$

In the following paragraph, the necessity and the procedure of statistical hypothesis testing is described. Two naïve approaches are discussed, where it is shown that they only yield useful results for small range of data generating processes.

2.3. Statistical Hypotheses Testing

The main scope of statistical hypotheses testing is to decide whether a hypothesis has to be rejected or not on the basis of measured data. Typically, hypotheses are questions like: Is the model consistent with the data or is there a difference of a certain quantity between two groups of measurements? In our case, the hypothesis is devoted to the problem if phase synchronization between two time series of oscillating systems is absent. To attack such questions on a quantitative way a usually real-valued quantity has to be defined assigning the N-dimensional vector of observations to a single number, where N denotes the size of the sample. Formally, the measurements are represented by a family of random variables $(X_i)_{i=1,\cdots,N}$ on the same space Ω. The desired quantity is therefore given by a map $\hat{t}_N$ with the following property

$$\hat{t}_N : \underbrace{\Omega \times \cdots \times \Omega}_{N-times} \to D \subset \mathbb{R}\ .$$

Since the space Ω is equipped with a probability measure P, the choice of $\hat{t}_N$ is restricted by the demand that $\hat{t}_N$ has to be measurable. This slight restriction is necessary to interpret the quantity $\hat{t}_N$ itself as being a random variable on D. Here, the random variable $\hat{t}_N$ is the statistic of the inference problem. Based on such a statistic, the hypothesis we like to address can be formulated in a probabilistic manner. For a given set $A \subset D$ the so called null hypothesis, denoted by H_0, is that the expectation value $E[\hat{t}_N]$ is an element of set A. Unfortunately, to decide whether the observed value of $\hat{t}_N$ satisfies the null hypothesis H_0 is problematic. This is due to the probabilistic character of $\hat{t}_N$. Consider, e.g., that $\hat{t}_N$ posses a continuous distribution with mass on the whole set D. This is exactly the situation we are confronted with when testing for phase synchronization. In that case a possible statistic is the mean phase coherence $\hat{t}_N = \hat{R}^2_N$, Eq. (2.4), which can take every value in $D = [0, 1]$. This leads to the situation that a rejection of the null hypothesis is not possible with certainty, which is due to the fact that $P^{H_0}_{\hat{t}_N}(D \cap [0, t]) \neq 1$ for every observed value t of $\hat{t}_N$. Here, $P^{H_0}_{\hat{t}_N}$

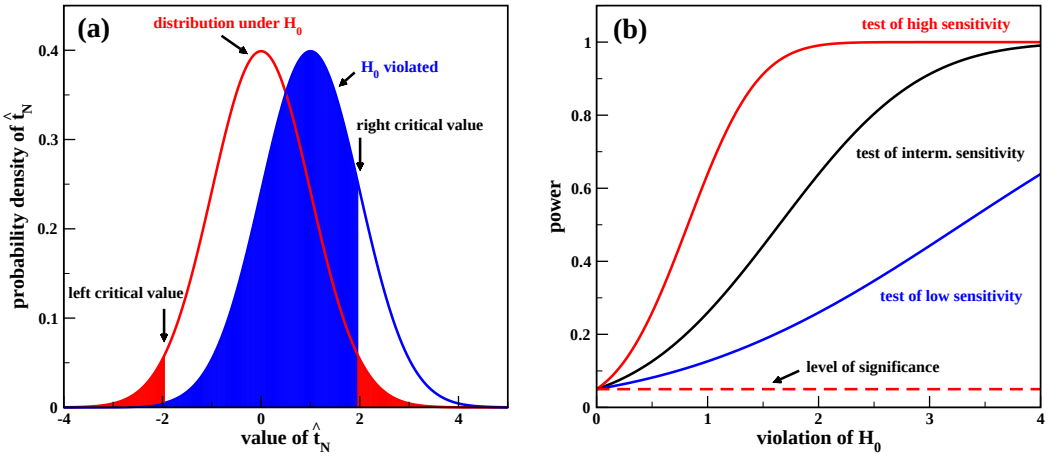

Figure 2.1: In this figure the characteristic quantities of a statistical test are illustrated. Here, the red curve in (a) shows the distribution of the statistic $\hat{t}_N$ for which the null hypothesis H_0 is valid. Indicated by a shift of the expectation value the blue curve represents the distribution of $\hat{t}_N$ whereas the alternate hypothesis H_1 is assumed to hold. The probability α to draw false positive conclusions from the test is shown by the red area of the red curve. This probability or level of significance is determined by the left and right critical values. In contrast, the blue area under the blue curve illustrates the probability β for making false negative conclusions under the alternative H_1. The right graph, (b), shows the power $1-\beta$ with respect to some violation of H_0. If no violation of H_0 is present the power coincides with the level of significance, displayed by the red dashed line. Moreover, the steepness of the power curve for small violations constitutes to the sensitivity of the test. Three exemplary power graphs of different sensitivity are shown by the red, black, and blue solid curves.

denotes the probability measure with respect to the statistic and under the assumption that the null hypothesis H_0 holds.

Providing a reliable and powerful method to decide whether to accept or to reject H_0 on the basis of empirical data, extreme values with considerably low probability are said to be not compatible with the null hypothesis. Therefore, a threshold has to be chosen separating the region for which the null hypothesis has to be rejected from the region where the null hypothesis is accepted. Depending on the problem a threshold on either the left, the right or both sides of the distribution of $\hat{t}_N$ has to be selected for this purpose. In our case a one-sided test is appropriate cutting off high values of $\hat{R}^2_N$, whereas the situation for a two-sided test displayed in Fig. 2.1a. The threshold is called critical value. Leaving out the improbable events leads to a non-vanishing probability that certain realizations are wrongly rejected. This so called error of first kind, false negative rate or level of significance is visualized by the red area in Fig. 2.1a, where the red curve represents the distribution of $\hat{t}_N$ if H_0 is valid. For a two-sided test the level of significance α can be determined from $P^{H_0}_{\hat{t}_N}$ by

$$\alpha = P^{H_0}_{\hat{t}_N}\left((\infty, t^l_{crit}] \cup [t^r_{crit}, \infty)\right) ,$$

where t^l_{crit}, t^r_{crit} is the left and right critical value. In general, not the critical value but the

error of first kind α is chosen in advance to set up the specificity of the test procedure. A central problem of statistical hypothesis testing is therefore devoted to the determination of the critical values for a given probability α. In the following, an approximation of the level of significance is derived for the mean phase coherence. Note that this task only requires the knowledge of the distribution of the statistic under the assumption that the null hypothesis holds, $P_{\hat{t}_N}^{H_0}$.

The term null hypothesis emphasizes that there also exists an alternative hypothesis. This alternate hypothesis is denoted by H_1 in the following. Clearly, the converse condition $E[\hat{t}_N] \notin A$ defines H_1. Apart from the behavior of the test under the null hypothesis its performance under the alternative hypothesis is also of practical importance. Here, the so called error of second kind β is the central quantity used to characterize the performance of the test under H_1. The error of second kind is defined as being the probability that the null hypothesis is accepted whereas it should have been rejected. Thus

$$\beta = P_{\hat{t}_N}^{H_1}\left([t_{crit}^l, t_{crit}^r]\right) , \tag{2.5}$$

where $P_{\hat{t}_N}^{H_1}$ is now the distribution of the statistic under the alternative hypothesis. In Fig. 2.1a, the blue curve exemplarily shows a distribution of $\hat{t}_N$ under H_1, visible by the shift of the expectation value to one. Here, the blue area represents the error of second kind given by Eq. (2.5). To incorporate both characterizations in one graph, the so called power of the test is introduced in the following. With respect to the violation of the null hypothesis the quantity $1-\beta$ is investigated for this purpose. The violation of the null hypothesis stated above is a distance measuring the degree of the departure from H_0. In case of the synchronization analysis this is, e.g., the distance of the "true" mean phase coherence from zero. The power $1-\beta$ is a probability and can therefore attain values in $[0, 1]$. Moreover, the power curve is usually a monotone function with respect to the violation of H_0, which should attain the level of significance if the null hypothesis is not violated. Three typical power curves are shown in Fig. 2.1b. As mentioned above the origin of each power curve is here the level of significance which was chosen to be 5%. However, the curves differ from the speed they rush up towards one with respect to the violation of H_0. This behavior characterizes the sensitivity of the test. For example, the red curve in Fig. 2.1b reaches values close to one for the lowest violation of the hull hypothesis and is therefore the most sensitive test with respect to the others. Instead, the black curve can be regarded as a test of intermediate sensitivity, whereas the blue curve represents a test of low sensitivity. A usual demand for a test statistics is that the sensitivity increases if the sample size N increases, since more information can be extracted out of the data. But keeping the sample size fixed, the sensitivity of the test can only be altered by its design.

In summary, a statistical test is characterized by the error of first kind if the null hypothesis H_0 holds and the power if the alternative hypothesis is valid. The first characteristic quantity determines the specificity of the test which has to be fixed prior the test procedure is applied. On the other hand, the second quantity is used to assess the sensitivity of the test. However, the power depends only on the sample size and the design of the statistical test. A graph visualizing both characteristics is the power diagram which will be used to assess the simulation study in Sec. 2.7.

2.4. Naïve Tests for Phase Synchronization

A first possible test procedure would be to check whether the empirical distribution of the phase difference is compatible with a uniform distribution. To this end, the so called Kolmogorov-Smirnov test [14] can be applied. The test statistics of the Kolmogorov-Smirnov test is based on the L^∞-distance between the (cumulative) empirical distribution function of the phase difference Ψ and the distribution function of the uniform distribution on $[0, 2\pi)$. Thus,

$$d_N^{KS} = \sup_{x\in[0,2\pi)} \left\{ |\hat{F}_N^\Psi(x) - (2\pi)^{-1}x| \right\}$$

is the desired test statistics, where $\hat{F}_N^\varphi(x) = N^{-1}\sum_{i=1}^N \theta(x-\Psi_i)$ is the empirical distribution function of Ψ and $\theta(\cdot)$ is again the Heaviside function. If the data points Ψ_i are statistically independent, then the asymptotic ($N \to \infty$) distribution of d_N^{KS} under $H_0 : d_N^{KS} = 0$ can be derived analytically. Now, we show the performance the described method in case of absent coupling between two stochastic Rössler oscillators [20]

$$\begin{aligned}
\dot{x}_{1,2} &= -\omega_{1,2}\, y_{1,2} - z_{1,2} + \sigma\ \eta_{1,2} \\
\dot{y}_{1,2} &= \omega_{1,2}\, x_{1,2} + a\, y_{1,2} \\
\dot{z}_{1,2} &= b + (x_{1,2} - c)\, z_{1,2}\,,
\end{aligned}$$

where the subscript 1 corresponds to system one and 2 represents system two. The influence of the dynamic noise is modeled by using Gaussian distributed random variables $\eta_{1,2} \sim \mathcal{N}(0,1)$. This leads to the a variance of σ^2 for the noise term $\sigma\,\eta_{1,2}$. The remaining parameters are set to $a = 0.15$, $b = 0.2$, $c = 10$, $\omega_{1,2} = 1 \pm 0.015$, $\sigma = 0.6$, and sampling rate is chosen to be 0.1. For the synchronization analysis only the x-components of the Rössler oscillators are examined. According to Sec. 2.2, the phases are estimated using the Hilbert transformation. The sample sizes are selected between 100 and 10^6 data points for each simulation. It turns out that the fraction of rejections of the null hypothesis was 100% for all simulations using the Kolmogorov-Smirnov test despite H_0 was fulfilled. As second possible test procedure, a strategy discussed in [16] can be considered. This method utilizes the asymptotic distribution of the mean phase coherence which is given by

$$2\ N\ \hat{R}_N^2 \approx \chi_2^2\,,$$

where χ_2^2 denotes the χ^2-distribution with two degrees of freedom. Again, in the derivation of this result it is assumed that the phase difference is independent. Using the same system and parameters as in the first case, the simulations yielded again 100% rejection of the null hypothesis. Since in both cases the null hypothesis was at any time rejected by the tests even though it was satisfied, the test procedures are not supposed to work. This is due to the rather unrealistic assumption that the phase differences are statistically independent. If the phase differences are statistically dependent, the rate at which the variance of $\hat{R}_N^2$ approaches zero is smaller than for a set of independent phase differences. Therefore, the false positive rate converges to one for $N \to \infty$. In following the distribution of the mean phase coherency is derived whereas the dependence structure of the phase differences for dynamical processes is explicitly implemented.

2.5. The Distribution of $\hat{R}_N^2$ under H_0

Formulating the phase-difference ϕ_i at time $t_i = i\,\Delta t$ as an increment process $\phi_i = \phi_{i-1} + \Delta\phi_i$, such that under H_0 the increments $\Delta\phi_i$ are strictly stationary. This holds for all sampling intervals Δt. Now, consider ϕ_i as a stochastic process and let us assume that the increments $\Delta\phi_i$ are representing an α-mixing process [21]. Precisely, let $\mathcal{F}_l^m = \sigma(\phi_l, \cdots, \phi_m)$ denote the smallest sigma-algebra such that all random variables $\phi_l, \cdots, \phi_m$ are measurable for some $0 \leq l \leq m$. The process ϕ_i is said to be α-mixing if the mixing coefficient

$$\alpha(k) = \sup_{l \geq 0} \sup \left\{ P(A \cap B) - P(A)P(B) : A \in \mathcal{F}_0^l,\ B \in \mathcal{F}_{l+k}^{\infty} \right\} \tag{2.6}$$

satisfies $\lim_{k\to\infty} \alpha(k) = 0$, where $P(\cdot)$ denotes the probability measure. In other words, the statistical dependencies are vanishing for infinitely distant events. Under this condition, it is possible to derive the asymptotic distribution of R_N^2 in the absence of phase synchronization. Moreover, in the following Chapter it is discussed that such a mixing condition is necessary for the inference of phase synchronization on the basis of empirical data. Similar to the usual central limit theorem, the phase increment process defined above converges to a Brownian motion. To this end, an appropriate metric process space is needed, which is explored in the following.

Assume that the process space is endowed with the Skorohod topology. The Skorohod topology is defined by the metric $d(\cdot,\cdot)$ on the space $\mathbb{D}[0,1]$ of cadlag functions on $[0,1]$. A cadlag function on $[0,1]$ is a real-valued function that fulfills

- $\lim_{s\uparrow s_0} x(s)$ exists for every $s_0 \in (0,1]$
- $\lim_{s\downarrow s_0} x(t) = x(s_0)$ exists for every $s_0 \in (0,1]$.

In general, we have to rescale the time t, i.e. $s = t/t_{\max} \in [0,1]$. Let Λ denote the class of strictly increasing continuous mappings of $[0,1]$ onto itself [22, 23]. Then, the distance $d(x,y)$ is the infimum of those positive ϵ for which there exists an $\lambda \in \Lambda$ with

$$\begin{aligned} \sup_{s\in[0,1]} \{|\lambda(s) - s|\} &\leq \epsilon \text{ and} \\ \sup_{s\in[0,1]} \{|x(s) - y(\lambda(s))|\} &\leq \epsilon \end{aligned}$$

for $x(s), y(s) \in \mathbb{D}[0,1]$. Then, the functional central limit theorem [24, 23] states that the sufficiently rescaled sum of the centered increments converge weakly to Brownian motion on $[0,1]$, i.e. there exist functions $\lambda_n \in \Lambda$ such that

$$\begin{aligned} \lim_{n\to\infty} x_n(\lambda_n(s)) &= x(s) \text{ and} \\ \lim_{n\to\infty} \lambda_n(s) &= s \end{aligned}$$

uniformly in s. Here, the sequence x_n converges weakly to the Brownian motion.

We can therefore replace the generally unknown evolution of ϕ by the following drift diffusion process

$$d\tilde{\phi}_t = \omega \; dt + \sqrt{D} \; dW_t \; , \tag{2.7}$$

where ω is the mean angular velocity of the phase difference, dW_t is the increment of the Brownian motion and D the diffusion constant. The phases ϕ_i can be approximated by $\phi_i \approx \tilde{\phi}_{i\Delta t} = \tilde{\phi}_t$ leading to the asymptotic distribution of $\hat{R}_N^2$ under the null hypothesis H_0. The procedure of estimating the coefficients ω and D from empirical data is addressed in Sec 2.6. Additionally, the initial distribution of $\phi_0 = 0$ with probability one can be assumed without loss of generality, since an over-all phase cancels out calculating the mean phase coherence. To determine the distribution $\hat{R}_N^2$ under H_0 the following random variables

$$X_N = N^{-1} \sum_{i=1}^{N} \cos(\phi_i) \quad \text{and} \quad Y_N = N^{-1} \sum_{i=1}^{N} \sin(\phi_i) \tag{2.8}$$

are considered. The solution of Eq. (2.7) is given by $\phi_i \sim \mathcal{N}(\omega t_i, D t_i)$, where $\mathcal{N}(\mu, \sigma^2)$ denotes the Gaussian distribution with mean μ and variance σ^2. Thus, for the phase model under H_0, Eq. (2.7), the expectation value of $E[X_N]$, $E[Y_N]$ yields

$$E[X_N] = N^{-1} \sum_{j=1}^{N} \cos(\omega t_j) \; e^{-\frac{D}{2} t_j} \quad \text{and} \quad E[Y_N] = N^{-1} \sum_{j=1}^{N} \sin(\omega t_j) \; e^{-\frac{D}{2} t_j} \; , \tag{2.9}$$

where $t_j = j\Delta t$. The latter expressions are due to following identity

$$\frac{1}{\sqrt{2\pi}\sigma} \int \big(\cos(x), \sin(x) \big) \; e^{-\frac{(x-\mu)^2}{2\sigma^2}} \; dx = \big(\cos(\mu), \sin(\mu) \big) \; e^{-\frac{\sigma^2}{2}} \; . \tag{2.10}$$

Expressing $\cos(\omega t_j)$ and $\sin(\omega t_j)$ by their polar representations and evaluating the geometric sums $\sum_{j=1}^{N} (\cdot)^j$ in Eq. (2.9) leads to

$$E[X_N] = \frac{1}{N} \left(\frac{f(t_1) - f(t_N) + e^{-D\Delta t} \; (f(t_{N-1}) - 1)}{(1 - e^{-D\Delta t/2})^2} \right) = O(N^{-1}) \quad \text{and}$$

$$E[Y_N] = \frac{1}{N} \left(\frac{g(t_1) - g(t_N) + e^{-D\Delta t} \; g(t_{N-1})}{(1 - e^{-D\Delta t/2})^2} \right) = O(N^{-1})$$

with $f(t_j) = \cos(\omega t_j) \; e^{-\frac{D}{2} t_j}$ and $g(t_j) = \sin(\omega t_j) \; e^{-\frac{D}{2} t_j}$. Especially the fact that $E[X_N] = O(N^{-1})$ and $E[Y_N] = O(N^{-1})$ is important for approximating the covariance matrix of the random vector $Z_N = (X_N, Y_N)$.

The covariance matrix of Z_N can be calculated using $\mathrm{C} = \mathrm{Cov}(Z_N) = E[Z_N' Z_N] - E[Z_N'] E[Z_N]$, where Z_N' indicates the transposition of Z_N. Since $E[Z_N] = O(N^{-1})$, C can be

approximated by its second moment with a remainder of order N^{-2}. Thus, $\mathrm{C} = \mathrm{Cov}(Z_N) = E[Z_N' Z_N] + O(N^{-2})$ and we obtain

$$\mathrm{C} = N^{-2} \sum_{i,j=1}^{N} \begin{pmatrix} E[\cos(\phi_i)\cos(\phi_j)] & E[\cos(\phi_i)\sin(\phi_j)] \\ E[\cos(\phi_i)\sin(\phi_j)] & E[\sin(\phi_i)\sin(\phi_j)] \end{pmatrix} + O(N^{-2}) \,. \tag{2.11}$$

Expansion of the diagonal entries of the covariance matrix yields that the corresponding expectation values can be represented by $\frac{1}{2}\big(E[\cos(\phi_i - \phi_j)] \pm E[\cos(\phi_i + \phi_j)]\big)$. The sum in Eq. (2.11) contains the case where $i = j$. This occurs for N combinations. Since the summand $E[\cos(\phi_i - \phi_j)] = 1$ if $i = j$, it dominates the sum in C for the diagonal entries, from which follows that $\mathrm{C} = O(N^{-1})$ and therefore $N \cdot \mathrm{C} \to \tilde{\mathrm{C}} \neq 0$. Hence, it is indeed guaranteed that Eq. (2.11) can be approximated by neglecting the term of order $O(N^{-2})$.

Since $\cos(\phi_i)$ and $\sin(\phi_i)$ are strongly mixing sequences, the central limit theorem for mixing processes [25] holds and, therefore, $\sqrt{N} \cdot Z_N$ converges in distribution to the bivariate normal distribution

$$\sqrt{N} \cdot Z_N \xrightarrow{d} \mathcal{N}(0, \tilde{\mathrm{C}}) \quad \text{as} \quad N \to \infty \,. \tag{2.12}$$

Furthermore, C is positive definite and symmetric, we can decompose $\mathrm{C} = \mathrm{QDQ}'$, where Q is orthogonal and D is diagonal. Since D is diagonal and positive, $\mathrm{D}^{\frac{1}{2}}$ is well defined by the square root of the the diagonal entries. Setting

$$\tilde{Z}_N \mathrm{D}^{\frac{1}{2}} \mathrm{Q}' = Z_N \tag{2.13}$$

it follows that $\tilde{Z}_N = (\tilde{X}_N, \tilde{Y}_N) \sim \mathcal{N}(0, \mathbb{1})$ for $N \to \infty$. This is due to the following assertions: the positive definiteness guarantees that the inverse $(\mathrm{D}^{\frac{1}{2}}\mathrm{Q}')^{-1}$ exists. Hence, $\tilde{Z}_N = (\mathrm{D}^{\frac{1}{2}}\mathrm{Q}')^{-1} Z_N$ and by Eq. (2.12), $E[\tilde{Z}_N] \to 0$ for $N \to \infty$. Moreover, $E[\tilde{Z}_N' \tilde{Z}_N] = E[Z_N'(\mathrm{QDQ}')^{-1} Z_N] = E[Z_N' \mathrm{C}^{-1} Z_N] \to \mathbb{1}$. Since the first and the second moment coincides with the moments of the standard normal distribution and the space of Gaussian distributed random variables is closed with respect to linear transforms, we can state from Eq. (2.12) that indeed $\tilde{Z}_N \xrightarrow{d} \mathcal{N}(0, \mathbb{1})$. According to Eq. (2.4), and by the definition of Z_N we can represent the estimator of the mean phase coherency by $\hat{R}_N^2 = Z_N Z_N' = ||Z_N||^2$. Inserting Eq. (2.13) in the previous expression, we obtain $\hat{R}_N^2 = \tilde{Z}_N \mathrm{D} \tilde{Z}_N'$. This leads to the equivalent expression

$$\hat{R}_N^2 = \lambda_1 \tilde{X}^2 + \lambda_2 \tilde{Y}^2 \,,$$

where λ_1, λ_2 are the eigenvalues of C, given by

$$\lambda_{1/2} = \frac{\mathrm{tr\ C}}{2} \pm \sqrt{\frac{(\mathrm{tr\ C})^2}{4} - \det \mathrm{C}} \,. \tag{2.14}$$

Consequently, the eigenvalues λ_1, λ_2 determine the asymptotic distribution of the mean phase coherence under H_0. The distribution of $\hat{R}_N^2$ can therefore be approximated by a superposition of two independent χ^2-distributions with one degree of freedom, χ_1^2, which is the

distribution for the square of a normally distributed random variable. Since $\lambda_{1/2} > 0$, we can further estimate an upper limit of this distribution by

$$\hat{R}_N^2 \approx \text{tr C} \cdot \chi_1^2 \,. \tag{2.15}$$

Critical values derived from the upper limit are therefore too large for a given level of significance α. In consequence, the true error of first kind, as discussed in Sec. 2.3, is smaller than the predefined. This leads to a test which is known as being conservative. For such tests, a certain proportion of significant results are overseen, which is tolerable in contrast to the opposite behavior where too much effects are detected. In Sec. (2.7) we demonstrate that the derived test statistics, however, still has enough power for discriminating the phase synchronized state from the unsynchronized state. Furthermore note, that for independent realizations with $\lambda_1 = \lambda_2$ the distribution yields

$$\hat{R}_N^2 \approx \frac{\chi_2^2}{2N} \,, \tag{2.16}$$

which is exact the distribution suggested in [16].

To obtain the asymptotic distribution in the general case, e.g., for non-independent but mixing phase differences, the trace of the covariance matrix given by Eq. (2.11)

$$\begin{aligned} \text{tr C} &= N^{-2} \sum_{i,j=1}^{N} \left(E[\cos(\phi_i)\cos(\phi_j)] + E[\sin(\phi_i)\sin(\phi_j)] \right) \\ &= N^{-2} \sum_{i,j=1}^{N} E[\cos(\phi_i - \phi_j)] \end{aligned} \tag{2.17}$$

has to be calculated to estimate the asymptotic properties of $\hat{R}_N^2$ under H_0. For the diffusion process, Eq. (2.7), the distribution of the phase difference $\phi_i - \phi_j$ is normally distributed with mean $\omega|t_i - t_j|$ and variance $D|t_i - t_j|$. Due to Eq. (2.10) we therefore obtain,

$$\text{tr C} = N^{-2} \sum_{i,j=1}^{N} e^{-\frac{D}{2}|t_i - t_j|} \cos(\omega|t_i - t_j|) = \frac{1}{N} + \frac{2}{N} \sum_{s=1}^{N-1} \left(1 - \frac{s}{N}\right) e^{-\frac{D}{2}t_s} \cos(\omega t_s) \,.$$

Abbreviating $\xi = e^{-\frac{D}{2}\Delta t + i\omega\Delta t}$ and $f(t_j) = e^{-\frac{D}{2}t_j} \cos(\omega t_j)$, we have

$$\begin{aligned} \text{tr C} &= N^{-1} \left(\frac{1}{2} + \xi \frac{1 - \xi^{N-1}}{1 - \xi} - \xi \frac{1 - \xi^{N+1}}{N\,(1-\xi)^2} + \frac{\xi^N}{1 - \xi} \right) + c.c. \\ &= N^{-1} \left(1 + 2\, \frac{f(t_1) + f(t_N) - e^{-D\Delta t}}{(1 - e^{-D\Delta t/2})^2} \right) + O(N^{-2}) \,, \end{aligned}$$

where *c.c.* is referred to as the complex conjugation of the previous expression. Therefore the distribution of estimated mean phase coherence assuming that the null hypothesis holds can be approximated by

$$\hat{R}_N^2 \sim N^{-1} \left(1 + 2\, \frac{f(t_1) + f(t_N) - e^{-D\Delta t}}{(1 - e^{-D\Delta t/2})^2} \right) \chi_1^2 \,. \tag{2.18}$$

We have to keep in mind that this approximation is only accurate for a large sample size N. To obtain a sufficient approximation of the distribution of $\hat{R}_N^2$ under H_0, the mean angular velocity ω and the diffusion constant D have to be reliably estimated. This task is subject of the following section.

2.6. The Estimation of ω and D

The estimation of ω can be performed by identification of the linear trend ωt_i for $i = 1, \cdots, N$ in ϕ_i obtained by linear regression, such that

$$\hat{\omega} = \frac{\sum_{i=1}^{N} t_i \ \phi_i}{\sum_{i=1}^{N} t_i^2} \ , \tag{2.19}$$

where again $t_i = i\Delta t$. Only stationarity was used here, whereas for the estimation of the diffusion constant D the functional central limit theorem has to be taken into account. Since D is related to the variance of the phase increments $\Delta\phi_i = \phi_i - \phi_{i-1}$,

$$\begin{aligned} D &= \lim_{N\to\infty} \frac{1}{\Delta t N} \ \mathrm{Var}\left(\sum_{i=1}^{N} \Delta\phi_i\right) = \lim_{N\to\infty} \frac{1}{\Delta t} \sum_{k=-N+1}^{N-1} \left(1 - \frac{k}{N}\right) \gamma(k) \\ &= \frac{1}{\Delta t} \sum_{k=-\infty}^{\infty} \gamma(k) \ , \end{aligned} \tag{2.20}$$

where

$$\gamma(k) = E\big[(\Delta\phi_i - E[\Delta\phi_i])(\Delta\phi_{i+k} - E[\Delta\phi_{i+k}])\big]$$

is the auto-covariance function of $\Delta\phi_i$. Due to the stationarity of the process, the auto-correlation function is well defined, it therefore does not depend on i. The auto-covariance function is a substantial part of Eq. (2.20), such that the correlations of the phase increments cannot be neglected in the estimation.

To deal with the problem of correlated phase increments, non-overlapping blocks are used out of the phase increments in a manner to achieve approximately independent blocks. This approach is similar to the one used in block bootstrap [26, 27]. Finding such non-overlapping blocks is possible if the particular time series is strongly mixing which is one of the central requirements of the functional central limit theorem. It is further assumed, without loss of generality, that for a given block-length l the number of blocks b is an integer value. Otherwise the time series of the increments can sufficiently be truncated. We define the total phase increment of each block by

$$\delta_j = \sum_{i=1}^{l} \Delta\phi_{(j-1)l+i} \qquad j = 1, \cdots, b = \frac{N}{l} \ . \tag{2.21}$$

The empirical variance of δ_j divided by $l\Delta t$ therefore yields an appropriate estimate for D and is given by

$$\hat{D} = \frac{1}{l\Delta t}\; b^{-1} \sum_{j=1}^{b} (\delta_j - l\;\hat{\omega}\Delta t)^2 \; . \tag{2.22}$$

Here, the free parameter of the block-length l has to be selected. If, e.g., the block-length was too small, the estimate of D could be strongly biased due to the correlations. On the other hand, if l is too large $\hat{D}$ itself shows a rather high variance. The optimal block-length should balance both effects. This can be achieved if the mean-squared-error MSE = Variance+Bias^2 is minimized with respect to the block-length l, where the bias term corresponds to $E[\hat{D}]-D$.

To apply the selection method for determining the block-length l an approximation of the mean-squared-error is derived. To this end, Eq. (2.22) is rearranged. It turns out that the empirical auto-covariance function $\hat{\gamma}_j$ of block j is the central quantity determining $\hat{D}$. Since $\delta_j = \sum_{i=1}^{l} \Delta\phi_{(j-1)l+i}$, Eq. (2.22) is equivalent to

$$\begin{aligned}
\hat{D} &= \frac{1}{l\Delta t}\; b^{-1} \sum_{j=1}^{b} \sum_{r,m=1}^{l} (\Delta\phi_{(j-1)l+r} - \hat{\omega}\Delta t)\; (\Delta\phi_{(j-1)l+m} - \hat{\omega}\Delta t) \\
&= \frac{1}{l\Delta t}\; b^{-1} \sum_{j=1}^{b} \sum_{k=-l+1}^{l-1} \sum_{m=1}^{l} (\Delta\phi_{(j-1)l+k+m} - \hat{\omega}\Delta t)\; (\Delta\phi_{(j-1)l+m} - \hat{\omega}\Delta t) \\
&= \frac{1}{\Delta t}\; b^{-1} \sum_{j=1}^{b} \sum_{k=-l+1}^{l-1} \hat{\gamma}_j(k) \; ,
\end{aligned} \tag{2.23}$$

where the index r was replaced by $k = r-m$. Thus, the empirical inter-block auto-covariance function of the phase increments is defined by

$$\hat{\gamma}_j(k) = l^{-1} \sum_{m=1}^{l} (\Delta\phi_{(j-1)l+k+m} - \hat{\omega}\Delta t)\; (\Delta\phi_{(j-1)l+m} - \hat{\omega}\Delta t) \; .$$

Due to the the stationarity of the phase increments, the random variable $\hat{\gamma}_j(k)$ does not alter between the blocks j. Moreover, $\hat{\gamma}_j(k)$ is unbiased such that both properties are leading to $E[\hat{\gamma}_j(k)] = \gamma(k)$. Making use of the latter observation and by using the value of D as derived in Eq. (2.20), the bias of $\hat{D}$ can be approximated by

$$\begin{aligned}
E[\hat{D}] - D &= \frac{1}{\Delta t}\; b^{-1} \sum_{j=1}^{b} \sum_{k=-l+1}^{l-1} E[\hat{\gamma}_j(k)] - D = \frac{1}{\Delta t}\; b^{-1} \sum_{j=1}^{b} \sum_{k=-l+1}^{l-1} \left(1 - \frac{|k|}{l}\right) \gamma(k) - D \\
&\approx \frac{1}{\Delta t} \sum_{k=-\infty}^{\infty} \left(1 - \frac{|k|}{l}\right) \gamma(k) - D = -\frac{1}{l\;\Delta t} \sum_{k=-\infty}^{\infty} |k|\gamma(k) \; ,
\end{aligned} \tag{2.24}$$

where contributions of the auto-covariance function for values $|k| \geq l$ are neglected. This is possible if the block-length l is close to the optimal. The variance of $\hat{D}$ can be treated in a

similar fashion, it reads

$$\mathrm{Var}(\hat{D}) = \left(\frac{1}{\Delta t}\right)^2 b^{-2}\ \mathrm{Var}\left(\sum_{j=1}^{b}\sum_{k=-l+1}^{l-1}\hat{\gamma}_j(k)\right) \approx \left(\frac{1}{\Delta t}\right)^2 b^{-1}\ \mathrm{Var}\left(\sum_{k=-\infty}^{\infty}\hat{\gamma}(k)\right) . \quad (2.25)$$

Here, the index j which represents the block for which the empirical auto-covariance function is calculated is dropped. This is again due to the approximation that contributions beyond the block-size are negligible small if l is close to the optimum. In Eq. (2.25), the last term deserves further investigation. From spectral analysis it is known that the variance of the sum over the empirical auto-covariance is asymptotically given by

$$\mathrm{Var}\left(\sum_{k=-\infty}^{\infty}\hat{\gamma}(k)\right) = 2\left(\sum_{k=-\infty}^{\infty}\gamma(k)\right)^2 , \quad (2.26)$$

as shown e.g. in [28, 29]. Substituting $b = N/l$ and by combining Eqs. (2.24), (2.25), (2.26) finally yields the desired approximation of the mean-square-error

$$\mathrm{MSE} \approx (\Delta t)^{-2}\left(l^{-2}C_1 + \frac{2l}{N}\ C_2\right) , \quad (2.27)$$

where

$$C_1 = \left(\sum_{k=-\infty}^{\infty}|k|\ \gamma(k)\right)^2 , \quad \text{and} \quad C_2 = \left(\sum_{k=-\infty}^{\infty}\gamma(k)\right)^2 .$$

The optimal block-length is given by the minimum of Eq. (2.27), thus $l_{opt} = (N\ C_1/C_2)^{\frac{1}{3}}$. Certainly, both constants C_1 and C_2 are unknown in the first place, moreover if C_2 was known the diffusion constant could be calculated using Eq. (2.20) directly. Instead, rough estimates of these constants are used to determine an almost optimal block-length, whereas the outcome of Eq. (2.20) is directly linked to the estimate of C_2 and has to be quite accurate instead. Under the assumption that the auto-covariance function decays exponentially, such a rough estimate is given by the following scheme [27]:

1. Estimate the auto-correlation function of the increments $\Delta\phi_i$ for $k \ll N$ by

$$\hat{\gamma}(k) = (N-k)^{-1}\sum_{i=1}^{N-k}(\Delta\phi_i - \Delta t\hat{\omega})\ (\Delta\phi_{i+k} - \Delta t\hat{\omega}) .$$

2. Fit $\varphi(k) = \varphi^k$ to the envelope of the auto-correlation function.

3. Compute the estimate of the optimal block-length $\hat{l}$ by

$$\hat{l} = (4\ N)^{1/3}\left(\frac{\varphi}{1-\varphi} + \frac{\varphi^2}{(1-\varphi)^2}\right)^{2/3}\ \left(1 + 2\ \frac{\varphi}{1-\varphi}\right)^{-2/3} .$$

The statistical properties of the mean phase coherence have been derived, where the mean angular velocity and the diffusion coefficient can reliably be estimated. An application to empirical data is therefore feasible. This is demonstrated in the following simulation study.

2.7. Simulation Study

To assess the performance of the proposed test, a system of two coupled stochastic Rössler oscillators [20]

$$\begin{aligned} \dot{x}_{1,2} &= -\omega_{1,2}\, y_{1,2} - z_{1,2} + \epsilon\, (x_{2,1} - x_{1,2}) + \sigma\, \eta_{1,2} \\ \dot{y}_{1,2} &= \omega_{1,2}\, x_{1,2} + a\, y_{1,2} \\ \dot{z}_{1,2} &= b + (x_{1,2} - c)\, z_{1,2} \end{aligned} \tag{2.28}$$

is investigated, where the two-in-one notation similar to the one in Sec. 2.3 is used. Again, the dynamic noise is modeled by Gaussian distributed random variables $\eta_{1,2} \sim \mathcal{N}(0,1)$ thus leading to the variance σ^2 of the noise term $\sigma\,\eta_{1,2}$. In addition, the same parameter values $a = 0.15$, $b = 0.2$, $c = 10$, and $\omega_{1,2} = 1 \pm 0.015$ as in Sec. 2.3 are used. Furthermore, the same sampling rate of 0.1 is chosen. For the synchronization analysis only the x-components of the Rössler oscillators are again examined.

The coupling strength between the two oscillators is modeled by the parameter ϵ. We varied this value, the noise $\sigma\,\eta_{1,2}$, and length of the sample N for each Rössler oscillator to quantify the coverage as well as the power of the proposed significance level. The coverage measures the number of false positive conclusions in the absence of phase synchronization and has to be controlled, i.e., there should be not more than α-false positive conclusions for an α-significance level as described in Sec. 2.3. The critical value for the α-significance level can be derived from Eq. (2.15) by

$$R^{\alpha}_{N,crit} = \mathrm{tr}\ \mathrm{C} \cdot \chi^2_{1,\,\alpha}\ , \tag{2.29}$$

here $\chi^2_{1,\alpha}$ denotes the α-quantile of the χ^2-distribution with one degree of freedom. Recall that the power is the probability to rejected the null-hypothesis H_0 correctly for a given violation of H_0. In the following, 100 realizations for every parameter combination is simulated to determine power and coverage of the proposed significance level.

The results are shown in Fig. 2.2. Here, the amount of data N is either chosen to be $N = 8192$ for the top row, or $N = 16384$ for the bottom row. Subsequent columns are reflecting different noise levels σ. These are ranging between $\sigma = 0.2$ and $\sigma = 0.8$. The coupling strength ϵ is varied for each parameter combination in the range from $\epsilon = 0$ to $\epsilon = 0.06$. Note that the horizontal line in each graph corresponds to a level of significance of 5%. First, we would like to emphasize that for absence of coupling between the Rössler oscillators the coverage is equals or below the 5%-significance level. From this behavior we can conclude that the critical value for the mean phase coherence prevents erroneous conclusions in the case of absent coupling and, moreover, approves the expected conservative behavior which is discussed in Sec. 2.5. Second, for high coupling strengths, a sufficiently large noise strength, and enough data the power reaches values of 100%, Figs. 2.2c-h. The steepness of several power curves especially for a sample size of $N = 16384$, emphasizes the good performance of the proposed test.

A more detailed examination of the power curves yields some interesting properties. To simplify our statements, let us focus on non-zero coupling strengths for the following discus-

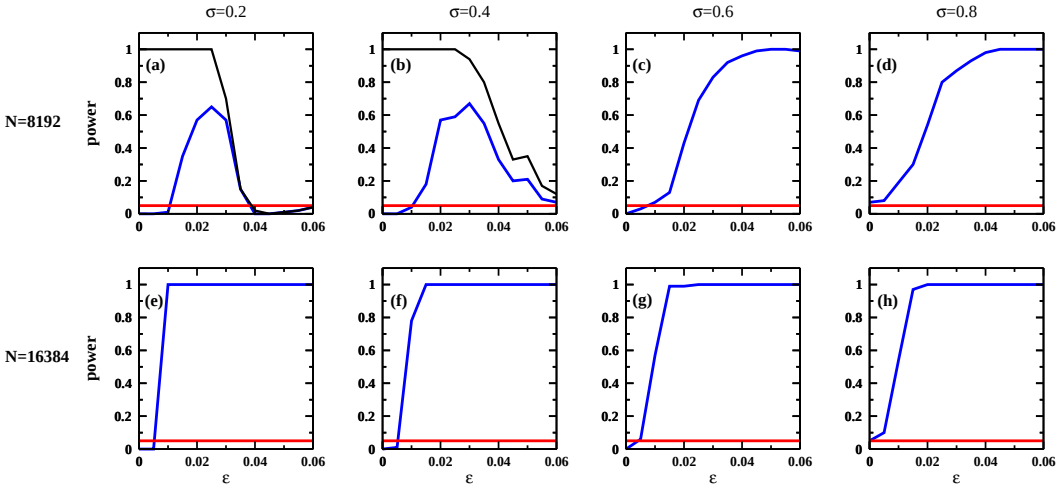

Figure 2.2: Power of the proposed significance level in dependence on data length and noise level. The first row shows the results for the sample size of $N = 8192$ and second row displays the results for $N = 16384$. Different noise levels σ are used for each subsequent column. The red line indicates the 5% significance level. Blue lines are showing the power of the proposed test versus the coupling strength ϵ. The black line in (a), and (b)indicate the fraction of critical values below one.

sion. In general, the performance of the test increases while the amount of data increases. This behavior is intuitively expected since a decision which is based on a large amount of data is more reliable than if only a few data points are taken into account. Therefore, the sensitivity of the test increases with the data size. The influence of the noise intensity is that it alters the rate of mixing of the Rössler systems. An increase of the noise strength leads to a higher phase diffusion, such that more approximately independent data points are available for the test. The amount of data is effectively higher in a manner that less data are used for achieving the same accuracy. If small sample sizes are considered, effects due to the rate of mixing are even more illustrative. A higher noise intensity can increases the performance test, as shown below. Note that the power in Fig. 2.2a starts decaying for a coupling strengths larger than 0.025. This is caused by the occurrence of critical values $R^{\alpha}_{N,crit}$ in Eq. (2.29) above one, thereby preventing the detection of significant results. This effect emerges in the simulations shown in Fig 2.2a, and b. The black line shows the fraction of critical values that are below one. For the cases where the power decreases, the critical value is to a certain extent close to or higher than one. Equation (2.29) enables us to understand of this phenomenon. The χ^2-distribution multiplied by the trace of matrix C is not bounded by one as the mean phase coherence itself. Especially for low noise strengths and small sample sizes this phenomenon may arise. Increasing the noise yields that the critical value is smaller than one, such that the derived statistics to becomes applicable, Fig. 2.2c, and d. Once a particular noise value is exceeded, here $\sigma = 0.6$, the power does not decrease any more for the considered range of ϵ. Alternatively the asymptotic behavior can also be achieved, when the number of data points is enlarged. This is revealed by the graphs in the second row. Here, even for small coupling strengths, no critical value below one is observed and the power curve increases monotonous with ϵ, Figs. 2.2e-h.

Additionally, for higher coupling strengths than used in this simulation study, it might happen that the derived approximation is not in its asymptotics. Then, a critical value higher than one would be observed preventing any conclusions about a coupling between the oscillators. Whenever a critical value of one or a critical value higher than one is obtained, further investigations are necessary as to which extent this belongs to a true result, a finite size effect or a violation of the assumptions. In this sense the significance level prevents false positive conclusions as it indicates when its assumptions are not fulfilled. Moreover, the length of the necessary segments to estimate the diffusion coefficient is an indicator whether or not the process is sufficiently mixing. If the length of the segments is too large, one should be cautious when drawing conclusions. Furthermore, the proposed significance level is not capable of distinguishing coupling between oscillators and for instance a signal propagation. One has to ensure in the first place, that whether one is in the regime of coupled synchronizing oscillators or not. This problem is common in time series research and there are suggestions how to distinguish synchronizing oscillators from, e.g., signal propagation [30].

2.8. Conclusion

The distribution of the test statistics is derived for the mean phase coherence that leads to a critical value for a corresponding significance level that allows to test for a non-zero synchronization value. The main mathematical assumption which is needed to derive this distribution is the strong mixing condition, Eq. 2.6. However, in the following Chapter it is discussed that this assumption is almost the minimal requirement in order to avoid spurious results. The only possible relaxation of the mixing assumption is that weak mixing might be considered to be able to estimate the mean phase coherence $\hat{R}_N$ reliably. Here, weak mixing refers to the decay of the auto-correlation function rather than the entire statistical dependency structure. The performance of the proposed test has been demonstrated in a simulation study based on coupled stochastic Rössler oscillators. The coverage of the significance level is conservative. Moreover, the level of significance is characterized by a steep increase in power. One major advantage of the proposed significance level lies in the fact that the suggested procedure provides information about its applicability to the problem at hand. If the segment length necessary for the estimation of the diffusion term is too large compared to the time series length, indicating that the system is either non-mixing or that the mixing is too slow, the proposed significance level should not be used which is indicated by the proposed procedure. In contrast to the naïve approaches, this prevents false positive conclusions about the synchronization in cases, where these conclusions cannot be inferred. In summary, the proposed significance level works well for a large variety of coupling strengths, noise variances, and sample sizes. It provides, thus, a powerful test for the presence of phase synchrony.

3

Mixing Properties of the Rössler System and its Consequences

3.1. Introduction

In the previous Chapter, the distribution of the mean phase coherence was derived under the hypothesis of absent phase synchronization. The central assumption on the generating processes is the mixing property $\lim_{k\to\infty} \alpha(k) = 0$, where $\alpha(k)$ is defined in Eq. (2.6), p. 12. However, this assumption is not only required to derive the statistical properties of the estimator for the mean phase coherence $\hat{R}_N$, but is also necessary to avoid spurious results. This is due to the fact, that a phase coherent behavior of two independent systems can be observed, since the phase of one oscillator is not drifting away with respect to the other. Such a misleading behavior can, e.g., happen for systems exhibiting a limit circle. We can therefore conclude that beside ergodicity, mixing is the most important stochastic feature of chaotic systems which is essential for synchronization analysis on the basis of empirical data. A second method to detect couplings of two systems is the coherency analysis. Again, the mixing of the observed systems is essential, as shown below. Here, it should be noted that some kind of mixing is also essential for statistical mechanics and thermodynamics. This is due to the demand that interactions between subsystems should not be too strong and negligible on a macroscopic scale such that the entropy is an extensive quantity [31]. A further property of mixing is that it implies the decay of the auto-covariance function, which is of great importance in the following.

For deterministic dynamical systems the rather abstract definition of the mixing property given in Chapter 2 can be reformulated. To do so, let $M_t(x)$ be the time evolution of a certain point x in phase space by an ergodic dynamic system, thus $x = M_{t=0}(x)$. The invariant measure is denoted by μ and exists by the demand that the system has to be ergodic. Mixing

of such a dynamical system is then satisfied if for all μ-measurable sets A, B the condition

$$\lim_{t\to\infty} \mu\left(A \cap M_t^{-1}(B)\right) = \mu(A)\ \mu(B) \tag{3.1}$$

is valid [32]. The set $M_t^{-1}(B)$ in Eq. (3.1) refers to the compact notation for the inverse image of M_t, $M_t^{-1}(B) = \{x : M_t(x) \in B\}$. Using the definition above, the system of our interest, namely the Rössler system [20]:

$$\begin{aligned} dx/dt &= -y - z \\ dy/dt &= x + ay \\ dz/dt &= b + (x - c)z\ , \end{aligned}$$

shows for a specific set of the parameters $a = b = 0.2$, $c = 6.3$ a behavior which could be explained by a defect of mixing. An alternative explanation would be the presence of finite size effects. This behavior vanishes if dynamical noise of a sufficient strength is included as it is done in Chapter 2. In this Chapter, however, the noise-free case is studied to discriminate a loss of mixing from finite size effects.

A possible loss of mixing is connected to the non-hyperbolicity of the system, since for hyperbolic or Axiom A systems mixing is always satisfied. Furthermore, the mixing coefficient, describing the statistical dependency of time lagged events or the correlations of sufficiently smooth observables is decaying exponentially and the rate of this decay is related to the positive Lyapunov exponents for these systems. The key point of these statements is the qualitative knowledge of the spectrum of the time evolution operator for the probability density of the system's states P_t, the so called Frobenius-Perron operator (FPO), [32]. Note that this density is chosen to be absolutely continuous with respect to some invariant measure. It can be shown that the resolvent function of the FPO: $R(z) = (\mathbb{1}z - P_t)^{-1}$ can be meromorphically extended onto the whole complex space [33-35]. The poles of the resolvent function are lying in the interior of the unit circle except for the simple pole at one, corresponding to the invariant measure. Since poles of the resolvent function are the point spectrum of the FPO and by using $P_{n\Delta t} = P_{\Delta t}^n$, the exponential decay of correlations for a sufficiently smooth real-valued observables can be shown. Moreover, eigenvalues close to the unit circle are generating sharp peaks of approximately Lorentzian shape in the power spectrum. This consequence is in perfect accordance with the more heuristic derivation of peak shapes of chaotic oscillators given in [36]. The corresponding eigenvalues are called Ruelle-Pollicott resonances.

In case of non-hyperbolic systems the discussed properties of the resolvent function need not be fulfilled. Generally, the Lyapunov exponents are not related to the rate of mixing, even if the process of interest satisfies condition (3.1). Instead, the spectrum of the FPO may have a cluster point on the unit circle which leads to a loss of mixing. Non-rigorous methods such as calculating the spectrum of the FPO in a finite dimensional approximation and performing the limit of infinite dimension have been applied, e.g., in [37, 38]. The comparison of the analytically derived results are in good accordance with simulations, even though there is no rigorous justification of this method. However, such a procedure is not feasible for the Rössler system, since the FPO P_t can only be approximated numerically and thus the limit

of infinite dimension is not possible. If the last step is omitted, the calculated eigenvalues and eigenfunctions would depend on the chosen set of basis functions. Inconsistency would therefore be the consequence of such a procedure. It is therefore not likely to approach the question of mixing of the Rössler system on the basis of the FPO.

In the following, it turns out that the crucial point relating to the mixing property of the Rössler system is the phase dynamics in the x-y plane. Before analyzing the phase dynamics in detail, consequences resulting from the absence of mixing are reviewed and empirical results are given for the power spectrum, and cross-spectral analysis in Sec. 3.2, as well as synchronization analysis in Sec. 3.3. A detailed analysis of the phase dynamics is then given in Sec. 3.4.

3.2. Spectral, Cross-Spectral Analysis and Mixing

In this section, the relation of the mixing property to the estimation of the power spectrum and the cross spectrum is examined. From the knowledge of the FPO the power spectrum of the process can be obtained. Moreover, the eigenvalue spectrum of the FPO determines the power spectrum of dynamical systems. To demonstrate this statement, let $f, g \in L^2$ be real valued observables satisfying

$$\lim_{n\to\infty} P^n_{\Delta t} f = \lim_{n\to\infty} P^n_{\Delta t} g = 0 \,, \tag{3.2}$$

which is equivalent to that both f and g are having an average of zero on the attractor. The dynamical system is assumed to be ergodic, therefore the unique invariant measure μ exists and its density corresponds to the non-degenerate eigenvalue 1 of the FPO. Due to Eq. (3.2), the observables f, g are orthogonal to the eigenspace, in which the invariant density lies. The correlation function is then

$$C^{f,g}(n) = \int g(x) P^n_{\Delta t} f(x)\ \mu(dx) \,.$$

For some complex values $z \in \mathbb{C}$ satisfying $|z| > 1$, the discrete Laplace transformation of the latter correlation function, given by

$$\tilde{C}^{f,g}(z) = \sum_{n=0}^{\infty} C^{f,g}(n)\ z^{-n} = \sum_{n=0}^{\infty} \int g(x)\ z^{-n}\ P^n_{\Delta t} f(x)\ \mu(dx) \,, \tag{3.3}$$

can be rewritten in terms of the resolvent function $R(z)$ of the FPO and yields

$$\tilde{C}^{f,g}(z) = \int g(x)\ zR(z)\ f(x)\ \mu(dx) \,. \tag{3.4}$$

The step from Eq. (3.3) to Eq. (3.4) needs some mathematical justification. First, observe that the sum and the integral in Eq. (3.3) can be exchanged. This is due to the property of the FBO referred to as Markov operator. A Markov operator P satisfies: $Pf \geq 0$ for every positive function $f \in L^2$ and $||P|| \leq 1$, where $||\cdot||$ refers to the usual operator

norm $||P|| = \sup_{\{f\in L^2,||f||=1\}} ||Pf||$. It follows that, $||P^n_{\Delta t}f|| \leq ||P||^n||f|| \leq ||f|| < \infty$ and hence there exists a function $\tilde{f} \in L^2$ which dominates $P^n_{\Delta t}f$. The partial sum of Eq. (3.3), $\sum_{n=0}^{N} \int g(x)P^n_{\Delta t}f(x)\ z^{-n}\ \mu(dx)$, allows the exchange of integration and summation since it is a finite sum. Moreover, $\sum_{n=0}^{N} g(x)P^n_{\Delta t}f(x)\ |z|^{-n}$ can be dominated by $g(x)\tilde{f}(x)\ (1-|z|^{-1})^{-1} \in L^2$ because $|z| > 1$. Now, the Lebesgue dominated convergence theorem guarantees the interchangeability of summation and integration in Eq. (3.3). Recall that resolvent function is given by $R(z) = (\mathbb{1}z - P_{\Delta t})^{-1}$. And we can therefore represent $zR(z)$ in Eq. (3.4) by the Neumann-series: $zR(z) = (\mathbb{1} - P_{\Delta t}/z)^{-1} = \sum_n^{\infty} z^{-n}\ P^n_{\Delta t}$, which is possible since $\limsup_{n\to\infty} ||(P_{\Delta t}/z)^n||^{\frac{1}{n}} \leq |z|^{-1} < 1$. Exactly the expression $zR(z) = \sum_n^{\infty} z^{-n}\ P^n_{\Delta t}$ occurs in Eq. (3.3) if summation and integration have been exchanged, thus leading to Eq. (3.4). Suppose now that f can be decomposed into eigenfunctions f_i of the FPO: $f(x) = \sum_{i=1}^{\infty} a_i f_i(x)$. The eigenvalues of f_i are denoted by z_i and are satisfying $|z_i| \leq 1$ again since $P_{\Delta t}$ is a Markov operator. Eq. (3.4) then yields

$$\tilde{C}^{f,g}(z) = \sum_{i=1}^{\infty} \frac{a_i z}{z - z_i} \int g f_i\ d\mu\ . \tag{3.5}$$

If all eigenvalues z_i are compactly contained in the unit circle, Eq. (3.5) can be homomorphically extended onto the unit circle by similar manipulations used above. Thus, $\tilde{C}^{f,g}(z)$ is defined for $z = e^{i\omega\Delta t}$ and yields $S(\omega) = \tilde{C}^{f,g}\left(e^{i\omega\Delta t}\right)$, which is the one-sided Fourier transform of the correlation function or the power spectrum. The power spectrum is usually defined by the two-sided Fourier transformation but in case of non-invertible dynamics such a power spectrum would not be defined. Therefore, the general structure of such a power spectrum is given by the smooth function

$$S(\omega) = \sum_{j=1}^{\infty} \frac{\gamma_j\ e^{i\omega\Delta t}}{e^{i\omega\Delta t} - z_j}\ ,$$

where eigenvalues close to the unit circle are able to produce resonances of Lorentzian shape. Such a specific distribution of the eigenvalues corresponds to a dynamical system equipped with the mixing property.

In case of the absence of mixing, in which the eigenvalues z_i are having a cluster point on the unit circle, the transition from $|z| > 1$ to $|z| = 1$ in Eq. (3.5) is not possible. But due to the assumed ergodicity the correlation function exists and thus the Wiener-Khintchine theorem guarantees the existence of a spectral distribution function [29]. Such a distribution function is in general not represented by a smooth density, instead delta-distributions are often present.

For empirical time series of length N, the power spectrum can be estimated by calculating the discrete Fourier transform of the observed time series x_i, $i = 1, \cdots, N$. The squared norm of the Fourier transform then defines the periodogram

$$\mathrm{Per}(\omega) = |f(\omega)|^2 \qquad \text{and} \qquad f(\omega) = \frac{1}{\sqrt{N}} \sum_{k=1}^{N} x_k\ e^{-i\omega k}\ . \tag{3.6}$$

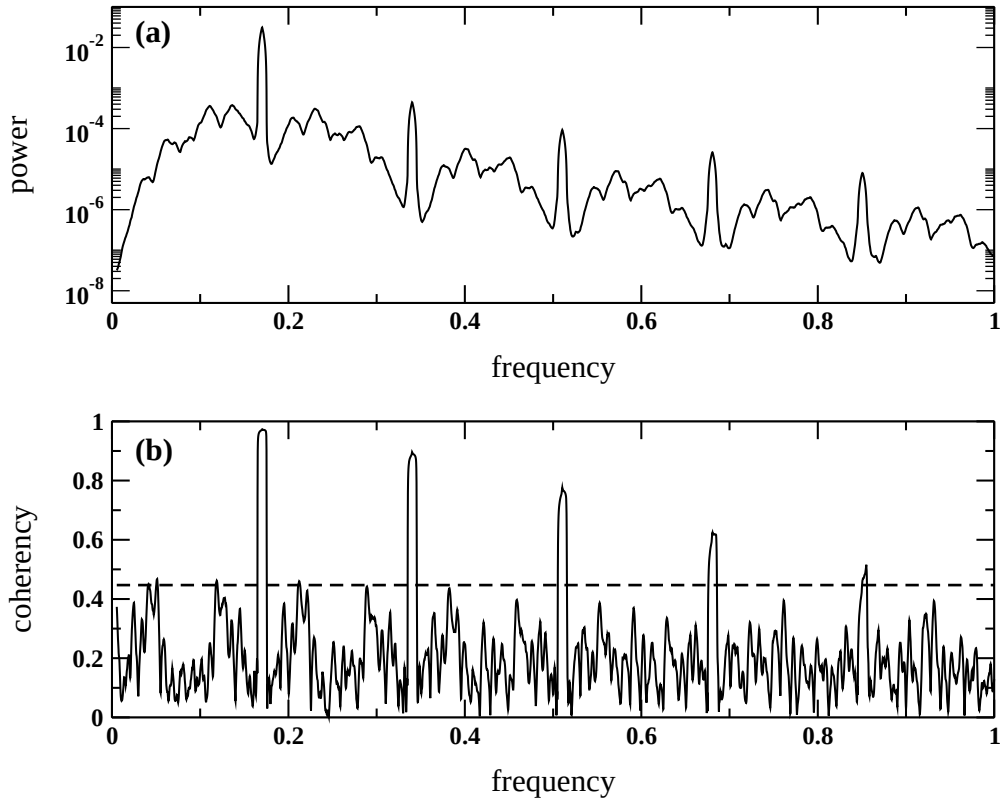

Figure 3.1: (a) Power spectrum of the x-component of the Rössler system at the vicinity of the its main oscillating frequency. (b) Coherency of two independent, identical Rössler systems. The coherency at frequencies of approximately 0.17 and its multiplies are lying above the 5% level of significance (dashed line).

If the power spectrum is a smooth function in the frequency domain and the time series mixes sufficiently, the periodogram $\mathrm{Per}(\omega)$ is χ^2-distributed

$$\mathrm{Per}(\omega) \sim S(\omega)\chi^2_2/2 \qquad \omega \neq 0 \text{ and } \pi \ ,$$

which is due to the central limit theorem [39, 28, 14]. Increasing N increases the frequency resolution but does not reduce the variance of the periodogram. In order to obtain a consistent estimation of the power spectrum, in which the variance vanishes if $N \to \infty$, the periodogram has to be smoothed [28, 29]. If, e.g., the spectral density contains a delta-distribution the smoothing procedure is no longer consistent. Due to the orthogonality of the Fourier transform, the growth of height with respect to the amount of data for this component is proportional to N. The x-component of the discussed Rössler system is showing sharp peaks in the power spectrum, Fig. 3.1a. By increasing the amount of data N, the peak seems to grow in height but the growth rate cannot be determined because of finite size effects. This is mainly due to the uncertainty of the peak location and truncation effects, also known as tapering effects.

The absence of mixing not only leads to severe problems for estimating the univariate power spectrum, but also the estimation of the bivariate cross-spectrum is problematic if

the mixing condition is not fulfilled for the underlying processes. Cross-spectral analysis is an analysis technique for detecting a linear relationship between two processes $x(t)$ and $y(t)$. The processes x, y are assumed to have zero mean and unit variance, if not a linear transformation has to be applied such that the processes are satisfying these requirements. The cross-spectrum is then defined by the Fourier transformation of the cross-correlation function:

$$\begin{aligned} \mathrm{CCF}(\tau) &= E[x(t)y(t-\tau)] \\ \mathrm{CCF}(\omega) &= \frac{1}{2\pi}\int \mathrm{CCF}(\tau)\ \exp(-i\omega\tau)\ d\tau\ , \end{aligned}$$

normalized by the product of square root of the univariate power spectra $S_x(\omega), S_y(\omega)$:

$$\mathrm{CS_{xy}}(\omega) = \frac{\mathrm{CCF}(\omega)}{\sqrt{S_x(\omega)\ S_y(\omega)}}\ .$$

According to the previous Chapter $E[\cdot]$ denotes the expectation value. This function is in general complex and can therefore be decomposed into the phase spectrum $\Phi_{xy}(\omega)$ and the coherency $\mathrm{Coh}_{xy}(\omega)$, such that

$$\mathrm{CS_{xy}}(\omega) = \mathrm{Coh}_{xy}(\omega)e^{i\Phi_{xy}(\omega)}\ .$$

Due to the normalization of the cross-spectrum the coherency is ranging from $\mathrm{Coh}_{xy}(\omega) = 0$, no linear relationship between x and y at ω, to $\mathrm{Coh}_{xy}(\omega) = 1$, perfect linear relationship. Whereas the interpretation of the phase spectrum $\Phi_{xy}(\omega)$ is more difficult, see e.g. [40]. The estimation of the cross-spectrum is analogous to the estimation of the power spectrum. Furthermore, an asymptotic level of significance under the hypothesis $\mathrm{Coh}_{xy}(\omega) = 0$ can be derived

$$s = \sqrt{1 - \alpha^{\frac{2}{\nu-2}}}\ , \tag{3.7}$$

where ν is the number of equivalent degrees of freedom depending on the smoothing procedure of the spectra [39, 29, 28, 40-42].

Mixing of the processes is again essential for cross-spectral analysis and for deriving Eq. (3.7). In case of two independent processes x and y we obviously have $\mathrm{Coh}_{xy} = 0$. According to [28, 39], the estimation of this quantity is possible if the processes can be approximated by the linear sequences

$$x(t) = \sum_{i=0}^{\infty} C_1(i)\ z_1(t-i) \quad \text{and} \quad y(t) = \sum_{i=0}^{\infty} C_2(i)\ z_2(t-i)\ ,$$

where $z_i(t)$ is an independent and identically distributed sequence of random variables having zero mean and a finite fourth moment. Moreover, the coefficients must satisfy

$$\sum_{j=0}^{\infty} |C_i(j)|\ j^{1/2} < \infty\ , \quad i = 1, 2\ . \tag{3.8}$$

Necessarily, $C_i(j) \to 0$ if $j \to \infty$ and hence the autocorrelation of x and y must decay, which is valid if both processes are mixing. Besides the pure estimation of the cross-spectrum, statistical inference such as Eq. (3.7) is based on the asymptotical normality of sums of state variables. Here, mixing is again a central requirement, see e.g. [25].

Now, 5×10^5 data points of the chaotic attractor of two independent, identical Rössler systems are simulated. For this simulation and the following simulations, the Rössler system is integrated by a Runge-Kutta scheme of fourth order with step size control keeping the numerical error below $\varepsilon = 10^{-12}$ [14]. The sampling rate of both time series was chosen to be $\Delta t = 0.01$. If the conditions of the cross-spectral analysis are valid, coherency of the x-component should be zero, since there is no (linear) relationship between the time series. But Fig. 3.1b clearly shows a significant coherency. This result can be interpreted in two different ways: 1. mixing is violated as outlined above or 2. the decay of the phase correlations is too slow such that the cross-spectral analysis has not reached its asymptotic accuracy.

3.3. Synchronization Analysis and Mixing

Like in Chapter 2, the mean phase coherence is used to quantify phase synchronization. Again, phase synchronization of two coupled, chaotic oscillators occurs if the $n : m$ phase locking condition is satisfied $|n\varphi_x(t) - m\varphi_y(t)| = |\Phi_{n,m}| < const$, where $\varphi_x(t), \varphi_y(t)$ denotes the phase of the time series $x(t), y(t)$ and n, m are given integers. To suppress phase jumps, induced by the presence of numerical or observational noise, $\Phi_{n,m}$ is, according to Chapter 2, modified by $\Psi_{n,m} = \Phi_{n,m} \bmod 2\pi$. Using the latter quantities, the mean phase coherence is given by

$$R^2_{n,m} = E[\cos(\Psi_{n,m})]^2 + E[\sin(\Psi_{n,m})]^2 \,,$$

cf. Sec 2.3. Recall that the mean phase coherence is $R_{n,m} = 1$ for a constant phase difference between the two time series and $R_{n,m} = 0$ for a uniformly distributed phase difference. Note that the usage of the Hilbert transform, introduced in Sec 2.3, is used in order to determine the phase difference $\Phi_{n,m}$. In our case the phase difference can be calculated directly from a x-y projection of the corresponding Rössler systems, but the outcome of the synchronization analysis does not alter if either the Hilbert transform or the direct computation is considered.

The mixing property for the phases is again essential to determine whether the processes are phase synchronizing on the basis of measured data or not. For demonstrating this statement, let us consider two ergodic self-sustained oscillatory systems satisfying $E[\cos(\Psi_{n,m})] = E[\sin(\Psi_{n,m})] = 0$, and thus $R^2_{m,n} = 0$. Suppose that $\Psi_i,\ i = 1, \cdots, n$ is a suitable realization of $\Psi_{n,m}$ which is equidistantly sampled in t. By the ergodic theorem $R^2_{n,m}$

is given by

$$\begin{aligned} R_{n,m}^2 &= \lim_{N\to\infty}\left\{\left(N^{-1}\sum_{i=1}^{N}\sin(\Psi_i)\right)^2+\left(N^{-1}\sum_{i=1}^{N}\cos(\Psi_i)\right)^2\right\} \\ &= \lim_{N\to\infty} N^{-2}\sum_{i,j=1}^{N}\left(\sin(\Psi_i)\sin(\Psi_j)+\cos(\Psi_i)\cos(\Psi_j)\right) \\ &= N^{-1}+2N^{-2}\sum_{j=1}^{N-1}\sum_{i=1}^{N-j}\left(\sin(\Psi_i)\sin(\Psi_{i+j})+\cos(\Psi_i)\cos(\Psi_{i+j})\right) . \end{aligned} \tag{3.9}$$

Since the sample is equidistant in time and by using the ergodicity again we have

$$\begin{aligned} &\frac{1}{N-j}\sum_{i=1}^{N-j}\left(\sin(\Psi_i)\sin(\Psi_{i+j})+\cos(\Psi_i)\cos(\Psi_{i+j})\right) \\ &= \underbrace{E[\sin(\Psi_1)\sin(\Psi_{1+j})+\cos(\Psi_1)\cos(\Psi_{1+j})]}_{=\xi_j}+r_{Nj}=\xi_j+r_{Nj} , \end{aligned} \tag{3.10}$$

for each $0 < j < n$. The remainder r_{Nj} vanishes asymptotically, $\lim_{N\to\infty} r_{Nj} = 0$. Inserting Eq. (3.10) into Eq. (3.9) we arrive at

$$\begin{aligned} R_{n,m}^2 &= \lim_{N\to\infty}\left\{N^{-1}+2\sum_{j=1}^{N-1}\frac{N-j}{N^2}(\xi_j+r_{Nj})\right\} \\ &= \lim_{N\to\infty} 2\sum_{j=1}^{N-1}\frac{N-j}{N^2}\xi_j . \end{aligned} \tag{3.11}$$

A necessary condition that $R_{n,m}^2$ in Eq. (3.11) vanishes is therefore $\xi_j \to 0$ if $j \to \infty$. Now, consider $\sin(\Psi_{n,m})$ and $\cos(\Psi_{n,m})$ as new observables of the processes, then ξ_j is the sum of the auto-covariance function of these quantities. Again, the auto-covariance function asymptotically vanishes if mixing, Eq. (3.1), is satisfied. The necessary condition is therefore met if both processes exhibits mixing. It should further be noted that the equidistant sampling is not explicitly needed and was only introduced to avoid a rather clumsy notation.

Again, two independent, identical Rössler systems are generated numerically, where the sampling is chosen to be $\Delta t = 0.01$ for both realizations of length 131072. The time evolution of $\Phi_{1,1}$ and the distribution of $\Psi_{1,1}$ is shown in Fig. 3.2 and reveals that the phase-locking condition seems to be satisfied. Furthermore, the narrow peak of the distribution of $\Psi_{1,1}$ indicates that the mean phase coherence should be close to unity. Calculating the mean phase coherence yields $R_{1,1} = 0.92$. On the basis of empirical data, one would draw the conclusion that these two time series are phase synchronized which is again spurious, either due to a loss in mixing or due to finite size effects. In addition, these results show that this question can be approached only by analyzing the phase evolution of the Rössler system.

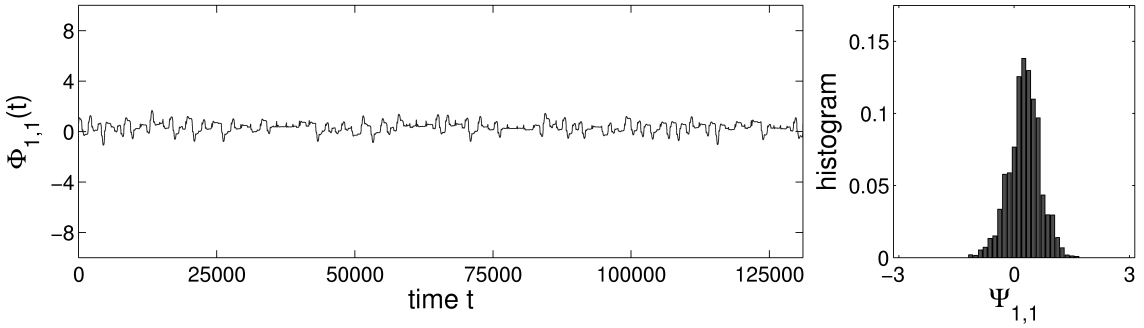

Figure 3.2: Time evolution of $\Phi_{1,1}$ for two independent Rössler systems, left graph. Clustering of phase difference $\Phi_{1,1}$ for values close to zero indicates that the phase locking condition $|\varphi_x(t) - \varphi_y(t)| = |\Phi_{n,m}| < const$ is satisfied. In addition, the histogram of $\Psi_{1,1}$, right figure, is showing an exposed, sharp peak such that phase synchronization is emphasized even though both systems do not interact.

3.4. A Model for the Phase Fluctuations

In the following, a model of the phase fluctuations is derived. The analysis shows that the diffusion constant of the Rössler system depends mainly on the inverse square of the amplitude in the x-y plane. The possibility of such a phase-amplitude dependency of chaotic oscillators is briefly discussed in [43]. Assuming that the system behaves like a diffusion process and that the z-component is approximately constant for a time step $\Delta t \ll 1$, an approximation of the phase fluctuations can be determined. The differential equation then reduces to the form: $dx/dt = -y - z_t$, $dy/dt = x + ay$ and can be integrated one step ahead

$$\begin{aligned} x_{t+\Delta t} &= A_t\, e^{\frac{a\Delta t}{2}} \cos(\omega\Delta t + \phi_t) - z_t\Delta t \\ y_{t+\Delta t} &= A_t\, e^{\frac{a\Delta t}{2}} \left(\omega \sin(\omega\ \Delta t + \phi_t) - \sqrt{1-\omega^2}\ \cos(\omega\Delta t + \phi_t)\right), \end{aligned} \tag{3.12}$$

where $\omega^2 = 1 - (\frac{a}{2})^2$ and A_t is the amplitude and ϕ_t is the phase at time t. In order to include the diffusion, Eq. (3.12) is perturbated by Gaussian white noise. Setting $\tau = \omega\Delta t + \phi_t$, the extended Eq. (3.12) yields

$$\begin{aligned} x_{t+\Delta t} &= A_t\, e^{\frac{a\Delta t}{2}} \cos(\tau) - z_t\Delta t + \sqrt{D_x\Delta t}\ \epsilon_t \\ y_{t+\Delta t} &= A_t\, e^{\frac{a\Delta t}{2}} \left(\omega \sin(\tau) - \sqrt{1-\omega^2}\ \cos(\tau)\right) + \sqrt{D_y\Delta t}\ \eta_t\ , \end{aligned}$$

where ϵ_t, η_t denotes uncorrelated white noise and D_x, D_y are the assumed diffusion constants for the x and y-component respectively. Now, the phase $\phi_{t+\Delta t} = \arctan(y_{t+\Delta t}/x_{t+\Delta t})$ is calculated up to order $\sqrt{\Delta t}$ in all noise terms and yields

$$\phi_{t+\Delta t} = \arctan(\kappa_t) + \frac{e^{-\frac{a\Delta t}{2}}}{A_t \cos(\tau)\left(1+\kappa_t^2\right)} \left(\kappa_t z_t\ \Delta t + \sqrt{D_y\Delta t}\ \eta_t - \kappa_t\ \sqrt{D_x\Delta t}\ \epsilon_t\right) + O(\Delta t)\ ,$$

where $\kappa_t = \omega\tan(\phi_t) - \sqrt{1-\omega^2}$. The diffusion constant of the phase is therefore determined by $D_{A_t,\phi_t} = \lim_{\Delta t\to 0} \mathrm{Var}(\phi_{t+\Delta t})/\Delta t$, where Var again denotes the variance of a random

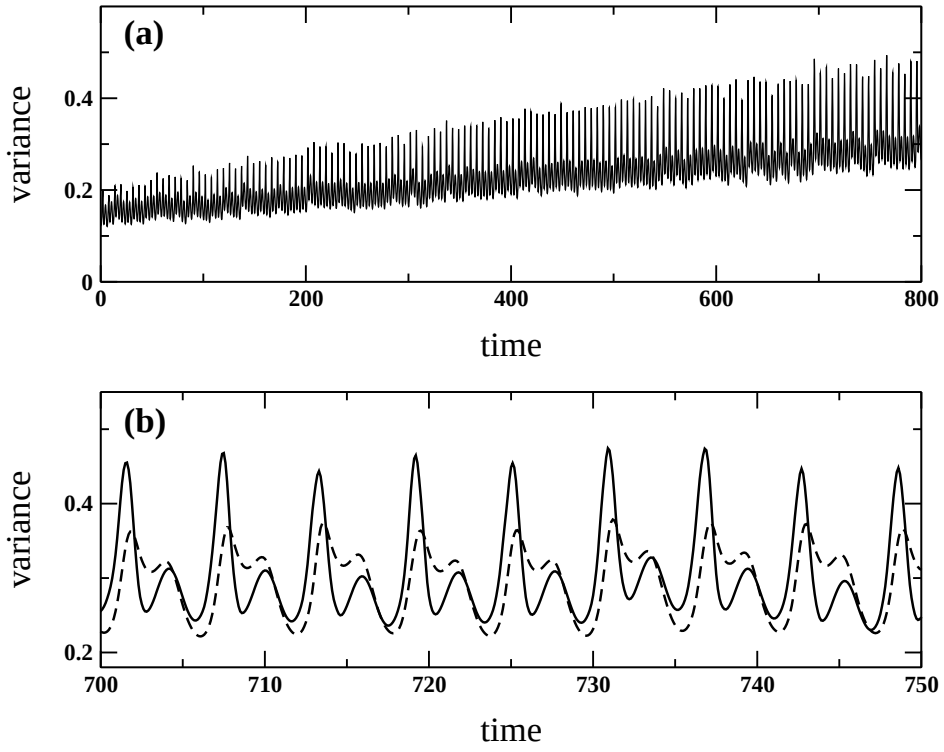

Figure 3.3: (a) Variance evolution over a sample of 1000 independent Rössler systems. (b) Same as (a) within a time window of 700-750 (solid line). The dashed line indicates the modeled variance of the phase fluctuations.

variable. Since $\lim_{\Delta t \to 0} \tau = \lim_{\Delta t \to 0} (\omega \Delta t + \phi_t) = \phi_t$:

$$D_{A_t,\phi_t} = \frac{1}{A_t^2 \cos^2(\phi_t) \left(1 + \kappa_t^2\right)^2} \left(\kappa_t^2 D_x + D_y\right) \ . \tag{3.13}$$

If $a \ll 1$ then $\omega \approx 1$ and thus Eq. (3.13) reduces to

$$D_{A_t,\phi_t} \approx \frac{\sin^2(\phi_t)\ D_x + \cos^2(\phi_t)\ D_y}{A_t^2} \ .$$

The variance of the system's phase $\varphi(t)$ at time t can then be approximated by

$$\mathrm{Var}(\varphi(t)) \approx \mathrm{Var}(\varphi(0)) + D_{E[A_t],E[\varphi(t)]} \cdot t \ , \tag{3.14}$$

where $\mathrm{Var}(\varphi(0)) \neq 0$, $E[A_t]$ is the mean amplitude and $E[\varphi(t)]$ the mean phase.

To check the validity of the model assumptions, the variance evolution over a sample of 1000 independent Rössler systems is simulated. The time step is chosen to be $\Delta t = 0.1$. Fig. 3.3a shows an increasing (in mean) variance of the phases, superposed by some spiking behavior. The diffusion constants D_x, D_y in Eq. (3.14) are fitted to the simulations using a linear fit algorithm [14]. The identified parameters are $D_x = 0.0089 \pm 4 \cdot 10^{-6}$,

$D_y = 0.0092 \pm 6 \cdot 10^{-6}$, thus different from zero. A comparison of the modeled variance, Eq. (3.13), with the simulation is shown in Fig. 3.3b. The comparison shows that our model captures most of the structure but the modeled variance evolution seems to be low-pass filtered. This effect is probably due to the assumed diffusion constants in the x-y plain which are not depending on the state of the system. The constants D_x, D_y are therefore representing mean diffusion coefficients leading to a smoother curve for the variance evolution of the fluctuations. Beside the phase fluctuations emerging from the system's equations, a contribution of numerical noise is always present in the simulations. This noise corruption is contained in the identified coefficients D_x and D_y. The chosen integration accuracy $\varepsilon = 10^{-12}$ gives a rough estimate on the numerical error of each time step Δt, see e.g. [14]. Note that ε cannot be made arbitrarily small, because if ε is close to the machine precision the number of internal steps for integrating the whole time step Δt diverges. Since $\varepsilon^2/\Delta t$ is several orders of magnitude smaller than D_x and D_y, contributions from the numerical error can be neglected in our analysis.

So far, we have derived an approximation of the phase dynamics by a diffusive process. It should now be shown that such phase diffusion satisfies the mixing condition of Eq. (3.1). This is one implication which can be drawn from the derivation of the significance level in Chapter 2. Nevertheless, the mixing condition is now explicitly verified to underline the following argumentation. To this end, suppose that the diffusion is constant, such that the sampled phase evolution reads

$$\varphi_{k+1} = \varphi_k + \omega\Delta t + \sqrt{D\Delta t}\ \epsilon_k\ , \tag{3.15}$$

for some $D \neq 0$ and ϵ_k is again a sequence of uncorrelated white noise. Starting at φ_0 and taking the wrapped phase $\phi_k = \varphi_k \bmod 2\pi$ to gain a stationary process, the conditional probability density $\rho(\phi_\infty|\varphi_0) = \lim_{k\to\infty}\rho(\phi_k|\varphi_0)$ is thus

$$\begin{aligned}\rho(\phi_\infty|\varphi_0) &= \lim_{k\to\infty}\frac{1}{\sqrt{2\pi D\Delta t k}}\sum_{j=-\infty}^{\infty}\exp\left(-\frac{(\omega\Delta t k+\varphi_0-\phi_k-2\pi j)^2}{2D\Delta t k}\right)\\ &= \frac{1}{(2\pi)^{3/2}}\int e^{-t^2/2}\,dt = \frac{1}{2\pi}\ .\end{aligned} \tag{3.16}$$

Since $\rho(\phi_\infty|\varphi_0)$ does not depend on the initial value φ_0, the asymptotic independence in Eq. (3.1) is shown. Moreover, the same result holds for the phase difference of two independent processes, and therefore $R_{1,1} = 0$. If D is not constant with respect to sampling point of index k but greater than zero, the result of Eq. (3.16) does not change.

Extracting the mean diffusion constant of about $D_{phase} = 2.1 \cdot 10^{-4}$ from Fig. 3.3, the presence of the finite size effect for the synchronization analysis can be verified for the most simple model given in Eq. (3.15). In order to compare the outcome with the results presented in Sec. 3.3, the parameters are chosen to be $\Delta t = 0.01$, $\omega = 1$, and $N = 131072$. The distribution of the mean phase coherence $R_{1,1}$ is shown in Fig 3.4. Since almost all mass is close to unity the finiteness of the amount of data has a predominant effect. Additionally, the value in case of the Rössler system $R_{1,1} = 0.92$ lies within the distribution but is slightly

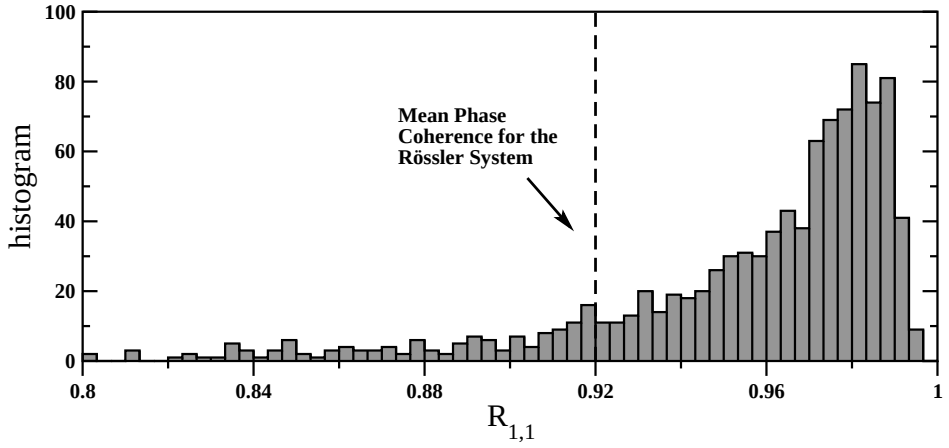

Figure 3.4: Distribution of the mean phase coherence $R_{1,1}$ for two independent processes of type (3.15). The parameters D, Δt, ω and the amount of data N are chosen to allow a comparison of the results presented in Sec. 3.3. This comparison is indicated by the dashed line showing the mean phase coherence for the noise-free Rössler system under this parameterization.

smaller than the mean mean phase coherence of the simplified model. This situation is exactly what one expects, because the bursts in the local diffusion rate destroy auto-correlations of the process. Due to Eq. (3.11) finite size effects are therefore slightly reduced. This positive result supports the strong presence of effects due to the finite amount of data. Moreover, applying the test discussed in Chapter 2 yields for this specific setting a critical value of about 4.6×10^7, where a 5% level of significance is chosen. Since this value is clearly above one, the test procedure cannot be applied. But the test statistics can be used to calculate the minimal amount of data to obtain meaningful critical values. It turns out that if $N > 1.33 \times 10^7$, the critical value for the 5% level of significance stays below one. Such a sample size calculation only yields reliable results if the diffusion constant of the phase can be determined.

3.5. Conclusion

The discussion about the phase evolution for the Rössler system has a long history. Crutchfield et al. [44] claimed that the attractor topology is mainly responsible for the sharp peak, namely that trajectories are revolving a single hole. This conjecture cannot hold in general, because the peak of the Rössler system is much broader when, e.g., the parameters are chosen to be $a = b = 0.2$, $c = 13$. The attractor topology remains the same in this setting. An intermittent behavior of the phase was discussed but this hypothesis was rejected afterwards [45-47]. Recently, Anishchenko et al. determined an effective diffusion coefficient by fitting Lorentzian to peaks in the power spectrum [48-50]. The presented work therefore supports their hypothesis that the chosen length of the time series is sufficiently large such that the spectral line width can be resolved.

A model of the phase fluctuations for the Rössler system has been derived from the

system's equations mainly under the assumptions of diffusion. Properties of this model are compared to simulated data. We have shown that the model captures the qualitative feature of the data. The diffusion constants derived from the model fitted to the data are significantly different from zero. In addition, a simplified but definitely mixing model of the phase evolution shows almost the same spurious mean phase coherence and the results from the test statistics derived in Chapter 2 shows that it is far away from its asymptotic accuracy for the given simulations. From the determined diffusion constant of the phase an approximate lower bound of the sample size can be determined, such that the test can be applied. These results are suggesting that the Rössler system for the chosen set of parameters is mixing. However, the rate of mixing is extremely low, explaining the spurious results for the cross-spectral and the synchronization analysis as finite size effects.

4

Strong Mixing in Sequences of Random Graphs and its Asymptotical Degree Distribution

4.1. Introduction

Random graphs are widely used to model real-world networks of high complexity. Such a random graph usually consists of a set of n labelled vertices, connected by m edges. The pair of vertices linked by an edge is selected with respect of some random process. Commonly, the evolution of these graphs are studied in the "thermodynamic" limit $n \to \infty$. One of the most basic feature of random graph processes is the degree distribution of vertices, namely the probability of a given total number of links leaving or approaching the vertex. Generally, the probability is determined for each vertex and obtained from the ensemble of graphs. Often the asymptotic degree distribution is independent of the vertices. In that case the underlying process is called degree stationary. Analogue to the stationarity of the distribution at every time point for time-series of ergodic processes, degree stationarity plays an important rôle for their analysis on the basis of measured data. This is due to the possibility that the degree distribution can be obtained from a single realization of the graph generating process, e.g., by the histogram of the observed degree over the vertices. However, there is no need that degree stationarity must be explicitly fulfilled for the following results but is mostly needed when treating random graphs on an empirical basis. Before introducing the main subject of this Chapter two important graph evolution processes are briefly discussed.

First, the most simple model of a graph process is the choice of m undirected edges from the whole set of $\binom{n}{2}$ undirected pairs, introduced by Erdős and Rényi [51, 52]. The edges are selected independently and with equal probability. It turns out that the degree distribution converges to a Poisson distribution for an appropriate choice of m with respect

to the number of vertices n. A similar model, introduced by Gilbert [53], also shows a Poissonian degree distribution. These models have in common that they describe a graph evolution which is completely independent from their predecessors. Beside the simple way the graphs are generated, they show an immense richness of mathematical properties as the work of Erdős and Rényi shows. Second, an exemplary process recently proposed by Barabási and Albert [54-56] shows a degree distribution which obeys a power law $P(d) \sim d^{-\gamma}$. Here, the so called preferential attachment is used as graph generating process for this exemplary process. In this case, a new vertex is added to the graph in each generation. A single edge is then drawn from the new vertex to a randomly chosen vertex of the preexisting graph. The probability with which the endpoint of this edge is chosen is proportional to the degree of the vertices. Thereby, this process motivates the term preferential attachment since vertices of high degree are preferred in every stage the graph is build. Interestingly, this process can be related or transformed to a Erdős and Rényi graph such that the degree distribution can exactly be derived as shown in [57]. It turns out that the characteristic exponent of the degree distribution $P(d) \sim d^{-\gamma}$ is $\gamma = 3$. Since the power law does not contain a characteristic scale, Barabási and Albert called graphs possessing a power law tail as being scale-free. In contrast to the first example, the Erdős and Rényi random graphs, statistical dependencies between the selected edges arises which is the crucial point for mathematical analysis presented in Sec. 4.3.

Scale-free degree distributions have been observed for a large amount of real-world networks such as the Internet, WWW, social and biological networks, [56, 58, 54, 59, 60]. This predominate occurrence of scale-free networks compared to the graph generating process suggested by Erdős and Rényi is probably due to the more realistic generation process. However, this was remarked by Erdős and Rényi themselves, in [52] they write: "Of course, if one aims at describing such a real situation, one should replace the hypothesis of equiprobability of all connection by a more realistic model". Similar to the central limit theorem and its generalization to stable limit laws, see e.g. [22], there might also exists a domain of attraction to scale-free networks. This question is partially answered in Sec. 4.3. Since such a question can only treated in a mathematically rigorous way, the structure of this Chapter differs significantly from the others. It is therefore necessary to define all elements used to built the general mathematical structure, which is accomplished in Sec. 4.2. Finally, the consequences of the derived results are discussed in Sec. 4.4

4.2. The Model and Basic Definitions

The evolution of the regarded random graphs are given by a discrete time stochastic process on a space Ω, $\big(\Omega, \mathcal{F}, P, (G^{n,m(n)})_{n\geq 1}\big)$, where the σ-algebra $\mathcal{F}$ is generated by the $n \times n$ matrices $G^{n,m(n)}$, having entries $g_{ij}^{n,m(n)} \in \{0, 1\}$. Again, the total number of vertices is denoted by n, the number of edges depending on n is given by $m(n)$, whereas $m(n) \to \infty$ if $n \to \infty$. A pair of vertices (i, j) is linked from vertex i to vertex j only if $g_{ij}^{n,m(n)} = 1$. The full matrix $G^{n,m(n)}$ therefore defines a directed graph containing self-edges, an edge which links only one vertex. If a graph does not contain any self-edges, the diagonal of $G^{n,m(n)}$ is

omitted from the probability space. Additionally, all elements g_{ij} are identified with g_{ji} for undirected graphs.

The degree of vertex i at generation n is given by the random variable d_i^n, which is related to the random matrices $G^{n,m(n)}$ by $d_i^n = \sum_{j=1}^n \left(g_{ij}^{n,m(n)} + g_{ji}^{n,m(n)}\right)$ for directed and $d_i^n = \sum_{j=1}^n g_{ij}^{n,m(n)}$ for undirected graphs. Note that in each generation only one vertex is added to the graph. Moreover, the asymptotic degree distribution is said to regular if

$$d_i^n \xrightarrow{d} d_i \ , \quad n \to \infty \tag{4.1}$$

converges in distribution for all $i \in \mathbb{N}$. It turns out that the latter condition is of great importance in the discussion of asymptotic degree distribution since it excludes oscillating degree sequences and distributions having all its mass at infinity. An example, in which the distribution is not regular is given by the following process: suppose that $(X_i)_{i\geq 1} \in \mathbb{R}^p$ is a realization of an ergodic dynamical process. Then,

$$g_{ij}^{n,m(n)} = \begin{cases} 1 & \text{if } ||X_i - X_j|| \leq \epsilon \text{ for all } 1 \leq i,j \leq n \text{ and } i \neq j \\ 0 & \text{else} \end{cases} \ ,$$

for some $\epsilon > 0$. The non-regularity of the degree distribution is due to ergodicity of the dynamical process since by the invariant measure P, we obtain for each i that $P\big(\{x \in \mathbb{R}^p : ||X_i - x|| \leq \epsilon\}\big) > 0$. By the ergodic theorem [61, 62], we observe that $n^{-1}\sum_{j=1}^n g_{ij}^{n,m(n)} = O_p(1)$ and therefore $d_i^n = O_p(n)$. Hence, this example shows that the graph generating process has to chosen with care such that the regularity is guaranteed. Moreover, regularity is essential to extrapolate the degree law of a finite realization to its asymptotic distribution. In a similar fashion, the total degree distribution d^n at generation n is given by $P(d^n \leq k) = n^{-1}\sum_{i=1}^n P(d_i^n \leq k)$. Again, the asymptotic total degree distribution is regular if

$$d^n \xrightarrow{d} d \ , \quad n \to \infty \ . \tag{4.2}$$

Analog to the stationary time-series, a degree distribution is called asymptotically stationary if d_i in Eq. (4.1) is independent of each vertex i. This property plays and important rôle for the inverse problem but is not essential for the following mathematical treatment.

Inspired by the classical central limit theorem for real valued random variables a mixing condition is established. However, this condition has to be different from the mixing property introduced in chapter 2 since it turns out that the spatial rather than the temporal dependency structure is of importance for determining asymptotic degree distributions. Since there is no appropriate distance measure for capturing the spatial dependence structure, the following mixing condition is based on a partition of the graph into subgraphs. Subgraphs, rather than the vertices itself are used to provide a more general characterization of the graph generating process. If these subgraphs are asymptotically independent, the graph process is called mixing. Precisely, consider all partitions of $\{1, \cdots, n\}$ into l disjointed, non-empty sets $\mathcal{M}^{n,l}$. Thus, the number of elements of $\mathcal{M}^{n,l}$ is given by the recursion

$$N_p^{n,l} = \frac{l^n}{l!} - \sum_{k=1}^{l-1} \frac{1}{(l-k)!}\, N_p^{n,k} \qquad \text{and} \quad N_p^{n,1} = 1 \ . \tag{4.3}$$

Here, l^n is the total number of ordered l-partitions which is due to the multinomial series

$$l^n = \sum_{n_1,\cdots,n_l\geq 0\ ;\ n_1+\cdots+n_l=n} \frac{n!}{n_1!\ \cdots\ n_l!}\ .$$

Note that empty sets are also included. To exclude them, we distribute $l-k$ empty sets over the set of k non-empty partitions to count the contribution of the empty sets in l^n. This leads to $\frac{l!}{(l-k)!}\ N_p^{n,k}$ and is thus the total amount of ordered partitions having $l-k$ empty sets. Hence, the sum over all $l-1$ empty sets yields the desired contribution to be subtracted from l^n. Finally, the term $1/l!$ takes into account that the ordering of the l-partitioning is arbitrary. Now, decompose the set $\mathcal{M}^{n,l}$ into its subsets such that $\mathcal{M}^{n,l} = \{\mathcal{C}_1,\cdots,\mathcal{C}_{N_p^{n,l}}\}$. Each of the sets $\mathcal{C}_i$ then contains a distinct l-partitioning $\mathcal{C}_i = \{\mathcal{V}_1^i,\cdots,\mathcal{V}_l^i\}$. For a given partition $\mathcal{C}_i$ the function $g_{\mathcal{C}_i}(k)$ assigns each vertex $k\in\{1,\cdots,n\}$ to the number of the corresponding partition. For example, if vertex k lies in partition l, thus $k\in\mathcal{V}_l^i$, we obtain $g_{\mathcal{C}_i}(k)=l$. Let $\mathbb{1}_{\mathcal{A}}(k)$ denote the indicator function with respect to some set $\mathcal{A}$, which has the property that $\mathbb{1}_{\mathcal{A}}(k)=1$ if k is an element of $\mathcal{A}$ and zero otherwise. We can therefore represent $g_{\mathcal{C}_i}(k)$ by $g_{\mathcal{C}_i}(k)=\sum_{j=1}^{l} j\ \mathbb{1}_{\mathcal{V}_j^i}(k)$. For each $i,j\in\{1,\cdots,n\}$ and $\mathcal{C}_k\in\mathcal{M}^{n,l}$ consider the following σ-algebras:

$$\mathcal{F}_{ij} = \sigma(g_{ij}) \qquad \text{and}$$

$$\mathcal{F}_{ij}^{\mathcal{C}_k} = \begin{cases} \sigma\left(\bigcup_{r,s=1}^{n}\sigma(g_{rs}) \setminus \bigcup_{g_{\mathcal{C}_k}(r)=g_{\mathcal{C}_k}(s)=g_{\mathcal{C}_k}(i)}\sigma(g_{rs})\right) & \text{if } g_{\mathcal{C}_k}(i)=g_{\mathcal{C}_k}(j) \\ \sigma\left(\bigcup_{r,s=1}^{n}\sigma(g_{rs}) \setminus \sigma(g_{ij})\right) & \text{else} \end{cases}, \tag{4.4}$$

where $\sigma(\cdot)$ is the smallest σ-algebra either induced by a random variable or contains the given system of sets. The σ-algebra $\mathcal{F}_{ij}$ contains only the link between vertex i and j. However, the interpretation of $\mathcal{F}_{ij}^{\mathcal{C}_k}$ is more complex. If i and j are lying in the same partition with respect to $\mathcal{C}_k$, links within the partition are not measurable if the measure restricted to $\mathcal{F}_{ij}^{\mathcal{C}_k}$ is considered. But if i and j are lying in distinct partitions only the probabilistic information of the edge linking i with j is excluded in $\mathcal{F}_{ij}^{\mathcal{C}_k}$. This construction thus offers the possibility to measure statistical dependencies between the partitions where vertex i and j is located, thereby providing a suitable basis for the definition of mixing in sequences of random graphs. A sequence of random graphs is called strongly mixing if for some integer valued function $l(n)\leq n$,

$$\alpha_n^{l(n)} = \inf_{\mathcal{C}_k\in\mathcal{M}^{n,l(n)}} \sup\left\{|P(A\cap B)-P(A)P(B)| : 1\leq i,j\leq n, A\in\mathcal{F}_{ij}, B\in\mathcal{F}_{ij}^{\mathcal{C}_k}\right\} \tag{4.5}$$

satisfies

$$\lim_{n\to\infty}\alpha_n^{l(n)} = 0\ .$$

Since the following mathematical analysis is based on this definition, a closer explanation of the interpretation of Eq. (4.5) is desired. First, the sets A and B in Eq. (4.5) are possessing the following property: if $g_{\mathcal{C}_k}(i)=g_{\mathcal{C}_k}(j)$ the set B contains only links connecting other subgraphs than that of $g_{\mathcal{C}_k}(i)=g_{\mathcal{C}_k}(j)$. This is necessary to avoid that $|P(A\cap B)-P(A)P(B)|$ measures statistical dependencies between vertices of a single partition. The other case $g_{\mathcal{C}_k}(i)\neq g_{\mathcal{C}_k}(j)$

inherently excludes the possibility that statistical dependencies within a single partition is measured since the nodes i and j are lying in different partitions. The only link to be excluded in set B is that from i to j, since identical links in A and B are leading to $\alpha_n^{l(n)} > 0$. However, such a definition would not be suitable for our purpose. Second, by the infimum over all possible l-partitionings the best partition scheme is selected possessing the lowest statistical dependencies. Interpreting the partitions as subgraphs, $\alpha_n^{l(n)}$ therefore measures the statistical dependencies between subgraphs whereas the decomposition of the graph into l subgraphs is optimal with respect to its dependency structure.

With the aid of the mixing coefficient, defined by Eq. (4.5), we are going to state conditions for which the asymptotical degree distribution can be regarded as being scale-rich. The asymptotical degree distribution of node i, $P(d_i = k)$ for all $k \in \mathbb{N}_0$ is said to be scale-rich if there exists a rapidly varying function $h(x)$, such that $P(d_i = k)$ is dominated by h for all $k \geq k_0$. According to [63, 64], a positive, Lebesgue measurable function h on $(0, \infty)$ is referred to as rapidly varying (with index $-\infty$), say $h \in \mathcal{R}_{-\infty}$ if

$$\lim_{x\to\infty} \frac{h(tx)}{h(x)} = \begin{cases} 0 & \text{if } t > 1 \\ \infty & \text{if } 0 < t < 1 \end{cases} . \tag{4.6}$$

Degree distributions which can, e.g., be dominated by a homogeneous function h of degree α are not scale-rich because $h(tx) = t^\alpha\, h(x)$ violates Eq. (4.6). Therefore, power law degree distributions are not scale-rich. On the other side, if the tail of $P(d_i = k)$ can be approximated by a regularly varying function $h \in \mathcal{R}_{-\gamma}$, $\gamma \in \mathbb{R}$, namely a positive, Lebesgue measurable function satisfying

$$\lim_{x\to\infty} \frac{h(tx)}{h(x)} = t^{-\gamma}, \qquad t > 0 \,, \tag{4.7}$$

the corresponding degree distribution is called scale-free. Whereas, a positive function $f(x)$ approximates the tail of some positive function $g(x)$ if $|f(x)/g(x) - 1| = o(1)$ for $x \to \infty$ which is referred to as $f(x) \sim g(x)$. Note that each degree distribution having a finite maximal degree is inherently scale-rich and total degree distributions are treated in a similar way. In the following, we only regard directed graphs having no self-edges. The results based on this restricted set of graphs are basically the same as for a more general class, because the effects originating form self-edges or effects due to undirected links are asymptotically negligible.

4.3. Mixing Sequences of Random Graphs

The first result is based on the assumption that the mixing coefficient vanishes for all $n \geq n_0$. Therefore, between the partitions the edge distribution should be similar to that of Erdős and Rényi. If in addition, the maximal number of elements of the partitions approaches a finite number it is likely to obtain a scale-rich graph. Because the statistical independence of the subgraphs is satisfied for $n \geq n_0$, the generating function plays a major rôle in the following result. A generating function of a discrete probability distribution, e.g., p_k for all $k \in \mathbb{N}_0$, is

given by the series $g(s) = \sum_{k=0}^{\infty} p_k \; s^k$ for each $s \in \Omega \subset \mathbb{C}$ such that the series is convergent. Since the probability distribution is normalized: $g(1) = 1$ holds. Further properties of the generating functions are, e.g., that the moments of the distribution can be obtained by derivatives of g evaluated at $s = 1$ and like the Fourier series, a discrete convolution of two probability densities corresponds to the product of their generating functions. From the generating function $g(s)$, the distribution can be gained with aid of the residue theorem. Let C a be a closed curve in the complex plain around zero, then $p_k = (2\pi i)^{-1} \; \int_C g(s) \; s^{-(k+1)} \; ds$. After this brief survey of the properties of generating functions, we return to main subject of this section. For simplicity, let us write $p_{ij}^n = P(g_{ij}^{n,m(n)} = 1)$. Then,

Lemma 1. *If* $\alpha_n^{l(n)} = 0$ *for all* $n \geq n_0$, $n - 1 - l(n) = O(1)$ *and* $\lim_{n\to\infty} \sum_{j=1, i\neq j}^{n} (p_{ij}^n + p_{ji}^n) < \infty$ *for some* $i \in \mathbb{N}$, *then the asymptotic degree distribution of vertex* i *is scale-rich.*

Proof. Let $n \geq n_0$, $\mathcal{C}_n$ a partition for which Eq. (4.5) attains its minimum and $\mathcal{V}^n = \mathcal{V}^n_{gc_n(i)}$. The degree distribution of vertex i is now divided into the degree contributing from vertices within $\mathcal{V}^n$, $d_i^{in,n}$ and the links to or from outside of $\mathcal{V}^n$, denoted by $d_i^{out,n}$. We first show that $d_i^{out,n}$ is scale-rich. Since $\alpha_n^{l(n)} = 0$, the generating function of $d_i^{out,n}$ is given by

$$g_n(s) = \prod_{j \notin \mathcal{V}^n} (1 + p_{ij}^n(s-1))(1 + p_{ji}^n(s-1)) \quad \text{for all } n \geq n_0 \; .$$

Setting $\lim_{n\to\infty} g_n(s) = g(s) = \sum_{k=0}^{\infty} a_k s^k$ and $N(n) = 2\,(n - |\mathcal{V}^n|)$ which is maximal possible degree for $d_i^{out,n}$, the radius of convergence of $g(s)$ can be determined by

$$\begin{aligned}
|g(s)| &\leq \sum_{k=0}^{\infty} a_k |s|^k = g(|s|) \\
&= \lim_{n\to\infty} \prod_{j \notin \mathcal{V}^n} (1 + p_{ij}^n(|s|-1))(1 + p_{ji}^n(|s|-1)) \\
&\leq \lim_{n\to\infty} \left(1 + \frac{|s|-1}{N(n)} \sum_{j \notin \mathcal{V}^n} (p_{ij}^n + p_{ji}^n) \right)^{N(n)} \\
&= \exp\left(\lambda_i(|s|-1)\right) \; , \qquad (4.8)
\end{aligned}$$

where $\lambda_i = \lim_{n\to\infty} \sum_{j \notin \mathcal{V}^n} (p_{ij}^n + p_{ji}^n) < \infty$ and $N(n) \to \infty$ since $|\mathcal{V}^n|$ is bounded. In Eq. (4.8) a standard estimate of the geometric and the arithmetic mean is used. Thus, the power series of $g(s)$ converges for all $s \in \mathbb{C}$. We can further assume without loss of generality, that $a_k > 0$ for almost all $k \in \mathbb{N}_0$, otherwise $d_i^{out,n}$ is scale-rich and nothing is left to show. The convergence of a_k and $a_k > 0$ implies that $\limsup_{k\to\infty} a_{k+1}/a_k = 0$. Let b_k an appropriate sub-series such that $b_k > 0$ for all $k \in \mathbb{N}_0$ and $b_{k+1}/b_k \to 0$. Now, for some $0 < \epsilon < 1$ there exists a k_0 such that for all $k \geq k_0$, $0 \leq b_{k+1}/b_k \leq \epsilon$ is satisfied. Setting $h(x) = b_{[x]}$, where $[x]$ denotes the integer part of x, we have for all $t > 1$:

$$0 \leq h(tx)/h(x) = b_{[tx]}/b_{[x]} \leq \epsilon^{[x(t-1)]} \to 0 \quad \text{if } x \to \infty \; .$$

Analogously, $h(tx)/h(x) \to \infty$ for $0 < t < 1$ can be shown regarding $b_{[x]}/b_{[tx]}$. Therefore, b_k can be dominated by a rapidly varying function. Since $g(1) = 1$ and $0 \leq a_k \leq 1$, $a_k = \lim_{n\to\infty} P(d_i^{out,n} = k) = P(d_i^{out} = k)$ can thus be dominated by a rapidly varying function, thus d_i^{out} is scale-rich. Finally, $d_i = d_i^{in} + d_i^{out}$ and is the sum of two independent random variables and since $|\mathcal{V}^n|$ is bounded, the degree distribution of vertex i scale-rich.

□

Now, the conditions of lemma 1 are examined in detail. It is shown below that the condition $\lim_{n\to\infty} \sum_{j=1,i\neq j}^{n} (p_{ij}^n + p_{ji}^n) < \infty$ can be dropped if the degree distribution is assumed to be regular.

Lemma 2. *If the graph process satisfies* $\alpha_n^{l(n)} = 0$ *for all* $n \geq n_0$, $n - 1 - l(n) = O(1)$ *and the degree distribution is regular then* $\lim_{n\to\infty} \sum_{j=1,i\neq j}^{n} (p_{ij}^n + p_{ji}^n) < \infty$ *for all* $i \in \mathbb{N}$.

Proof. Assume that $\sum_{j=1,i\neq j}^{n} (p_{ij}^n + p_{ji}^n) \to \infty$ for some $i \in \mathbb{N}$. By using the same notation as introduced in lemma 1 and the estimate, Eq. (4.8), of $|g(s)|$, we have $g(s) = 0$ for all $s \in \mathbb{C}$ satisfying $|s| < 1$. Consider a closed curve C inside the unit circle and around zero, thus by the residue theorem we obtain

$$\lim_{n\to\infty} P(d_i^{out,n} = k) = a_k = \frac{1}{2\pi i} \int_C \frac{g(s)}{s^{k+1}}\, ds = 0 \;, \quad \text{for all } k \in \mathbb{N}_0 \;.$$

Consequently, the degree distribution is not regular since all mass of $\lim_{n\to\infty} d_i^{out,n}$ is concentrated at infinity. It should be noted that contributions from $d_i^{in,n}$ can again be neglected asymptotically, because the convolution of the distributions $d_i^{in,n}$ and $d_i^{out,n}$ shifts the total mass to infinity since the distribution $d_i^{in,n}$ has a finite maximal degree by $n-1-l(n) = O(1)$.

□

The condition $\lim_{n\to\infty} \sum_{j=1,i\neq j}^{n} (p_{ij}^n + p_{ji}^n) < \infty$ can therefore be replaced by the demand that the degree distribution is regular. However, the condition $n-1-l(n) = O(1)$ is essential for establishing a scale-rich degree distribution as in lemma 1. In order to demonstrate this statement, consider the extremal situation, where both $l(n) \to \infty$ and $n-1-l(n) \to \infty$, e.g., $l(n) = O(\sqrt{n})$. According to the proof of lemma 1, d_i^{out} is still scale-rich since $N(n) \to \infty$. Let us further assume that d_i^{in} is scale-free, namely that there exists a regularly varying function $h \in \mathcal{R}_{-\gamma}$ satisfying $0 < P(d_i^{in} = k) \sim h(k)$. This, however, is possible because some subgraphs may accumulate an infinite number of vertices in the limit $n \to \infty$. Let $g(z)$ be the generating function of d_i^{out} and $f(z)$ the generating function of d_i^{in}. Since $f(z) = \sum_{k=0}^{\infty} b_k\, z^k$ has a finite radius of convergence, $b_{k-1}/b_k \to z_0$ as $k \to \infty$. Applying theorem 2 of [65] we have for $g(z)f(z) = \sum_{k=1}^{\infty} c_k\, z^k$, $c_k \sim g(z_0)\, b_k$. For $n \geq n_0$ the independence of d_i^{out} and d_i^{in} yields $P(d_i = k) = c_k \sim g(z_0)\, b_k$ is scale-free. The assumption $n - 1 - l(n) = O(1)$ is therefore essential to gain a scale-rich graph under the conditions of lemma 1. Thus, we can state the following corollary:

Corollary 1. *If* $\alpha_n^{l(n)} = 0$ *for all* $n \geq n_0$, $n-1-l(n) = O(1)$ *and the degree distribution is for some vertex* $i \in \mathbb{N}$ *is regular, then the asymptotic degree distribution of node* i *is scale-rich.*

At this point let us consider the more general situation that the mixing coefficient $\alpha_n^{l(n)}$ only vanishes asymptotically. It turns out, however, that $\alpha_n^{l(n)}$ cannot arbitrarily scale with respect to n. This is manly due to the increased number of combinations contributing to the same degree whenever n increases. We state the following theorem:

Theorem 1. *If $\alpha_n^{l(n)} = o(n^{-1/2}\ 2^{-n})$, $n-1-l(n) = O(1)$ and the degree distribution is for some vertex $i \in \mathbb{N}$ is regular, then the asymptotic degree distribution of node i is scale-rich.*

Proof. Again, consider for some vertex $i \in \mathbb{N}$ the random variables $d_i^{out,n}$, $d_i^{in,n}$ and the set $\mathcal{V}^n$ as defined in lemma 1. Further, let $\tilde{d}_i^{out,n}$ be the a random variable having a distribution uniquely determined by the generating function $g_n(s)$ which is also defined in lemma 1. Therefore, the distribution of $\tilde{d}_i^{out,n}$ describes the analogue situation for which all statistical dependencies are removed and according to corollary 1, $\tilde{d}_i^{out,n}$ converges to a scale-rich distribution. On the other side, the distribution $P(d_i^{out,n} = k)$ which takes the statistical dependencies into account is determined by the sum of all

$$P(e_1, \cdots, e_{2(n-|\mathcal{V}^n|)}) = P\left(\{g_{ij_1}^{n,m(n)} = e_1\} \cap \cdots \cap \{g_{j_{2(n-|\mathcal{V}^n|)}i}^{n,m(n)} = e_{2(n-|\mathcal{V}^n|)}\}\right) ,$$

where both $\{j_1, \cdots, j_{n-|\mathcal{V}^n|}\}$, $\{j_{n-|\mathcal{V}^n|+1}, \cdots, j_{2(n-|\mathcal{V}^n|)}\}$ are denoting the labels of all vertices in $\{1, \cdots, n\} \setminus \mathcal{V}^n$ and $e_j \in \{0,1\}$ satisfying $\sum_{j=1}^{2(n-|\mathcal{V}^n|)} e_j = k$. By setting $N(n) = 2\ (n-|\mathcal{V}^n|)$ and $P_{j_k} = P\left(g_{ij_k}^{n,m(n)} = e_{j_k}\right)$ an estimate of $\mathcal{B}_n = \left|P(e_1, \cdots, e_{N(n)}) - \prod_{k=1}^{N(n)} P_{j_k}\right|$ is given by

$$\begin{aligned}
\mathcal{B}_n &= \left|P(e_1, \cdots, e_{N(n)}) - P_{j_1} \cdot \prod_{k=2}^{N(n)} P_{j_k}\right| \\
&= \left|P(e_1, \cdots, e_{N(n)}) - P_{j_1} \cdot P(e_2, \cdots, e_{N(n)}) + P_{j_1} \cdot \left(P(e_2, \cdots, e_{N(n)}) - \prod_{k=2}^{N(n)} P_{j_k}\right)\right| \\
&\leq \underbrace{\left|P(e_1, \cdots, e_{N(n)}) - P_{j_1} \cdot P(e_2, \cdots, e_{N(n)})\right|}_{\leq\ \alpha_n^{l(n)}} + \underbrace{P_{j_1}}_{\leq 1} \cdot \left|\left(P(e_2, \cdots, e_{N(n)}) - \prod_{k=2}^{N(n)} P_{j_k}\right)\right| \\
&\leq \alpha_n^{l(n)} + \left|\left(P(e_2, \cdots, e_{N(n)}) - \prod_{k=2}^{N(n)} P_{j_k}\right)\right| \leq \ldots \leq (N(n)-1)\ \alpha_n^{l(n)} \qquad (4.9)
\end{aligned}$$

The sum of all $\binom{N(n)}{k}$ combinations satisfying $\sum_{j=1}^{2(n-|\mathcal{V}^n|)} e_j = k$ the yields an upper bound for $\mathcal{D}_n = \left|P(d_i^{out,n} = k) - P(\tilde{d}_i^{out,n} = k)\right|$. Since the right hand side of Eq. (4.9) does not depend on the e_j's, we arrive at

$$\mathcal{D}_n \leq \binom{N(n)}{k}(N(n)-1)\ \alpha_n^{l(n)} \leq \binom{N}{N/2}(N-1)\ \alpha_n^{l(n)} .$$

Using Stirling's formula $N! = \sqrt{2\pi N}\left(\frac{N}{e}\right)^N \left(1 + O(N^{-1})\right)$ to approximate $\binom{N}{N/2}$ by

$$\binom{N}{N/2} = \frac{N!}{(N/2)!\ (N/2)!} = \sqrt{\frac{2}{\pi N}}\ 2^N\ \left(1 + O(N^{-1})\right)$$

and therefore

$$\mathcal{D}_n \leq \sqrt{\frac{2}{\pi}}\ \sqrt{N}\ 2^N\ \alpha_n^{l(n)}\ \left(1 + O(N^{-1})\right)\ . \tag{4.10}$$

Since $\alpha_n^{l(n)} = o(n^{-1/2}\ 2^{-n})$, Eq. (4.10) yields $\lim_{n\to\infty} \mathcal{D}_n = 0$ and therefore $d_i^{out,n} \xrightarrow{d} \tilde{d}_i^{out,n}$. Hence, it is possible to dominate $\lim_{n\to\infty} P(d_i^{out,n} = k) = P(d_i^{out} = k)$ by a rapidly varying function and since $|\mathcal{V}^n|$ is bounded, the degree distribution of vertex i is scale-rich. □

Theorem 1 states that under the given conditions vertex i of a graph process evolves to a scale-rich degree distribution. Consider the case that each vertex of the graph is having a regular degree distribution. Then under the conditions of theorem 1, the degree distribution of each vertex converges to a scale-rich distribution. However, if the total degree distribution is considered, the conditions above are not sufficient. Despite that $\lambda_i = \lim_{n\to\infty} \sum_{j=1,j\neq i}^{n} (p_{ij}^n + p_{ji}^n) < \infty$, λ_i may satisfy $\lambda_i \to \infty$ if $i \to \infty$. To exclude this situation, the assumption that the total degree is regular, Eq. (4.2), turns out to be sufficient. This leads to:

Theorem 2. *If $\alpha_n^{l(n)} = o(n^{-1/2}\ 2^{-n})$, $n-1-l(n) = O(1)$, the degree distributions for all vertices are regular and the total degree distribution is regular, then the total degree distribution is asymptotically scale-rich.*

Proof. Analogue to the proof of lemma 1, let $\lim_{n\to\infty} g_n^i(s) = g^i(s)$ be the asymptotic generating function of d_i^{out} for vertex i. Let further d^{out} be defined by $P(d^{out} = k) = \lim_{n\to\infty} n^{-1} \sum_{i=1}^{n} P(d_i^{out,n} = k)$ and which posses the generating function $h(s)$. An upper bound of $|h(s)|$ is

$$|h(s)| \leq \lim_{n\to\infty} n^{-1} \sum_{i=1}^{n} g_n^i(|s|) \leq \lim_{n\to\infty} n^{-1} \sum_{i=1}^{n} \exp\left(\lambda_i(|s| - 1)\right)\ ,$$

where λ_i is again given in lemma 1. Let us assume that the sequence $(\lambda_i)_{i\in\mathbb{N}}$ is not bounded, because in the opposite case d^{out} is scale-rich using the same argumentation of lemma 1. Setting $x_i = \exp\left(\lambda_i(|s| - 1)\right)$, thus for $|s| < 1$ we have $x_i \to 0$ if $i \to \infty$ since λ_i diverges. By a theorem of Toeplitz, the convergence of x_i to zero implies

$$|h(s)| \leq \lim_{n\to\infty} n^{-1} \sum_{i=1}^{n} x_i = \lim_{n\to\infty} x_n = 0\ .$$

Again, from the residue theorem can be concluded that $P(d^{out} = k) = 0$ for all k. The process does not yield a regular distribution which is a contradiction to the assumption. Therefore, the sequence $(\lambda_i)_{i\in\mathbb{N}}$ is bounded and the total-degree converges to a scale-rich distribution. □

If the asymptotic degree distribution is stationary as defined in Sec. 4.2, the whole situation simplifies significantly. Since the asymptotic distribution d_i is invariant with respect to the vertex i, the total degree distribution coincides with the distribution for each individual vertex in the asymptotic limit $n \to \infty$. Theorem 1 and 2 can therefore be merged in the following manner: suppose that the asymptotic degree distribution is asymptotically stationary and the mixing coefficient satisfies $\alpha_n^{l(n)} = o(n^{-1/2}\ 2^{-n})$ where $n - 1 - l(n) = O(1)$, then limit distribution is scale-rich. Consequences of the these results are now discussed in the following section.

4.4. Discussion and Conclusion

So far, based on a definition of strongly mixing graphs a limit theorem for scale-rich degree distributions is established. Here, the notion scale-rich and scale-free is solely based on the behavior of the degree distribution. Precisely, if the degree distribution scales according to a power law or the distribution can asymptotically be approximated by a regular varying function, the resulting network is called scale-free. Otherwise, if the degree distribution can be dominated by a rapidly varying function, the graph is called scale-rich. However, there is not a commonly accepted definition of scale-free networks or graphs in the literature. Additional network specific signatures are often consulted for this purpose which are mainly based on the analysis of graphs obtained by preferential attachment, see e.g. [66, 56, 67, 54, 55, 68, 69]. In this chapter, we restricted our attention only on the asymptotic degree distribution of probabilistic graph processes and therefore reduce the definition of scale-free and scale-rich networks only to this feature. In the following discussion of the results three issues are addressed: first, the relation of the defined strong mixing condition to a preexisting measure of the dependence structure, second, the motivation to incorporate finite subgraphs into $\alpha_n^{l(n)}$, and third, possible implications for real networks such as protein interaction networks.

Let us address the first issue: Assortative/disassortative mixing introduced by Newman in [70] is based on degree correlations of the vertices. In order to measure these correlations, a quantity r is defined which is strongly related to the Pearson's correlation coefficient. According to Eq. (4) in [70] this quantity can be calculated using

$$r = \frac{m^{-1}\sum_{i=1}^{m} j_i k_i - \left(m^{-1}\sum_{i=1}^{m}(j_i + k_i)/2\right)^2}{m^{-1}\sum_{i=1}^{m}(j_i^2 + k_i^2)/2 - \left(m^{-1}\sum_{i=1}^{m}(j_i + k_i)/2\right)^2}\ , \tag{4.11}$$

where j_i, k_i are the degrees of the vertices at the ends of edge i. The normalization in Eq. (4.11) is chosen that r can attain values within the range $-1 \leq r \leq 1$, like the usual correlation coefficient. A graph having $r > 0$ is called assortative mixing whereas a graph possessing $r < 0$ is said to be disassortative mixing. This might be interpreted as follows, if on one side high degree vertices are attached with preference to vertices also having a high degree then assortative mixing is expected. On the other side, high degree vertices are preferentially attached to low degree vertices disassortative mixing should be observed. These properties of r are, e.g., used to study synchronization on complex networks [71] but are not useful to discriminate scale-free and scale-rich limit distributions. In [70] it is, e.g., shown that both,

the preferential attachment as introduced by Barabási and Albert and the Erdős and Rényi model are having $r = 0$. Moreover, an algorithm can be constructed to obtain a variety of scale-free graphs having $r = 0$, see [72]. Reasons that scale-free and scale-rich graphs cannot be distinguished from the value of r is that second moments are not sufficient to capture the entire statistical dependency structure which is also similar in the case of the classical central limit theorem. Even more important, due to aggregation obtained by calculating the degree distribution the desired information to discriminate scale-free from scale-rich degree distributions is destroyed.

Second, the motivation to introduce finite subgraphs into the mixing condition is mainly driven by the occurrence of network motifs in biochemical relations, see e.g. [73-76]. These motifs are highly conserved modules of networks occurring at a significantly higher rate than one would expect to observe these structures at random. Not only in biological networks one would expect to see these motifs but also in artificial networks like electronic circuits. Network motifs can be regarded as building blocks which carry most of the network's functionality. Since these highly correlated substructures are usually finite in size, e.g., not larger than five nodes for the protein interaction network in yeast [75], these motifs do not alter the asymptotical degree distribution as shown above. In contrast, they would spoil the mixing coefficient $\alpha_n^{l(n)}$ if not taken into account. It is thus necessary to incorporate the possibility of having highly dependent subgraphs into $\alpha_n^{l(n)}$ to obtain more general results.

Third, consequences of the given theory are presented in the following. Let us first address the problem that usually the picture of a network is incomplete, where certain vertices are left out due to the impossibility to measure all components of the graph. This lack of information can be regarded as sampling of the underlying graph which is also studied in [77]. In this study the authors come to the conclusion that due to the sampling of the network a different degree distribution can be observed rather than the real underlying distribution. Using the presented theory, this result can also be obtained. Consider that the underlying graph is exhibiting a scale-free degree distribution. Unfortunately, the sampling scheme destroys central statistical dependencies such that the mixing coefficient of the sampled graph would satisfy $\alpha_n^{l(n)} = o(n^{-1/2}\ 2^{-n})$. By theorem 1 or 2 the sampled graph shows a scale-rich degree distribution even though the real underlying distribution is scale-free. However, in real networks this is likely not happen because strongly correlated motifs are generally the central components gluing the motifs together in order to achieve the network's function as whole. Missing these components therefore results in a complete lost of function of the network. This might prevent the usage of an inappropriate sampling scheme. As second consequence, consider that there is an evidence that the graph of interest is scale-free. Reverting the assertions of the presented theorems leads to the fact that the statistical dependencies between some finite subgraphs are scaling at a rate slower than $n^{-1/2}\ 2^{-n}$, where n is the network size. It is therefore possible to gain some insights of the evolution of the dependency structure by the classification of the degree distribution in either scale-free or scale-rich distributions. As example, graphs following preferential attachment are preserving inter vertex correlations.

In summary, a theory based on a definition of strong mixing in sequences of random graphs is presented. It is shown that this theory is capable to distinguish scale-rich behavior from

scale-free behavior on the basis of the scaling of the mixing coefficient $\alpha_n^{l(n)}$ with respect to the total amount of vertices n. Motivated from the occurrence of highly correlated network motifs in biological systems, only statistical dependencies between finite subgraphs are measured by $\alpha_n^{l(n)}$ to generalize the results. Consequences of this theory are also discussed with respect to the problem that most of the observed networks are not complete but sampled. It is argued that this sampling can destroy correlations which may alter the degree distribution of the observed graph. The presented theory can be seen as a first step toward a limit theorem for degree distributions of complex networks. Furthermore, the rather strict conditions to obtain a scale-rich degree distribution suggests the predominate occurrence of scale-free graphs.

5

Parameter Estimation in Differential Equations with Application to Biochemical Processes

5.1. Introduction

Processes involved in biochemical networks are currently far too complex to be approached on a fundamental basis, e.g., using quantum chemistry. Based on various well accepted simplifying assumptions, phenomenological models are used to achieve a deeper insight of the intra-cellular organization and its functionality. Basically, there are three different levels of abstraction which differ on the specific regime the models intend to describe. These are, stochastic gene expression models, e.g. [78], spatially inhomogeneous deterministic models, e.g. [79], and spatially homogeneous models, e.g. [80]. In this Chapter we focus on the latter mode of describing intra-cellular processes which is frequently used in signal transduction networks. For this specific type, it is necessary to assume that the involved chemical reactions are operating on time scales which are large compared to the diffusion of the substances. In that case, the substances of interest can be regarded as being well stirred such that no spatial effects are playing an important rôle. Additionally, the number of involved molecules has to be high enough in order to neglect stochastic fluctuations. Under these general assumptions, the biochemical reactions can be modeled with a system of ordinary differential equations (ODEs).

Usually, a priori information obtained from biochemical experiments is used to translate the knowledge of the process into a system of ODEs. Sometimes the perception of biochemical process is incomplete or debated such that various models can be proposed. On the basis of general design properties paired with a mathematical analysis some of these models can often be abolished, such a procedure is, e.g., followed in [81]. If quantitative experimental data

about the system is available, a model selection of alternative models and the verification of the best model in terms of goodness of fit can be proceeded. This procedure leads directly to the problem of estimating the parameters as well as the initial conditions in ODEs. Due to the following items it is a challenging task: first, usually a limited number of substances in a living cell can be observed and that these measurements are in general corrupted with noise. The procedure should be able to cope with partially observed, noisy data. Second, the involved optimization of estimating the parameters is highly non-linear and non-convex. Thereby, the problem of ending up in a local optimum arises. And forth, often not all parameters can be estimated for the given data set. The possible parameter combinations, leading to the optimum, are no longer a single point but usually a manifold such that a certain fixation of the estimates has to be done, either in advance or by the estimation method itself. There are several different approaches which meet these requirements or at least most of them. These approaches mostly differ from the optimization method they use. Possible optimization routines can be classified into global or local procedures. Methods based on global minimization routines are, e.g., random search and adaptive stochastic methods [82-85], clustering methods [86], evolutionary computation [87] and simulated annealing [88]. A detailed discussion of these methods with respect to parameter identification in ordinary differential equations is given in [89]. The disadvantage of stochastic optimizers is mainly their immense computational cost which is the price for the flexibility and stability of these methods. On the other side, local optimization procedures such as sequential quadratic programming (SQP), Newton methods, quasi-Newton methods, are computationally efficient but they tend to converge to local minima. In case of parameter identification in ODEs the problem of convergence to local minima is predominant if the so called initial value approach is considered. This approach utilizes the fact that the trajectory is uniquely determined by the parameters and initial values. In the following section this method is described in detail.

The situation stated above further suggests that there is a trade-off between computational efficiency and stability for estimating parameters in ODEs. In comparison to the initial value approach, the proposed method, multiple shooting provides enhanced stability with only a slight increase of the computational cost. The method was introduced in [90] and was substantially enhanced and mathematically analyzed by Bock [91-93]. The main idea of the method is to introduce more flexibility to search the optimal parameters. This is done by allowing discontinuous trajectories during the optimization process. Continuity of the trajectories is only forced at convergence to obtain a regular solution of the ODE. By utilizing such a strategy, the method can stay closer to the measurements and uses their information more efficiently. A detailed discussion of multiple shooting is given in Sec. 5.3 and an extension to the aforementioned problem that not all parameters can be estimated, non-identifiable problems, is presented in 5.4. To undermine the superior properties of the proposed method over the classical initial value approach the results from a simulation study are presented in Sec. 5.5. Finally, an application to *in vivo* measurements of a prominent signal transduction network is given in Sec. 5.6.

5.2. The Estimation Problem

Suppose that a dynamical system is given by the d-dimensional state variable $x(t) \in \mathbb{R}^d$ at time $t \in I = [t_0, t_f]$, which is the unique and differentiable solution of the initial value problem

$$\dot{x}(t) = f(x(t), t, p) \qquad x(t_0) = x_0 \; . \tag{5.1}$$

The right-hand side of the ODE depends on some parameters $p \in \mathbb{R}^{n_p}$. It is further assumed that f is continuously differentiable with respect to the state x and the parameters p. Let Y_{ij} denote the data of measurement $i = 1, \ldots, n$ and of observable $j = 1, \ldots, obs$, whereas n represents the total amount of data and obs is the number of observable. Moreover, the data Y_{ij} satisfies the following observation equation

$$Y_{ij} = g_j(t_i, p) + \sigma_{ij}\epsilon_{ij} \qquad j = 1, \ldots, obs \; , \tag{5.2}$$

for some observation function $g : \mathbb{R}^d \to \mathbb{R}^{obs}$, $d \geq obs$, $\sigma_{ij} > 0$, and ϵ_{ij}'s are independent and standard Gaussian distributed random variables. The sample points t_i are ordered such that $t_0 \leq t_1 < \cdots < t_n \leq t_f$ and the observation function $g(\cdot)$ is again continuously differentiable in both variables. The generalization of Eq. (5.2) to more than one experiment, possibly under different experimental conditions, reads:

$$Y_{ijk} = g_j(x(t_{ij}), p) + \sigma_{ijk}\epsilon_{ijk} \qquad k = 1, \ldots, n_{exp} \; , \tag{5.3}$$

where n_{exp} is the number of experiments performed. Certain parameters may be different for each experiment, but the treatment of these local parameters and the different experiments requires only minor modifications of the described procedures and therefore only the one-experiment design $n_{exp} = 1$ is considered.

On the basis of the measurements Y_{ij} the task is now to estimate the initial state x_0 and the parameters p. The principle of maximum-likelihood, see e.g. [94], yields an appropriate cost function which has to be minimized with respect to the parameters x_0 and p. Defining $x(t_i; x_0, p)$ as being the trajectory at time t_i, the cost function is then given by

$$\mathcal{L}(x_0, p) = \sum_{i=1}^{n} \sum_{j=1}^{obs} \frac{\left(Y_{ij} - g_j(x(t_i; x_0, p), p)\right)^2}{2\sigma_{ij}^2} \; . \tag{5.4}$$

A direct minimization of $\mathcal{L}$ with respect to x_0, p leads to the so called initial value approach.

Initial Value Approach

The development of the initial value approach has a long history, [89, 95-98]. Again, one can distinguish between local and global optimization methods. If global optimization procedures are used for minimizing the likelihood, Eq. (5.4), the computational cost is rather high. On the other hand local optimization algorithms are having a small domain in parameter space for which the method converges to the global minimum. These problems are due to the following difficulties:

1. The optimization problem is highly non-linear such that local optimization routines tend to converge to local minima.

2. The solution of the differential equation can become unstable such that the trajectory diverges before the last time point t_n is reached.

An efficient and robust method minimizing these effects therefore needs a modification of the optimization scheme. One possibility of such a modification is multiple shooting.

Multiple Shooting

A detailed mathematical analysis of the multiple shooting method was performed by Bock [91-93]. Some applications of the method to measured data are, e.g., [99-103]. The basic idea of multiple shooting is that the parameter space is enlarged during the optimization process. This offers the possibility to circumvent local minima because the procedure has more flexibility for searching the parameter space. It is realized by subdividing the time interval $I = [t_0, t_f]$ into $n_{ms} < n$ subintervals I_k such that each interval contains at least one measurement. Each of the intervals is assigned to an individual experiment having its own initial values $(x_0^k)_{k=1,\ldots,n_{ms}}$ but sharing the same parameters p. The only difference in the cost function Eq. (5.4) is that the trajectory $x(t_i; x_0, p)$ is replaced by the interval dependent trajectory $x(t_i; x_0^k, p)$ for all $k = 1, \ldots, n_{ms}$. Since the over-all trajectory for each $t \in I = I_1 \cup \cdots \cup I_{n_{ms}}$ is usually discontinuous at the joins of the subintervals, the fitted curve would not satisfy the smoothness assumption of the model, Eq. (5.1). To enforce smoothness of the final trajectory, the optimization is constrained such that all discontinuities are eventually removed which therefore leads to a constrained non-linear optimization problem. This has the advantage that further equality and inequality constraints, such as parameter bounds or conservation relations can easily be implemented.

For each $k = 1, \ldots, n_{ms}$ let $t_k^+ = \max\{I_k\}$, $t_k^- = \min\{I_k\}$ and $\theta_k = (x_0^k, p)$. The optimization problem can then be formulated in the following manner:

$$\mathcal{L}(\theta_1, \ldots, \theta_{n_{ms}}) = \tfrac{1}{2} \sum_{j=1}^{obs} \sum_{k=1}^{n_{ms}} \sum_{\{i:t_i \in I_k\}} \left(R_{ijk}^a(\theta_k) \right)^2 = \min_{\theta_1,\ldots,\theta_{n_{ms}}}$$

subject to

$$\begin{aligned} & x(t_i^+; \theta_i) - x(t_{i+1}^-; \theta_{i+1}) = 0 \qquad i = 1, \ldots, n_{ms} - 1 \\ & R_j^e(\theta_1, \ldots, \theta_{n_{ms}}) = 0 \qquad\qquad j = 1, \ldots, n_e \\ & R_k^g(\theta_1, \ldots, \theta_{n_{ms}}) \geq 0 \qquad\qquad k = 1, \ldots, n_g \ , \end{aligned} \tag{5.5}$$

where the continuity constraints are given at the first row of the constraints-part followed by some optional constraints R_j^e, R_k^g, to include, e.g., conservation laws or parameter bounds. The cost function $\mathcal{L}(\theta_1, \ldots, \theta_{n_{ms}})$ is equivalent to Eq. (5.4) if the continuity constraints are satisfied, hence

$$R_{ijk}^a(\theta_k) = \frac{Y_i^{(j)} - g^{(j)}(x(t_i; \theta_k), p)}{\sigma_{ij}} \ .$$

This non-linear programming type of problem can only be solved iteratively. We use the generalized-quasi-Newton method for solving Eq. (5.5), where the cost function is expanded up to the second order with respect to some initial guess $\theta^0 = (\theta_1^0, \ldots, \theta_{n_{ms}}^0)$. All contributions depending on the second derivative of R_{ijk}^a are neglected afterwards. This is possible because these contributions to the Hessian of $\mathcal{L}$ are vanishing asymptotically, $n \to \infty$, if the model assumptions are correct [93, 14]. From the quadratic approximation an update step for the l-th iteration $\Delta\theta^l = (\Delta\theta_1^l, \ldots, \Delta\theta_{n_{ms}}^l)$ can be calculated by solving the linear programming problem

$$
\begin{aligned}
&\tfrac{1}{2}\sum_{j=1}^{obs}\sum_{k=1}^{n_{ms}}\sum_{\{i:t_i\in I_k\}}\left(R_{ijk}^a(\theta_k^l) + d_\theta R_{ijk}^a(\theta_k^l)\Delta\theta^l\right)^2 = \min_{\Delta\theta^l} \\
&\text{subject to} \\
&x(t_i^+;\theta_i^l) - x(t_{i+1}^-;\theta_{i+1}^l) + d_{\theta_i}x(t_i^+;\theta_i^l)\Delta\theta_i^l - d_{\theta_{i+1}}x(t_{i+1}^-;\theta_{i+1}^l)\Delta\theta_{i+1}^l = 0 \qquad (5.6)\\
&R_j^e(\theta^l) + d_\theta R_j^e(\theta^l)\ \Delta\theta^l = 0 \\
&R_k^g(\theta^l) + d_\theta R_k^g(\theta^l)\ \Delta\theta^l \geq 0\ ,
\end{aligned}
$$

where d_θ denotes the derivative with respect to the parameters θ of the corresponding function. Setting $\theta^{l+1} = \theta^l + \Delta\theta^l$, $l = 1, \ldots$ and iterating Eq. (5.6) until $\Delta\theta^l \approx 0$, yields a minimum of Eqs. (5.5) under the condition that all parameters are identifiable and the constraints are not contradictory. These extra assumptions are necessary to fulfil the so called Kuhn-Tucker conditions for the solvability of constrained, non-linear optimization problems [104, 93]. In Sec. 5.4 a regularization approach is discussed for weakening these restrictions if non-identifiable parameters are present.

In combination with multiple shooting the generalized-quasi-Newton approach has three major advantages:

1. The optimization is sub-quadratically convergent.
2. A transformation of Eqs. (5.6) can be found such that the transformed equations are numerically equivalent to the initial value approach, which is called *condensing*.
3. Due to the linearization of the continuity constraints, they do not have to be fulfilled exactly after each iteration, but only at convergence. This allows discontinuous trajectories during the optimization process, reducing the problem of local minima.

Properties 1. and 2. are yielding the desired speed of convergence whereas 3. is mainly responsible for the stability of multiple-shooting. This is gained by the possibility that the algorithm can circumvent local minima by allowing for discontinuous trajectories while searching the minimum. The main disadvantage results from the linearization of the cost function. It can easily happen that despite the update step $\Delta\theta^l$ is pointing in the direction of decreasing $\mathcal{L}$ the proposed step is too large. Such an overshooting is common to any simple optimization procedures based on the local approximation of the cost function. A suitable approach to cure this defect is to *damp* the proposed step, which is realized by relaxing the update scheme to $\theta^{l+1} = \theta^l + \lambda^l\Delta\theta^l$ for some $\lambda^l \in (0, 1]$. Both, the condensation algorithm and the damping method are necessary for building up a fast and stable parameter estimator

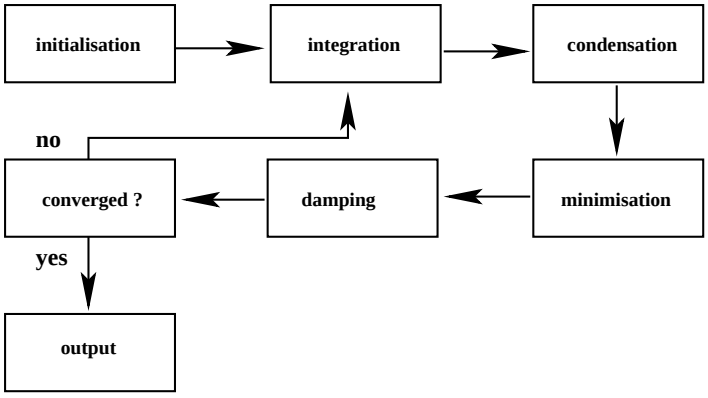

Figure 5.1: The main program flow is shown above. Here, all stages of the algorithm are displayed

for ODEs. These procedures as well as the main program flow are the subject of following section.

5.3. Detailed Description of Multiple Shooting

In the previous section the basic idea and some aspects of the performance of multiple shooting was displayed without emphasizing any algorithmic details of the method. To fill this gap, each module, starting from the initialization and ending in the output of the procedure is discussed in detail. The different stages of the described method can be extracted from the flow chart, Fig. 5.1. Beginning at the initialization, where e.g the multiple shooting mesh as well as the initial values of each interval are set, a first trial trajectory has to be integrated. Using these data, the linearized problem Eq. (5.6) can be formulated for the initial iteration and condensed in order to accelerate the minimization process. To prevent overshooting, the relaxation or damping of the obtained update step is done. Then one decides whether the procedure is converged or a further iteration has to be taken into account by integrating a new trail trajectory, applying a convergence criterion, such as $||\Delta\theta^l|| \approx 0$. After convergence, output such as the parameter estimates, the estimates for the initial values as well as the covariance matrix for a statistical analysis of the solution is provided. The first non-trivial stage in the program flow is the integration of a trial trajectory.

Integration

The choice of the numerical integrator depends on the class of ODE given in Eq. (5.1) or its numerical stability. There are four major groups to consider:

1. non-stiff ODEs

2. stiff problems
3. delay differential equations
4. and differential algebraic equations.

For non-stiff ODEs standard numerical integrators such as the Runge-Kutta method [14] with an appropriate step size control can be used. Whereas, if the solution of the ODE has at least two different time scales which differ by orders of magnitude only stiff integrators are useful. Especially in the case of multiple shooting we propose to use ODESSA [105, 106], because the code is optimized for simultaneously solving the sensitivity equations. The significance of the trajectory's sensitivity is due to the linearization given in Eq. (5.6) and will be discussed later. Delay differential equations (DDEs) cannot be represented by Eq. (5.1). Although DDEs are not ordinary differential equations, it is possible to adapt multiple shooting to this class of differential equations [107-109]. Since the right-hand-side of a DDE depends on the time delayed trajectory or a delay distribution, specially suited integrators are needed. A widely used DDE integrator is, e.g., RETARD [110], for a deeper discussion of DDEs we refer to [111]. Differential algebraic equations (DAEs) are differential equations in which algebraic relations between the state variables are present. In some cases the algebraic relations can be formulated as equality constants and are thus treated like constrained ODEs. Sometimes, this kind of separation is not possible such that special DAEs integrators have to be considered [112].

Besides the choice of the integrator, the solution of the sensitivity equations has to be obtained, because the Jacobian $d_\theta R^a_{ijk}(\theta^0_k)$ or $d_\theta x(t_i^+;\theta_i^0)$ in Eq. (5.6) contains derivatives of the trajectory with respect to the initial values and parameters:

$$\frac{\partial x(t;\theta_k)}{\partial x_0^{k(i)}} \quad \text{and} \quad \frac{\partial x(t;\theta_k)}{\partial p^{(j)}} \qquad t \in I_k,\ k = 1,\ldots,n_{ms},\ i = 1,\ldots,d,\ j = 1,\ldots,n_p\ .$$

In order to calculate these quantities numerically, three approaches are feasible:

1. finite differences, called external differentiation [92, 93],
2. differentiation of the integration scheme, called internal differentiation [92, 93, 110],
3. and the simultaneous solution of the sensitivity equations [107].

The approximation of the derivatives by finite differences such as

$$\frac{\partial x(t;\theta_k)}{\partial x_0^{k(i)}} \approx h^{-1}\left(x(t;\theta_k + e_{i,x_0}h) - x(t;\theta_k)\right)$$

for some $h \ll 1$ and e_{i,x_0} being the i-th unit vector with respect to the initial value, leads to numerical difficulties. Due to the numerical integration, the trajectory $x(t;\theta_k)$ is corrupted by numerical noise. Since an adaptive integration step size is used, the maximal noise strength can be predefined by some constant $eps \ll 1$. Consequently, h cannot be chosen arbitrarily

small without destabilizing the method. Arguments based on the expansion of $x(t;\theta_k)$ reveals that the optimal choice is

$$h = \mathcal{O}(\sqrt{eps}) \ , \tag{5.7}$$

see e.g. [113]. Unfortunately, the constant of proportionality in Eq. (5.7) depends on the second derivative and is therefore not known. Furthermore, a high integration accuracy is needed for achieving a suitable derivative. Thus, external differentiation should be avoided because of the unknown parameter h and the high computational cost.

Differentiating the integration scheme is considerably faster than external differentiation [92, 93] and the problem of adjusting a parameter does not occur. On the other hand, internal differentiation depends highly on the used integrator and has to be adapted whenever one decides to try another integration scheme.

A more flexible and quite efficient approach is the simultaneous integration of the sensitivity equations. Consider again a trajectory $x(t;x_0,p) = x(t;\theta)$ of Eq. (5.1) and the derivative d_θ, where the subscript indicates the variables to be differentiated. The time evolution of the sensitivities $S(t;\theta) = d_\theta x(t;\theta)$ is then given by the solution of

$$\begin{aligned} \frac{d}{dt}S(t;\theta) &= (d_\theta f)(x(t;\theta),t,p) + (d_x f)(x(t;\theta),t,p)\ S(t;\theta) \\ S_0 &= S(t_0;\theta) = \left(\mathbb{1}_{d\times d}, 0_{d\times n_p}\right) \ , \end{aligned} \tag{5.8}$$

where $\mathbb{1}_{d\times d}$ is the $d\times d$-unity matrix, $0_{d\times n_p}$ the $d\times n_p$-matrix of zeros, and f is the right hand side of the ODE as introduced in Eq. (5.1). Simultaneously integrating Eq. (5.1) and Eq. (5.8) yields the trajectory as well as the desired sensitivities. It is further sufficient to restrict the step size control to the main ODE, Eq. (5.1). Doing this, the speed and the accuracy is comparable to the internal differentiation. It is therefore a matter of taste using either the internal differentiation or the simultaneous solution of the sensitivity equations, Eq. (5.8).

The procedure requires the calculation of derivatives like $d_p f, d_x f$, etc. Calculating such derivatives by hand can be very time consuming and error-prone for big systems. Therefore automatic differentiation should be applied. One possibility is to generate the derivatives at runtime by using program packages like ADIFOR or ADOLC [114, 115]. Since the derivatives have to be recalculated for every function evaluation, this approach slows down the method significantly. The calculation of the Jacobians should therefore processed before the program is executed which can be realized by using symbolic computation software, e.g., GinNaC [116].

Condensation

All information is now available for setting up Eq. (5.6). Suppose that $h_i = x(t_i^+) - x(t_{i+1}^-)$, $\Delta\theta_i^l = (\Delta x_0^i, \Delta p)$ for all $i = 1,\ldots,n_{ms}-1$ and because of (5.8), $d_{x_0^{i+1}} x(t_{i+1}^-) = \mathbb{1}$, $d_p x(t_{i+1}^-) = 0$ then the continuity constraints can be written as

$$h_i + d_{x_0^i} x(t_i^+)\ \Delta x_0^i + d_p x(t_i^+)\ \Delta p = \Delta x_0^{i+1} \qquad i = 1,\ldots,n_{ms}-1 \ . \tag{5.9}$$

According to Eq. (5.9) all initial value update steps at the multiple shooting intervals can therefore be related to Δx_0^1 by backward elimination. Inserting the increments $\Delta x_0^2, \ldots, \Delta x_0^{n_{ms}}$ obtained by Eq. (5.9) into Eq. (5.6) yields a system to be solved only for Δx_0^1 and Δp. Let R^a be the $n \cdot n_{ms} \cdot n_{obs}$-dimensional vector with components R^a_{ijk} and R^e, R^g respectively, the condensed problem is thus

$$\begin{aligned} & ||u_1^a + E_1^a \ \Delta x_0^1 + P_1^a \ \Delta p||^2 = \min_{\Delta x_0^1, \Delta p} \\ \text{subject to} \quad & \\ & u_1^e + E_1^e \ \Delta x_0^1 + P_1^e \ \Delta p = 0 \\ & u_1^g + E_1^g \ \Delta x_0^1 + P_1^g \ \Delta p \geq 0 \ , \end{aligned} \tag{5.10}$$

where $u_1^{a/e/g}$ and the matrices $E_1^{a/e/g}, P_1^{a/e/g}$ are determined by the recursion [92, 93]:

$$\begin{aligned} \text{Initialisation} \quad : \quad & u_{n_{ms}}^{a/e/g} = R^{a/e/g} \ , \ E_{n_{ms}}^{a/e/g} = d_{x_0^{n_{ms}}} R^{a/e/g} \ , \ P_{n_{ms}}^{a/e/g} = d_p R^{a/e/g} \\ \text{For } i = n_{ms}, \ldots, 2 \quad : \quad & u_{i-1}^{a/e/g} = u_i^{a/e/g} + E_i^{a/e/g} \ h_{i-1} \\ & E_{i-1}^{a/e/g} = d_{x_0^{i-1}} R^{a/e/g} + E_i^{a/e/g} \ d_{x_0^{i-1}} h_{i-1} \\ & P_{i-1}^{a/e/g} = P_i^{a/e/g} + E_i^{a/e/g} \ d_p h_{i-1} \ . \end{aligned} \tag{5.11}$$

The condensation algorithm eliminates Eq. (5.9) such that problem Eq. (5.10) is of lower dimension than the original, Eq. (5.6). Since Eq. (5.11) involves only matrix multiplications the desired increase in speed is achieved by solving only the condensed problem. After the solution of Eq. (5.10) is determined, the actual full update step $\Delta\theta^l$ is obtained by the recursion given in Eq. (5.9), which involves again only matrix multiplications.

Minimization

The solution of the linear programming problem Eq. (5.10) can be obtained by calculating the generalized inverse $G(\theta^l)$ at θ^l. Since the condensation procedure removes the continuity constraints by partially calculating the generalized inverse using the transformation given above, we concentrate on the uncondensed problem Eq. (5.6) in the following. The general inverse then solves

$$-d_\theta R^a(\theta^l)\Delta\theta^l = R^a(\theta^l) \tag{5.12}$$

subject to all equality and inequality constraints of Eq. (5.6), where R^a is again the $n \cdot n_{ms} \cdot n_{obs}$-dimensional vector of the actual residuals. Therefore, $\Delta\theta^l = G(\theta^l)R^a(\theta^l)$ and by multiplying the system to solve, Eq. (5.12), with $G(\theta^l)$, we obtain $-G(\theta^l)d_\theta R^a(\theta^l) = \mathbb{1}$. Note that since Eq. (5.12) is over-determined the solution as constructed above only yields the minimum quadratic norm solution, as desired. Moreover, the equality and violated inequality constraints are handled by projections onto the resulting sub-manifold using Lagrange multipliers.

In practice, any appropriate minimization algorithm for solving constrained linear optimization problems, e.g., the routine E04NCF from the NAG library, LSEI [117] or, the method of Stoer [118], can be used.

Damping

Damping or relaxation of the update is essential for the stability of the whole method. To judge if the proposed update step is descendant, some kind of level function has to be chosen. Such a *level function* must share the same monotony properties of the cost function close to the global minimum. In case of unconstrained problems, it is feasible to use the cost function $\mathcal{L}$ directly, whereas some modifications are necessary for constrained problems, such as multiple shooting. These modifications are due to the constraints entering the level function via Lagrange multipliers. A possible level function is then

$$T(\theta) = \mathcal{L}(\theta) + \underbrace{\sum_{i=1}^{n_{ms}+n_e-1} \alpha_i \, |R_i^e(\theta)|}_{\text{equality constr.}} + \underbrace{\sum_{i=1}^{n_g} \beta_i \, |\min\{0, R_i^g(\theta)\}|}_{\text{inequality constr.}} , \tag{5.13}$$

where α_i and β_i are bounded below by their corresponding Lagrange multipliers. Based on this level function, a downhill procedure can always be constructed by some one-dimensional line-search algorithm. According to [91-93] it turns out that the performance of using $T(\theta)$ is rather bad. This inefficiency is due to

1. line-search has a high computational cost since a new trajectory has to be integrated for each evaluation of Eq. (5.13) and

2. the local geometry of the minimization problem is not adapted to the level function, leading to extremely small steps for badly conditioned problems.

To surmount these problems Bock [91-93] proposed to replace the line-search by some *predictor-corrector* method and the level function is changed to include the local geometry. As prototype for constructing such a level function, we consider the following ideal level function

$$T_{N,\theta^*}(\theta) = ||G(\theta^*)R^a(\theta)||^2 , \tag{5.14}$$

where θ^* is the minimum of the cost function $\mathcal{L}$, G is the generalized inverse as defined further above and R^a the vector of residuals at the corresponding point in parameter space. Expanding $R^a(\theta)$ about θ^* up to first order and substituting the obtained expression into Eq. (5.14) yields $T_{N,\theta^*}(\theta) = ||G(\theta^*)(R^a(\theta^*) + d_\theta R^a(\theta^*)(\theta - \theta^*) + O(||\theta - \theta^*||^2))||^2$. Since we assume that the Kuhn-Tucker conditions are fulfilled, as described in Sec. 5.2, $G(\theta^*)R^a(\theta^*) = 0$ and by the properties of the generalized inverse $-G(\theta^l)d_\theta R^a(\theta^l) = \mathbb{1}$, we obtain

$$T_{N,\theta^*}(\theta) = ||\theta - \theta^*||^2 + O(||\theta - \theta^*||^3) .$$

In conclusion, the ideal level function T_{N,θ^*} measures the squared Euclidean distance to the optimum up to third order. Therefore, T_{N,θ^*} is in vicinity of θ^* a distance measure in a Euclidean space which does not depend on application specific geometric properties of the parameter "landscape". Moreover, it shares the same monotony properties of the cost function close to the global minimum, as desired. Unfortunately, the knowledge of the

minimum θ^* is needed for constructing T_{N,θ^*}. In order to obtain an applicable level function which has similar properties as T_{N,θ^*}, we replace θ^* by θ^l. The resulting level function

$$T_N^l(\theta) = ||G(\theta^l)R^a(\theta)||^2 \tag{5.15}$$

is called *natural level* function which provides an efficient criterion for determining the relaxation coefficient λ^l for the l-th iteration.

Again, finding an appropriate λ^l for which the minimization scheme is descendant involves some kind of line-search to guarantee that $T_N(\theta^l + \lambda^l\Delta\theta^l) < T_N(\theta^l)$ is satisfied. Since the evaluation of the natural level function involves the integration of the trajectory and in addition the solution of the whole minimization procedure, calculating T_N is quite expensive. To prevent line-search, an upper bound for the level function evaluated at the relaxed update step $T_N(\theta^l + \lambda^l\Delta\theta^l)$ can be derived, as shown in [93] and in the following. Provided that the second derivative $d_\theta^2 R^a$ for the vector of residuals R^a exists in a sufficiently large domain containing θ^l, the following estimate holds:

$$T_N^l(\theta^l + \lambda^l\Delta\theta^l) \leq \left(1 - \lambda^l + \frac{\lambda^{l^2}}{2}\,\omega(\theta^l, \lambda^l)\right)^2 T_N^l(\theta^l)\,, \tag{5.16}$$

where for each $\lambda^l \in (0, 1]$ the function ω is given by

$$\omega(\theta^l, \lambda^l) = \sup_{s\in(0,\lambda^l]} \left\{ \frac{||G(\theta^l)\left(d_\theta R^a(\theta^l + s\Delta\theta^l) - d_\theta R^a(\theta^l)\right)\Delta\theta^l||}{s||\Delta\theta^l||^2} \right\} < \infty\,. \tag{5.17}$$

Therefore, on the basis of T_N^l a descendent step can always be found, if λ^l is correctly adjusted. In order show Eq. (5.16), consider the following estimates for $\alpha = \sqrt{T_N^l(\theta^l + \lambda^l\Delta^l)} - (1 - \lambda^l)\sqrt{T_N^l(\theta^l)}$:

$$\begin{aligned}
\alpha &\leq \left| \sqrt{T_N^l(\theta^l + \lambda^l\Delta^l)} - (1 - \lambda^l)\sqrt{T_N^l(\theta^l)} \right| \\
&\leq \left|\left| G(\theta^l)R^a(\theta^l + \lambda^l\Delta\theta^l) - (1 - \lambda^l)G(\theta^l)R^a(\theta^l) \right|\right|\,.
\end{aligned} \tag{5.18}$$

Since, $G(\theta^l)R^a(\theta^l) = \Delta\theta^l$, and inserting $-G(\theta^l)d_\theta R^a(\theta^l) = \mathbb{1}$ into Eq. (5.18), we arrive at

$$\begin{aligned}
\alpha &\leq \left|\left| G(\theta^l)\left[R^a(\theta^l + \lambda^l\Delta\theta^l) - R^a(\theta^l) - \lambda^l d_\theta R^a(\theta^l)\Delta\theta^l\right] \right|\right| \\
&= \left|\left| \int_0^{\lambda^l} \frac{G(\theta^l)\left\{d_\theta R^a(\theta^l + s\Delta\theta^l) - d_\theta R^a(\theta^l)\right\}\Delta\theta^l}{s||\Delta\theta^l||^2}\; s\;||\Delta\theta^l||\;\sqrt{T_N^l(\theta^l)}\; ds \right|\right| \\
&\leq \frac{\lambda^{l^2}}{2}\;\omega(\theta^l, \lambda^l)\;||\Delta\theta^l||\;\sqrt{T_N^l(\theta^l)}\,,
\end{aligned}$$

which proves Eq. (5.16).

Now, for some arbitrarily chosen $\eta \in (0,2]$, every $\lambda^l \in (0,\lambda^*]$ yields a descending step $T_N(\theta^l + \lambda^l \Delta\theta^l) < T_N(\theta^l)$, where λ^* can be obtained from the solution of

$$\lambda^* = \min\left\{1, \frac{\eta}{\omega(\theta^l,\lambda^*)\ ||\Delta\theta^l||}\right\}\ . \tag{5.19}$$

This is because $\lambda^l \leq \lambda^* \leq \eta\ (\omega(\theta^l,\lambda^*)||\Delta\theta^l||)^{-1}$ and by using Eq. (5.16)

$$\begin{aligned} T_N^l(\theta^l + \lambda^l\Delta\theta^l) &\leq \left(1 - \lambda^l + \frac{\lambda^l}{2}\ \eta\right)^2 T_N^l(\theta^l) \\ &= \left(1 - \lambda^l\,(1-\eta/2)\right)^2 T_N^l(\theta^l) < T_N^l(\theta^l)\ . \end{aligned}$$

For a given $\eta \in (0,2]$ the maximal relaxation parameter leading to a descendant step is therefore λ^*. Moreover, if the relaxation coefficient is chosen to be $\lambda^l \in [\lambda^*(\eta_1), \lambda^*(\eta_2)]$, for $0 < \eta_1 \leq \eta_2 < 2$, the damped generalized-quasi-Newton method converges to a full-step procedure, $\lambda = 1$, when the parameters are approaching the minimum. This requires the local identifiability of all parameters and the boundedness of the second derivative $d_\theta^2 R^a$ in the vicinity of the minimum. To show this property of the damping algorithm suppose that for all initial guesses $\theta_0 \in D$, where D is a convex set, the undamped generalized quasi-Newton converges locally to a θ^* which minimizes $\mathcal{L}$. Moreover, let the norm of the second derivative $d_\theta^2 R^a$ be bounded by $\tilde{\omega}$ on D. Then, for all $s \in [0,1]$

$$\begin{aligned} \left|\left|G(\theta^l)\left(d_\theta R^a(\theta^l + s\Delta\theta^l) - d_\theta R^a(\theta)\right)\Delta\theta^l\right|\right| &= \left|\left|G(\theta^l)\int_0^s d_\theta^2 R^a(\theta^l + t\Delta\theta^l)(\Delta\theta^l, \Delta\theta^l)\ dt\right|\right| \\ &\leq ||G(\theta^l)||\ \sup_{x\in D}\left|\left|d_\theta^2 R^a(x)\right|\right|\ s\ ||\Delta\theta^l||^2 \\ &\leq \tilde{\omega}\ s\ ||\Delta\theta^l||^2\ , \end{aligned}$$

by the continuity of G on D. According to Eq. (5.17), $\omega(\theta^l,\lambda^l) \leq \tilde{\omega} < \infty$ and therefore $\omega(\theta^l,\lambda^l)\ ||\Delta\theta^l|| \leq \tilde{\omega}\ ||\Delta\theta^l|| \to 0$ for $l \to \infty$. Due to Eq. (5.19), the maximal possible damping parameter leading to descending quasi-Newton steps converges to one.

Since $\omega(\theta^l,\lambda^l)$ is a priori not known a suitable estimation or approximation is necessary. Demanding the coincidence of the estimator with Eq. (5.17) in the limit $\lambda^l \to 0$ automatically guarantees an appropriate relaxation scheme whenever a massive damping is needed. The estimator

$$\hat{\omega}(\theta^l,\lambda^l) = 2\ \frac{||G(\theta^l)R(\theta^l + \lambda^l\Delta\theta) - (1-\lambda^l)\Delta\theta^l||}{||\lambda^l\Delta\theta^l||^2}\ , \tag{5.20}$$

satisfies this desired property [93]. Replacing ω with $\hat{\omega}$ in Eq. (5.19), a predictor-corrector procedure can be constructed to find a suitable $0 < \lambda^l \leq \lambda^*$. Assuming that $\hat{\omega}(\theta^{l-1},\lambda^{l-1})$ from the previous Gauss-Newton iteration is approximately constant the damping parameter for the actual iteration can be determined by

$$\lambda^l = \min\left\{1, \frac{\eta_0}{\hat{\omega}(\theta^{l-1},\lambda^{l-1})\ ||\Delta\theta^l||}\right\}\ , \tag{5.21}$$

for some $0 < \eta_0 < 2$. If the assumption is violated such that decreasing of the method cannot be guaranteed, $\hat{\omega}$ has to be recalculated from Eq. (5.20) but now using λ^l, given in Eq. (5.21). This procedure has to be repeated until a suitable relaxation coefficient has been obtained. For some $0 < \eta_0 < \eta_2 < 2$, $\tau \in [0.5, 1]$ and $0 < \tau_{min} \ll 1$, the damping procedure can be described by the following algorithm:

1. Set $j = 0$ and calculate the predictor $\mu_0 = \eta_0 / \left(\hat{\omega}(\theta^{l-1}, G, \lambda^{l-1}) \; ||\Delta\theta^l||\right)$.
2. The predicted relaxation step is then given by
$$\lambda_j^{pred} = \begin{cases} 1 & \tau < \mu_j \\ \mu_j & \tau_{min} \leq \mu_j \leq \tau \\ \tau_{min} & \mu_j < \tau_{min} \end{cases} .$$
3. If $\hat{\omega}(\theta^l, \lambda_j^{pred}) \; ||\Delta\theta^l|| \lambda_j^{pred} \leq \eta_2$ then the proposed step $\lambda_j^{pred} = \lambda^l$ yields a descending update and is therefore accepted. Whereas, if the above statement is violated, $j = j+1$ and
4. the prediction λ_{j-1}^{pred} is corrected by
$$\mu_j = \frac{\eta_0}{\hat{\omega}(\theta^l, \lambda_{j-1}^{pred}) \; ||\Delta\theta^l||} . \tag{5.22}$$
5. Step 2, 3 and 4 are repeated until a sufficient relaxation coefficient λ^l is found or the minimal step length τ_{min} is reached.

In order to ensure the numerical stability of the damping algorithm, a predefined minimal relaxation τ_{min} must be provided. An upper threshold τ is also given, which determines the transition from a damped procedure to a full step approach, $\lambda^l = 1$. Finally, η_0, η_2 are controlling the correction (step 4). Inserting $\hat{\omega}(\theta^l, \lambda_{j-1}^{pred}) \; ||\Delta\theta^l|| \lambda_{j-1}^{pred} > \eta_2$ into Eq. (5.22) and suppose that $\mu_j > \tau_{min}$, we have $\lambda_j^{pred} < (\eta_0/\eta_2) \; \lambda_{j-1}^{pred}$. Thus, the minimal correction factor is given by the ratio η_0/η_2. A suitable choice of these control parameters is, e.g., $\tau_{min} = 0.01, \tau = 0.5, \eta_0 = 1$ and $\eta_2 = 1.8$. Since there is no information about $\hat{\omega}$ for the first Gauss-Newton iteration, one can chose $\hat{\omega}$ such that λ^1 attains the lower bound τ_{min}.

The described damping algorithm reflects the advantageous geometrical properties of the natural level function. Furthermore, the correction step Eq. (5.22) is rarely activated such that in most of the cases only one extra integration is needed to achieve an appropriate damping. Unfortunately, there are no rigorous proofs that this damping strategy always yields a descending method, which is due to the approximation of ω. But the algorithm provides excellent results in practice, we can therefore highly encourage the use of this damping scheme.

Statistical Analysis

Beside the pure estimation of parameters and initial values statistical information such as standard errors or confidence intervals for these values are essential in practice. In the case

of maximum likelihood estimators the statistical properties can be derived in the asymptotic limit. Under mild conditions, the estimator is converging to the "true" parameters and the parameters are normally distributed [119]. The covariance matrix of the estimates can be obtained from the Fisher information matrix which can be approximated by

$$\mathrm{IF}(\hat{\theta})_{ij} = \frac{\partial^2 \mathcal{L}(\hat{\theta})}{\partial\theta_i \partial\theta_j} \,, \tag{5.23}$$

where $\mathcal{L}$ is the negative logarithm of the likelihood. Inverting $\mathrm{IF}(\hat{\theta})$ then yields the covariance matrix C for the estimated parameters $\hat{\theta}$.

The described procedure for estimating parameters in ODEs is a maximum likelihood approach, such that Eq. (5.23) provides a sufficient approximation of C^{-1}. Most of the minimizers, e.g. [117], simultaneously calculate this covariance matrix within the quadratic approximation discussed in Sec. 5.2.

All described stages, integration, condensation, etc. define the basic algorithm of multiple shooting which are valid in case of identifiable problems. As explained, the restriction of having only identifiable parameters is of great importance for the convergence of the algorithm, the damping strategy and the statistical analysis. To judge if the system of interest contains only identifiable parameters several methods can be applied, e.g [120-123]. Since these methods can involve extremely tedious calculations even for small models, it is often a priori not feasible to decide whether the system is identifiable. Alternatively, the multiple shooting method can be modified to obtain parameter estimates even if some parameters can not be identified. A possible implementation of such a strategy is described in the next section.

5.4. Regularization in Case of Non-Identifiable Parameters

If some parameters are not identifiable in a certain domain of the parameter space, the matrix P_1^a of the condensed system Eq. (5.10) does not have its full rank whenever the algorithm tries to enter this region. The central idea of the regularization approach is to manipulate the estimation process such that the modified matrix $\tilde{P}_1^a$ attains its full rank. The manipulation we propose can be regarded as heavily damp a specific parameter set such that they appear to be fixed.

A singular value decomposition [14] of $P_1^a = U\ \mathrm{diag}(w_1, \ldots, w_{n_p})\ V^T$ is calculated first to determine if P_1^a has its full rank. Both matrices U, V^T are orthogonal, V^T is the transposed matrix of V, and $\mathrm{diag}(w_1, \ldots, w_{n_p})$ is a diagonal matrix containing the positive (by convention) singular values $w_1, \ldots, w_{n_p}$. It this further assumed that the singular values are in descending order $w_1 \geq \cdots \geq w_{n_p}$. The rank criterion is said to be violated if the condition number w_{n_p}/w_1 is below a given threshold $0 < \epsilon_c \ll 1$. Introducing a threshold is necessary because the numerical error prevents the condition number to vanish exactly. Therefore, the value of ϵ_c should be close to the machine accuracy. In order to judge, which parameters contribute to the violation of the rank criterion, the set $M_c = \{i \ : \ w_{n_p}/w_i \leq \epsilon_c\}$ of all

singular directions is regarded. Let

$$\Pi_c = \sum_{i \in M_c} e_i \otimes e_i^T$$

be the projection onto the space of all singular directions, the regularization can be realized by enlarging the corresponding singular values. For this reason, some $\Delta \gg w_1$ has to be chosen. The regularized matrix $\tilde{P}_1^a$ is the given by

$$\tilde{P}_1^a = U \ \left(\mathrm{diag}(w_1, \ldots, w_{n_p}) + \Delta \ \Pi_c\right) \ V^T \ . \tag{5.24}$$

For a well adjusted value of Δ all parameters contributing to the singular directions are almost kept fixed if P_1^a is replaced by $\tilde{P}_1^a$ in Eq. (5.10). Since the described regularization method is similar to the classical damping procedure of Levenberg and Marquardt [124, 125], regularization can also be regarded as an individual damping of ill-conditioned directions. If the regularization is turned off at the last iteration, the singular directions of the covariance matrix can help to find the unidentifiable parameters. Note that if some initial values are not identifiable, the same procedure can also be applied to the matrix E_1^a in Eq. (5.10).

5.5. Simulation Study

To display the performance of multiple shooting a simulation study is carried out in the following. To that end, a trajectory from a model describing oscillations in a calcium signalling pathway is chosen. Calcium ions are an important second messager substance in eucaryotic cells. Thereby, Ca^{2+} is a substantial part of the cellular information processing system. It has been observed that the concentration of the cytoplasmatic calcium ions may exhibit oscillations, see e.g. [126]. A mathematical model of these oscillations is developed in [127] which shows for a specific set of parameters complex and even chaotic behavior. The main stages of the calcium signalling pathway are activation of the phospolipase C (PLC) enzyme by the activated G_α unit of a G-protein linked receptor. This enzyme is attached to the plasma membrane and itself catalyzes the hydrolysis of the membrane lipid phosphatidyl inositol-4,5-bisphosphate to build inositol-1,4,5-trisphosphate (IP_3) and diacylglycerol. Then, IP_3 may bind to specific ion-channels in the endoplasmatic reticulum which lead to a massive out-flux of Ca^{2+} from intra-cellular stores.

For the following simulation study we used the most complex mathematical model presented in [127]. This model consists of four state variables representing the concentrations of: 1) the active G_α unit, G_α^*, 2) the active PLC, PLC^*, 3) the free calcium in the cytoplasm, Ca_{cyt}, and 4) the calcium in the endoplasmatic reticulum, Ca_{er}. For sake of simplicity, the dynamics of the IP_3 is assumed to follow the dynamics of the active PLC. The dynamics of the remaining state variables is then given by the following differential equation:

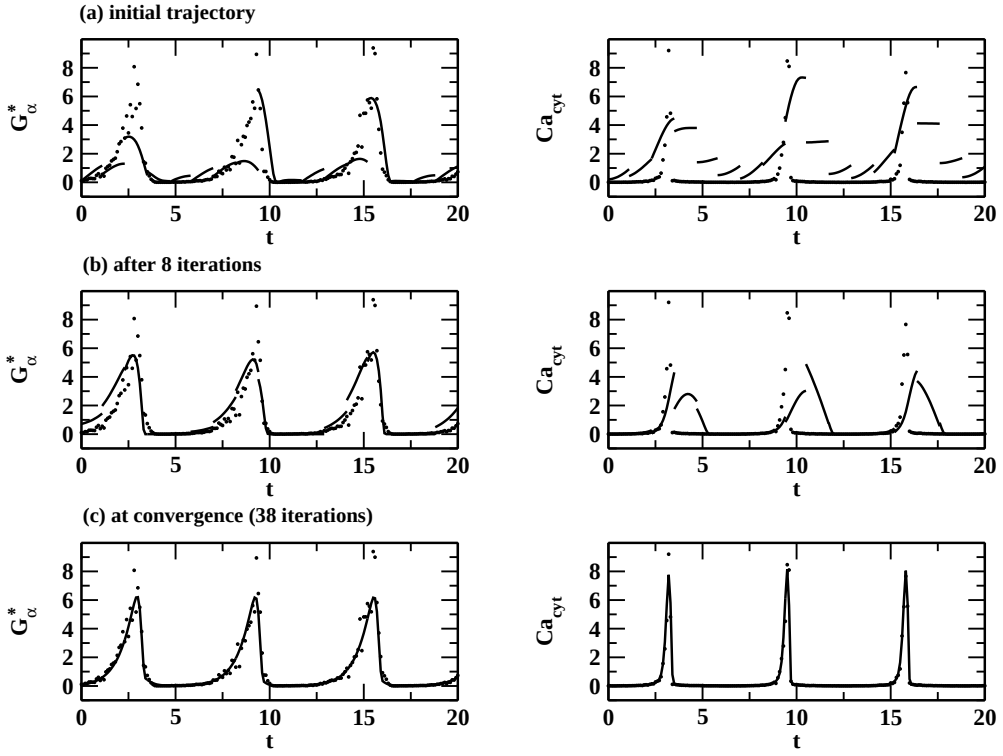

Figure 5.2: Identification of the presented calcium signalling pathway using multiple shooting. For sake of clearness, three snapshots of the identification procedure are shown only for the state variables G^*_α, and Ca_{cyt}. Due to the large amount of multiple shooting intervals the initial trajectory is highly discontinuous (a). After 8 iterations the trajectory is significantly smoother (b). Since the discontinuities are removed by the algorithm, the trajectory turns out to be continuous at convergence (c).

$$
\begin{aligned}
\frac{d}{dt}\ G^*_\alpha \quad &= k_1 + k_2\ G^*_\alpha - k_3\ PLC^*\ \frac{G^*_\alpha}{G^*_\alpha + Km_1} - k_4\ Ca_{cyt}\ \frac{G^*_\alpha}{G^*_\alpha + Km_2} \\
\frac{d}{dt}\ PLC^* &= k_5\ G^*_\alpha - k_6\ \frac{PLC^*}{PLC^* + Km_3} \\
\frac{d}{dt}\ Ca_{cyt}\ &= k_7\ PLC^*\ Ca_{cyt}\ \frac{Ca_{er}}{Ca_{er} + Km_4} + k_8\ PLC^* + k_9\ G^*_\alpha \\
&\qquad - k_{10}\ \frac{Ca_{cyt}}{Ca_{cyt} + Km_5} - k_{11}\ \frac{Ca_{cyt}}{Ca_{cyt} + Km_6} \\
\frac{d}{dt}\ Ca_{er}\ &= -k_7\ PLC^*\ Ca_{cyt}\ \frac{Ca_{er}}{Ca_{er} + Km_4} + k_{11}\ \frac{Ca_{cyt}}{Ca_{cyt} + Km_6}\ ,
\end{aligned}
\tag{5.25}
$$

where the 17 parameters are chosen in the following manner: $k_1 = 0.09$, $k_2 = 2$, $k_3 = 1.27$, $k_4 = 3.73$, $k_5 = 1.27$, $k_6 = 32.24$, $k_7 = 2$, $k_8 = 0.05$, $k_9 = 13.58$, $k_{10} = 153$, $k_{11} = 4.85$, $Km_1 = 0.19$, $Km_2 = 0.73$, $Km_3 = 29.09$, $Km_4 = 2.67$, $Km_5 = 0.16$, and $Km_6 = 0.05$. For this specific parameterization the solution of Eq. (5.25) shows a limit cycle. As initial values we use $G^*_\alpha(0) = 0.12$, $PLC^*(0) = 0.31$, $Ca_{cyt}(0) = 0.0058$, and $Ca_{er}(0) = 4.3$. As sampling

	single shooting	**multiple shooting**
convergent fits	**4%**	**49%**
needed computational load	**(44 ± 16) s**	**(48 ± 58) s**

Table 5.1: A comparison of multiple and single shooting (initial value approach) in terms of stability, convergence to the global optimum and computational load. The results are obtained from 250 runs using a randomly generated initial guess for each sample. For sake of comparability the same initial guess is used for single and multiple shooting within the sample. For the simulations a computer with a 2.6 GHz Pentium 4 processor is used.

time domain we choose the interval $[0, 20]$ and the sampling interval is set to $\Delta t = 0.1$. This leads to 200 data points. We chose a biological reasonable noise model where the standard deviation of each observed variable is proportional to the concentration of its noise free state. This leads to an overall mean noise-to-signal ratio of 6.5%.

For comparing multiple shooting with single shooting we aim to estimate the parameters $k_1, \cdots, k_{11}$. The initial guesses of these parameters are randomly selected from an uniform distribution over $[0, 1]$. Note, that some of the true parameters , e.g., k_5, k_6, and k_{10} are far of this interval of initial guesses for the parameters, rendering the estimate a difficult one. A snapshot of the initial trajectory, after the 8. multiple shooting iteration and the final trajectory is shown in Fig. 5.2. Here, 17 multiple shooting intervals are used, leading to a rather rough initial trajectory, Fig. 5.2a. These discontinuities are still present after eight iterations, Fig. 5.2b and are completely removed at convergence, Fig. 5.2c. To compare the performance of multiple shooting to the initial value approach, a simulation study has been carried out. To achieve the most comparable results, a sample of 250 initial guesses are randomly selected. The performance for both, multiple shooting and the initial value approach is compared in terms of stability and computational load using the same initial guess for each sample. The results are summarized in Tab. 5.1. These results clearly supports the statements about the superior stability of multiple shooting, since only 4% of fits converged to the global optimum for the initial value approach whereas 49% for multiple shooting. If one compares the ratio of these values, it turns out that about twelve times as many convergent fits converged to the global optimum for multiple shooting than for the initial value approach. In terms of computational load, both methods are showing basically the same performance. Therefore, for this particular problem, the condensation algorithm is highly efficient since the condensed problem is computationally equivalent to the initial value problem as discussed in Sec. 5.3. In addition, the high standard deviation of the computational load for both methods indicates that the needed computational effort to find an optimum of the cost function highly depends on the used initial guess.

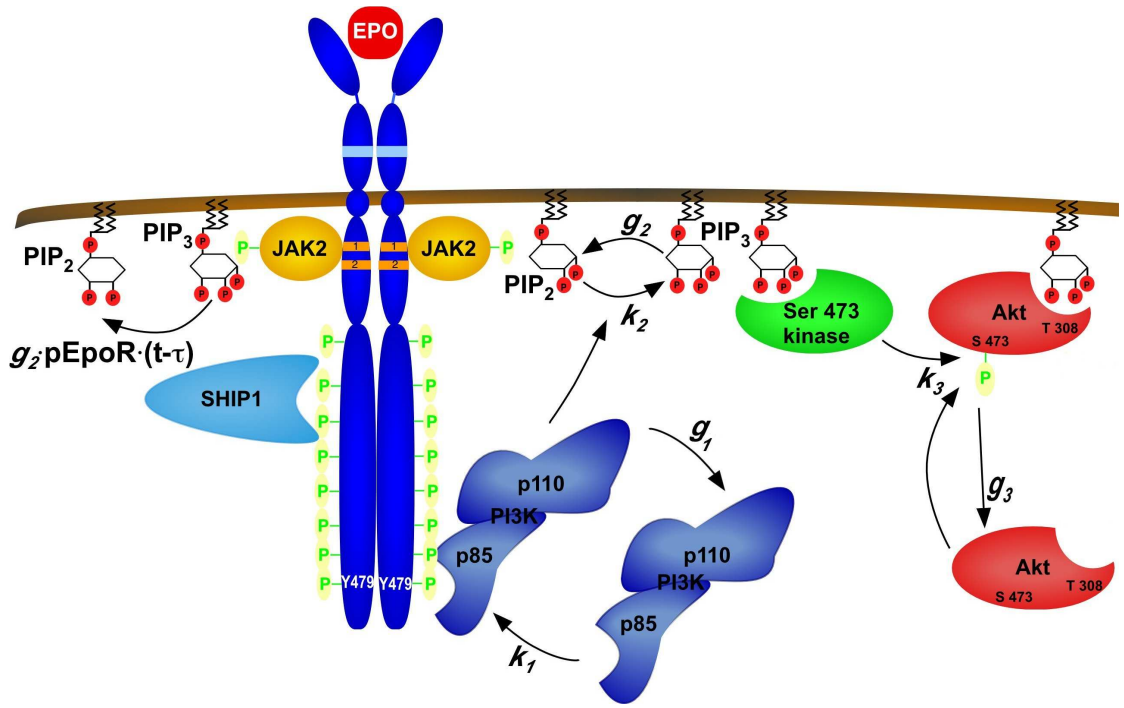

Figure 5.3: The core module of the PI3-Kinase Akt signaling pathway. Binding of the p85/p110 heterodimer to the phosphorylated tyrosine 479 of the Epo-receptor (EpoR) activates the kinase activity of PI3K. For this reaction the assumed binding rate is k_1 and the degradation of the EpoR-PI3K complex is assumed to happen at a rate g_1. Then, the conversion of inositol-4,5-bisphosphates (PIP_2) to inositol-3,4,5-trisphosphates (PIP_3) located in the plasma membrane takes place with rate k_2. PIP_3 provides docking sites for Akt and its upstream kinases, thereby placing the them in close proximity and enabling the phosphorylation and activation of Akt with rate k_3. PIP_3 is removed by inositol phosphatases with rate g_2, Akt is unactivated by cytosolic protein phosphatases with rate g_3.

5.6. Application to Biochemical Data

As an application of the described method to measured data, the phosphoinositide 3-kinase (PI3K) signal transduction pathway is chosen. Before discussing this pathway in detail, a few biochemical concepts are introduced. Phosphorylation is a process which alters the state of a protein. This is triggered by a type of enzyme, called kinase, which transfers phosphate groups (PO_4) to the target protein. A phosphorylated protein can be regarded as being active in a sense that it may alter the state of other proteins downstream the signalling pathway. In order to remove the phosphate groups from an activated protein, a further enzyme is consulted, the phosphatase. The phosphatase therefore turns the protein from the activated state to the unactivated state.

The PI3K pathway is activated by a large number of cell surface receptors and plays an important rôle in tumor-genesis [128, 129]. However, if the PI3K is activated by the hematopoietic cytokine receptor EpoR, its function is important for the proliferation (cell devision) and differentiation of blood progenitor cells. Ligand binding leads to the activa-

tion of the Epo-receptor by phosphorylation, namely attaching phosphate to specific sites of the receptor. This allows the binding of the PI3K p85/p110 heterodimer and thereby activates the PI3 kinase. Activated PI3 kinase proteins then generate 3,4,5 phosphorylated phosphatidylinositols (PIP_3) out of 4,5 phosphorylated phosphatidylinositols (PIP_2), both are attached to the plasma membrane of the cell. PIP_3 provides a specific docking site, such that other compatible proteins can be activated. Especially, the serine/theonine kinase Akt and its upstream kinases can bind to this site which leads to the activation of Akt to relay the signal further downwards which alters the cell's metabolism, transcriptional activity, etc. A sketch of the PI3K signalling pathway is shown in Fig. 5.3. More detailed information about the PI3K pathway is, e.g., presented in [130, 131].

The presented data were obtained using cultivated BaF3 cells, where no Epo stimuli have been applied for a time period of five hours prior the time course experiments. This is necessary to study the reaction of the pathway when a stimulus is applied, since the entire pathway is "switched off" before starting the experiments. At 20 distinct time points after the stimulus, spanning one hour in total, about 10^7 cells are removed from the population. To terminate each cellular reaction a lysis buffer was applied to these cells, thereby providing a snapshot of the cell's state at each instant of time. Then, up to an unknown scaling factor the concentration of the activated PI3K, the activated Akt, and the state of the Epo-receptor is measured using quantitative imunoblotting, a method which is based on electrophoresis. Unfortunately, the other components of the PI3K pathway cannot be measured using these experiments. Since the pathway depicted by Fig. 5.3 contains no feed-back loop, the modelling procedure can be divided into two steps. The first step consists on the modelling of the activated PI3K by the receptor and the second step leads from the activated PI3K to the phosphorylation of Akt.

Focussing on first step of the pathway, where the time course of receptor activity is denoted by $EpoR(t)$, and the concentration of the active PI3 kinase by $aPI3K(t)$. Since the conversion of inactive $PI3K$ to active is controlled by the receptor activity, the most simple model is given by

$$\begin{aligned} \frac{d}{dt} PI3K(t) &= -k_1 \; EpoR(t) \; PI3K(t) + g_1 \; aPI3K(t) \\ \frac{d}{dt} aPI3K(t) &= \; k_1 \; EpoR(t) \; PI3K(t) - g_1 \; aPI3K(t) \; , \end{aligned} \tag{5.26}$$

where k_1 is the activation rate of the $PI3K$, g_1 the degradation rate and due to the preparation of the cells $aPI3K(0) = 0$. Since the measurements of $EpoR$ are rather noisy as shown in Fig. 5.4a, we decided to model receptor activity with $EpoR(t) = A_0 \; (1 - e^{-\lambda_1 t}) \; e^{-\lambda_2 t}$, which yields an adequate description of the data. The estimate of the parameters in this function are $A_0 = 0.86$, $\lambda_1 = 0.33 \text{ min}^{-1}$, and $\lambda_2 = 0.007 \text{ min}^{-1}$, using a standard non-linear fitting procedure, see e.g. [14]. Apart from the unknown scaling parameter in both, $EpoR$ and $aPI3K$ all parameters are identifiable if ideal measurements would have been available. But according to Fig. 5.4b, the data are strongly corrupted by noise, resulting into parameter identifiability problems. To find all unidentifiable parameters the regularization procedure described in Sec. 5.4 is consulted. It turns out that fixing the unactivated PI3K to 1 finally yields an identifiable parameter estimation problem. For the remaining parameters we obtain

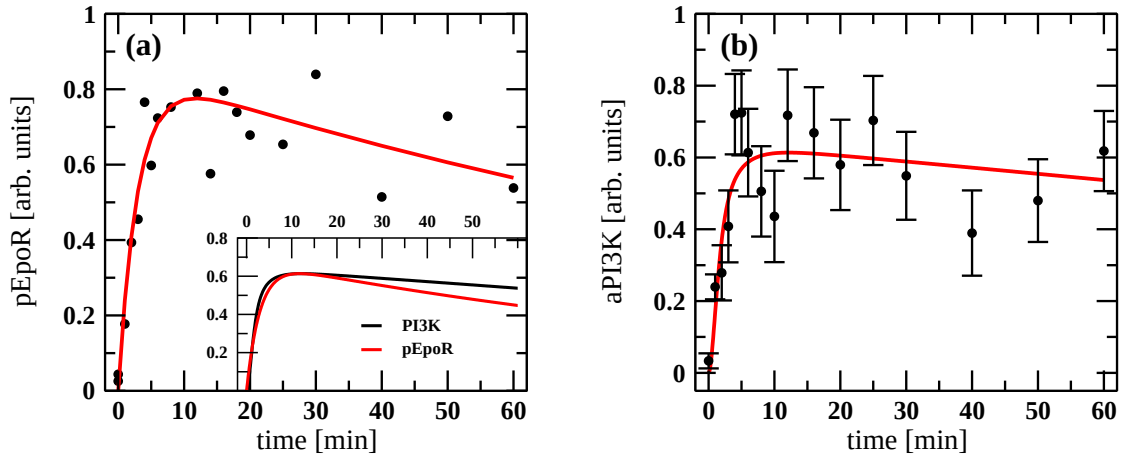

Figure 5.4: Modelling of the activation of the PI3 kinase ($PI3K$). (a) Since the noise on the measurements for the receptor activity (pEpoR) is rather high, its time course is approximated by $pEpoR(t) = A_0\ (1 - e^{-\lambda_1 t})\ e^{-\lambda_2 t}$ (red curve). As shown, this expression adequately describes the data and is thus suitable as input for Eq. 5.26. (b) Here, the red curve graphs the best fit of the model based on Eq. 5.26, yielding that the model is in accordance with the measurements. Moreover, a comparison of the receptor activity $EpoR$ with the concentration of the activated Pi3K is shown by the inset graph in (a). Note that $pEpoR$ is rescaled to compare both time courses. Up to 20 min the $aPI3K$ parallels the time course of $EpoR$, where the decay of the $aPI3K$ is slightly slower than the receptor signal.

$k_1 = 2 \pm 1.41\ \text{min}^{-1}$ and $g_1 = 0.98 \pm 0.74\ \text{min}^{-1}$. In fact, the obtained fit is consistent with the measurements, as shown by the red curve in Fig. 5.4b. A comparison of the rescaled receptor activity $EpoR(t)$ with $aPI3K(t)$ is shown in the inset graph of Fig. 5.4a. Up to 20 min the $aPI3K$ parallels the time course of $EpoR$, where decay of the $aPI3K$ is slightly slower than the receptor signal.

The remaining components of the signalling pathway can be modeled using a succession of two ODE subsystems which are equivalent to Eq. (5.26). In addition, this type of ODE can be solved analytically which allows a mathematical analysis helping to decide whether current picture of the pathway as shown in Fig. 5.3 is compatible with the measurements or not. Let us therefore represent Eq. (5.26) by the general expression

$$\begin{aligned} \frac{d}{dt}x(t) &= -\alpha\ f(t)\ x(t) + \beta\ y(t) \\ \frac{d}{dt}y(t) &= \quad \alpha\ f(t)\ x(t) - \beta\ y(t)\ . \end{aligned} \tag{5.27}$$

Here, $PI3K$ is replaced by x, $aPI3K$ by y, $EpoR$ by a positive function f, k_1 by α, and g_1 by β. The initial values are chosen to satisfy $x(0) = x_0 > 0$ and $y(0) = 0$. Since $x(t) + y(t) = x_0$ is conserved, Eq. (5.27) can be uncoupled which yields $\dot{y} = \alpha x_0\ f(t) - (\alpha\ f(t) + \beta)y$ for the output variable $y(t)$. This equation has the solution

$$y(t) = \alpha x_0 \int_0^t f(s)\ \exp\left(-\beta\ (t-s) - \alpha \int_s^t f(\tau)\ d\tau \right) ds\ . \tag{5.28}$$

In order to give a qualitative understanding of the dynamics obtained from Eq. 5.28, four different regimes of the ratio β/α are discussed in the following. Let us further assume that the time domain of interest is restricted to $[0, t_{max}]$. We observe:

1. $\beta/\alpha \gg t_{max}^{-1} \int_0^{t_{max}} f(\tau)\, d\tau$:

$$y(t) = \frac{\alpha}{\beta} x_0 \int_0^t f(s) \underbrace{\beta\, e^{-\beta(t-s)}}_{\approx \delta(t-s)} \exp\left(-\alpha \int_s^t f(\tau)\, d\tau \right) ds \approx \frac{\alpha}{\beta} x_0\, f(t)\,.$$

   Therefore, $y(t)$ approximately follows the dynamics of $f(t)$.

2. $\beta/\alpha \ll t_{max}^{-1} \int_0^{t_{max}} f(\tau)\, d\tau$: The slowly varying term $e^{-\beta(t-s)}$ can approximated by $e^{-\beta t}$:

$$\begin{aligned} y(t) &\approx \alpha x_0\, e^{-\beta t} \int_0^t f(s)\, e^{-\alpha \int_s^t f(\tau)\, d\tau}\, ds = x_0\, e^{-\beta t} \int_0^t \frac{d}{ds}\, e^{-\alpha \int_s^t f(\tau)\, d\tau}\, ds \\ &= x_0\, e^{-\beta t} \left(1 - e^{-\alpha \int_0^t f(\tau)\, d\tau} \right). \end{aligned}$$

   Since $\alpha\, t_{max}^{-1} \int_0^{t_{max}} f(\tau)\, d\tau$ is large compared with β, $y(t)$ is rushing up quickly which is followed by a slow decay.

3. $\beta/\alpha \approx t_{max}^{-1} \int_0^{t_{max}} f(\tau)\, d\tau$ and $\beta \gg 1$: For this regime, $\alpha \int_s^t f(\tau)\, d\tau$ can approximated by $\beta(t-s)$, leading to

$$y(t) \approx \alpha x_0 \int_0^t f(s)\, e^{-2\beta(t-s)}\, ds \approx \frac{\alpha}{2\beta} x_0\, f(t)\,,$$

   where a similar approximation as in 1. has been used. Again, the dynamics of $y(t)$ approximately follows $f(t)$.

4. $\beta/\alpha \approx t_{max}^{-1} \int_0^{t_{max}} f(\tau)\, d\tau$ and $\beta \ll 1$: By similar approximations than used in case 2 and 3, we have

$$y(t) \approx \alpha x_0 \int_0^t f(s)\, e^{-2\beta(t-s)}\, ds \approx \alpha x_0\, e^{-2\beta t} \int_0^t f(s)\, ds\,.$$

   The long term limiting factor is $e^{-2\beta t}$ leading to a slow decay similar to case 2.

Motivated by the slow decay of $EpoR(t)$, consider that $f(t)$ also decays slowly. Then, no acceleration in the decay of $y(t)$ can be expected if either of the discussed cases are regarded. Moreover, let $\beta/\alpha \approx t_{max}^{-1} \int_0^{t_{max}} f(\tau)\, d\tau$, thus $y(t)$ is still related to the convolution of $f(t)$ with $e^{-2\beta t}$ and therefore an acceleration of the decay cannot be achieved, a result which is independent of β.

Let us return to the PI3K pathway. The second step consists of two successive reactions, the conversion of PIP_2 to PIP_3 and the activation of Akt. As it can be seen in Fig. 5.3, Akt

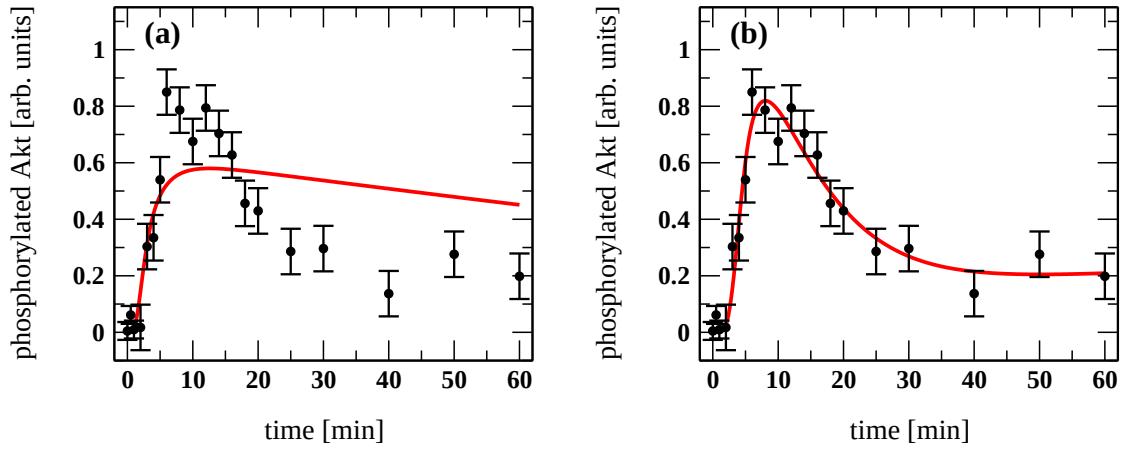

Figure 5.5: Shown is the time course of the phosphorylated Akt and two attempts to describe the data by a mathematical model. (a) The best fit of the model given by Eq. (5.29) to the measurements. As expected by an analysis of the system's equations the model cannot adequately describe the data. (b) However, the extension of the model given by Eq. (5.30) yields an almost prefect description of the data. Here, the degradation of PIP_3 to PIP_2 is driven by the time delayed Epo-receptor activity.

itself and the Ser 473 kinase bind to a specific binding site of PIP_3. Phosphorylation of Akt can only happen if the PIP_3-Akt and PIP_3-Ser 473 kinase complexes are in proximity, which is the rate limiting factor for the activation of Akt. According to [130] Akt and the Ser 473 kinase accumulates at the plasma membrane, therefore the binding of PIP_3 to Akt and to the Ser 473 kinase can safely omitted. The activation of Akt is thus proportional to $PIP_3^2(t)$, where $PIP_3(t)$ denotes the concentration of PIP_3. Let us further denote the concentration of PIP_2 by PIP_2, the inactive Akt by Akt and the phosphorylated (active) Akt by $pAkt$. The reaction scheme is then translated into an ODE by

$$\begin{aligned}
\frac{d}{dt}PIP_2(t) &= -k_2\ aPI3K(t)\ PIP_2(t) + g_2\ PIP_3(t) \\
\frac{d}{dt}PIP_3(t) &= \ \ k_2\ aPI3K(t)\ PIP_2(t) - g_2\ PIP_3(t) \\
\frac{d}{dt}Akt(t) &= -k_3\ PIP_3^2(t)\ Akt(t) + g_3\ pAkt(t) \\
\frac{d}{dt}pAkt(t) &= \ \ k_3\ PIP_3^2(t)\ Akt(t) - g_3\ pAkt(t)\ ,
\end{aligned} \tag{5.29}$$

where k_2, k_3, and g_2, g_3 are the rate constants for activation and degradation respectively. Due to preparation of the cells the initial concentrations of PIP_3 and the activated Akt and are again zero. In fact, Eq. (5.29) is equivalent to the connection of two systems described by Eq. (5.27) in series. This allows a mathematical analysis for Eq. (5.29) to decide whether the model is capable to describe the data. The concentration of the phosphorylated Akt is shown in Fig. 5.5. It can be seen that this concentration quickly increases within the first 10 min after the stimulus but also quickly decreases afterward. In contrast, the concentration of active PI3K only decreases slowly after 10 min, as shown in Fig. 5.4b on p. 68. Since any of the analyzed cases of Eq. (5.28) does not yield and accelerated decay with respect to the input

function, Eq. (5.29) cannot describe the dynamical behavior of the measurements. This is confirmed by the application of the fitting procedure. As shown in Fig. 5.5a the best fit using Eq. (5.29) does not reproduce the fast decay of $aAkt$ after 10 min. Note that all parameters and remaining initial conditions cannot be identified having only one observed component. Again, the regularization method is used to find all unidentifiable parameters. This leads to the fixation of $PIP_2(0)$ and k_3 to 1 for the fitting process. However, the estimates of the remaining parameters are no longer of great importance since they scale with the actual values of $PIP_2(0)$ and k_3 in a non-trivial way.

The degradation of PIP_3 to PIP_2 may be influenced by other proteins such as SHIP1, SHIP2, and PTEN [130, 132]. Assuming that these processes itself are regulated by the Epo-receptor, the model is extended by replacing g_2 with $g_2\ EpoR(t-\tau)$, where $EpoR(t-\tau)$ is the time delayed receptor activity which is assumed to vanish for all $t < \tau$. The introduction of the delay $\tau \geq 0$ can be regarded as an approximation to unknown processes which are responsible for the accelerated decay of $pAkt$. The complete ODE of the modified model therefore yields

$$\begin{aligned}
\frac{d}{dt}PIP_2(t) &= -k_2\ aPI3K(t)\ PIP_2(t) + g_2\ EpoR(t-\tau)\ PIP_3(t) \\
\frac{d}{dt}PIP_3(t) &= \ \ k_2\ aPI3K(t)\ PIP_2(t) - g_2\ EpoR(t-\tau)\ PIP_3(t) \\
\frac{d}{dt}Akt(t) &= -k_3\ PIP_3^2(t)\ Akt(t) + g_3\ pAkt(t) \\
\frac{d}{dt}pAkt(t) &= \ \ k_3\ PIP_3^2(t)\ Akt(t) - g_3\ pAkt(t)\ ,
\end{aligned} \tag{5.30}$$

Figure 5.5b shows the fit of Eq. (5.30) to the measurements. From this fit it can be concluded that the model extension leads to a model which is able to describe the data. The estimated delay is $\tau = 11.36 \pm 2.84$ min. Such a large delay may arise by either spatial effects due or by a signalling cascade used to regulate the degradation of PIP_3 to PIP_2 rather than a single signalling protein. The first alternative is not likely since all processes are taking place in proximity of the receptor. We can therefore conclude that a multi-component reaction scheme is needed for this feed-forward loop, which can only be identified with the aid of further experiments.

5.7. Conclusion

In this Chapter, the parameter estimation procedure for ordinary differential equations, multiple shooting, is described in detail. Apart from other attempts of estimating parameters in differential equations, this procedure does not heavily suffer from the attraction to local minima and the speed of convergence is considerably higher than global optimization methods can achieve. Besides the general idea of embedding the problem into a higher dimensional parameter space, the speed of convergence as well as the stability can only be achieved by sophisticated numerical methods. Especially the condensation algorithm and the damping strategy can be considered as landmarks of this issue. These aspects are thoroughly presented

within the remaining issues of the method, such as integration of the ODE, minimization and the statistical analysis of the estimates. Identifiability of the parameters can be regarded as central assumption for a successful operation of most of the numerical components. A regularization procedure to weaken this assumption is included to the discussion of multiple shooting. The regularization can further help to remove all unidentifiable parameters as demonstrated in Sec. 5.6. In addition, a simulation study using a recently proposed model of a cellular process of calcium signalling demonstrates that multiple shooting clearly outperforms the initial value approach.

Moreover, an extension of multiple shooting to partial differential equations is also possible, [133, 134]. Additionally, the method can also be used to find an optimal experimental design, see e.g. [135, 136]. This broad applicability of the multiple shooting method marks the relevance of such a tool for a vast range of applied sciences and engineering. Especially for estimating parameters in complex reaction networks, as they often appear in systems biology, multiple shooting can substantially assist the modelling procedure. This is underlined by the application of the proposed method to an important signalling pathway, the PI kinase. Paired with a mathematical analysis of a model obtained from the current biological knowledge of the PI kinase, the method substantially helped to identify a feed-forward loop which is needed to obtain an adequate model.

6

Quantifying the Substitution Rate Variation Across Mammalian Genomes

6.1. Introduction

The structure of the DNA was discovered by the biologist J. Watson and the physicist F. Crick in 1953. They found that the four bases of the DNA, guanine, cytosine, thymine, and adenine are organized in a double helix structure consisting of two strands. Each base on one strand can only bind to a complementary base on the other strand, where guanine is complementary to cytosine and thymine is complementary to adenine. The genetic information of each life form is encoded in the DNA which is itself partitioned to several chromosomes, e.g., 22 non sex specific chromosomes for the human and 19 for the mouse. Pieces on the DNA, or genome which are corresponding to protein synthesis are called genes. Only a small fraction of the entire genetic material are genes, about 2% for the human. Not all parts of the genes, however, are coding for proteins. The non-coding part of a gene is called intron and coding part is referred to as exon.

Rarely occurring changes in the sequence of the base composition of the DNA are called substitutions. Substitutions are essential for the evolution of species. In fact, the rate at which DNA undergoes substitutions varies not only between mammalian species [137-140] but even across a single genome and over time [141-143]. Various models accounting for this variation have been suggested [141, 143-145], but the cause of this the variation remains unknown. A second significant substructure of the genome is the local GC content, which is the proportion of cytosine (C) and guanine (G) nucleotides in a local region of the genome. The GC content varies over large length scale of the DNA, typically about 150 kbp (kilo base pairs). Structures of a elevated GC content are called GC isochores. Despite their existence, the evolutionary origin remains unclear [146]. Numerous models have been proposed to both account for this isochore structure and to determine whether it is in a state of decay, but no

consensus has been reached in either case [147, 148]. In this Chapter, the local substitution rate and the GC content are incorporated into a single model, thereby providing a unified description for both processes. Before being able to tackle this question, a reliable estimate of the substitution rate across the genome is needed.

There are numerous approaches to estimate the substitution rate pattern based on inter-species comparisons of certain sequences, e.g. [142, 143]. However, the usage of different species results in a convolution of species or lineage specific features of the substitution rate to the final estimate. At first glance, calculating substitution rates based on a single species seems to be impossible since the only available source is the sequence one observes today. Fortunately, nature has invented a curiosity which allows the calculation of the substitution rate, resolved in space (the position on the genome) and time. This is the presence of repetitive elements in the genome, short sequences occurring in an immense number of copies. Different types of these repetitive elements (in short repeats) have been copied at distinct times into the genome. These types are called repeat families in the following. Most of the repeats are equipped with a copying mechanism allowing them to spread over the whole genome. Others however are making use the of the copying mechanism by attaching themselves to other repeat families such that those can carry them along. Thereby, they act like freeloaders on a molecular scale. Due to this copying process the total amount of copies of a single repeat family can reach up to five million in the human genome. Since the typical size of the repeats itself lies between hundred and a few thousand base pairs (bp), about 40% of the entire human genome consists of repetitive element specific bases. In addition, the high copy number provides the possibility to reconstruct the ancestral or consensus sequence of each family. Of course these differ from the copies in today's genome because of substitutions which have been occurred after they entered the DNA. In total, about 800 different repeat families can be identified which are almost uniformly covering the last 150 Myr (million years. The spatial resolution is high enough of in order to find still 40 kb of repeat specific base pairs in stretches of about 150 kb (on average) for the human genome. Note that the aforementioned criteria of the repetitive elements are also roughly valid in the genomes of mouse, rat, dog, and chimpanzee. This massive occurrence of repetitive elements naturally raise the question of the rôle they play in the genome. Concerning this question, in [149] the author comes to the conclusion that due to the cut and paste mechanism described above, repeats are reshaping the genome which might lead to beneficial effect for the species. The results presented in [150] suggests that repeats are speeded up the evolution of the dog's morphology. These works are suggesting that at least some repetitive elements have or might have had some function and are not just so called "junk DNA". Repetitive elements can be classified by the GC content, size, and their copying mechanism. Three major groups are ALUs, LINEs, and DNA-transposons. ALUs are GC rich, whereas LINEs and DNA-transposons are mostly GC-low. The size of the three types is also quite distinct: $80-300$ bp for the ALUs, $6-8$ kbp for LINEs, and 80 bp-3 kbp for DNA-transposons. There are also differences in the copying mechanism between these groups, for more details see [151].

As already mentioned, the consensus sequence of the repeat families can be reconstructed. These reconstructed sequences are available at the RepBase [152]. Aligning the consensus sequence using the RepeatMasker software [152], provides the input for our method. A sample

output of the alignment procedure is given below.

```
chr1          1405 AGACAAATTCTCGGCCGACCTCATTGATCCTCGCCTCCTGGCGTTCACGC 1454
                       i i   vi vi i  i vv      i          i
MLT1E            7 AGACAGACTCTAAGGTGGCCCCCATGATCCCCGCCTCCTGGTGTTCACGC 56

chr1          1455 GCTTGTGTAATCTGCTCCCCTTAAGTGTGAGTGGAATCTGTGACTTGCTT 1504
                   v           iv        i      i    i i
MLT1E           57 CCTTGTGTAATCCCCTCCCCTTGAGTGTGGGTGGGACCTGTGACTTGCTT 106
```

Here, red letters are representing the sequence of today's genome and the blue letters are the corresponding aligned consensus sequence. Note that the four bases of the DNA are abbreviated by: A for adenine, C for cytosine, G for guanine , and T for thymine. Substitutions are marked by black letters, where **v** relates to the twelve transversions ($A \to C$, $T \to G$, $A \to T$, $T \to A$, $C \to G$, $G \to C$,$C \to A$, and $G \to T$) and **i** denotes the remaining four transitions. ($A \to G$, $T \to C$, $G \to A$ and $C \to T$). Since the four bases of the DNA belong to two chemically different groups: purins (A, G) and pyrimidins (C, T), substitutions leading to a base of a chemically different group are called transversions. Whereas, substitutions of bases within either purins and pyrimidins are called transitions. Using this source of data a model for the evolution of non-coding DNA is proposed to relate the outcome of the RepeatMasker to the substitution rate pattern. This model is based on the following three observations:

1. In terms of practical use, the computation of absolute substitution rates is unnecessary. Instead, it is sufficient to estimate the substitution rate relative to the genomic average.

2. Without loss of accuracy the problem can be greatly simplified if relative rates of substitution types are assumed to be constant for a certain point in time and location on the genome, e.g., the quotient of the rate for the substitution $A \to C$ with that of $A \to G$ is constant.

3. Substitution rate estimations reflecting random noise introduced by the data collection methods which can be filtered out by the application of statistical tools.

These observations lead to a model which is considerably less complex than other models discussed in the literature, e.g., the model proposed by Arndt et al. [153]. To obtain a deeper insight in the processes which may cause the mutative events across the DNA, a simple description is more powerful than an unnecessary complex description.

The remaining Chapter is organized as follows: A model for the evolution of non-coding DNA based on the observations above is formulated in Sec. 6.2 and the issue of applying the model to the RepeatMasker data is given in Sec. 6.3. In Sec. 6.4 the used noise-filtering procedure is discussed. Furthermore, a model extension taking nearest neighbor interactions into account, thus leading to a significantly more complex model is addressed in Sec. 6.5. It is shown that by ignoring this neighbor effect no significant lost in accuracy may be seen. First, results using inter-species comparisons are presented in Sec. 6.6, whereas a validation of the model assumptions and the results are given in Sec. 6.7. Biological issues, namely the conservation of the substitution rate pattern during the time course and its relation to the GC isochore structure is addressed in Sec. 6.8. This leads to the discussion of a possible cause for the substitution rate pattern, given in Sec. 6.9.

γ	Partition index	α	Index denoting a repeat family
Z	Number of partitions	M	Number of repeat families
t	Time ($t = 0$ denotes present)	t_α	Age of repeat family α
$C_1, \ldots, C_7$	Label of an age-class	t_i	Mean age of age class C_i
$m_\gamma(t)$	Substitution rate over partition γ at time t	$m(t)$	$\frac{1}{Z}\sum_\gamma m_\gamma(t)$
$\tau_\gamma(t)$	$m_\gamma(t) - m(t)$	$\overline{f}_\alpha$	Average value of $f(t)$ over interval $(-t_\alpha, 0)$
$[p_\gamma(t)]_i$	Probability a Markov chain in γ is in state i at time t	$R_\gamma(t)$	Rate matrix for Markov chain γ at time t
$Q_{\alpha\gamma}$	Transition rate matrix for Markov chain γ over time interval $(-t_\alpha, 0)$, connecting the initial probability $p_\gamma(-t_\alpha)$ to $p_\gamma(0)$	q	Relative rate matrix for all Markov chains
$t_\alpha \overline{m}_\alpha$	t_α in scaled units	$\overline{\tau}_{\alpha\gamma}/\overline{m}_\alpha$	τ_γ averaged over $(-t_\alpha, 0)$ in scaled units
σ_α^2	$Z^{-1}\sum_\gamma(\overline{\tau}_{\alpha\gamma})^2$ variance of $\overline{\tau}_{\alpha\gamma}$	σ_α	$\sqrt{\sigma_\alpha^2}$ – standard deviation.
$[k_{\alpha\gamma}]_{ij}$	Number of family α's base positions in γ containing base-type i at the time of α's insertion and base-type j at present.	$[N_{\alpha\gamma}]_i$	Number of family α's base positions in γ containing base-type i at the time of α's insertion.

Table 6.1: Summary of the used Notation. Definitions are chosen to be mostly consistent with [154].

6.2. A Model for the Evolution of Non-Coding DNA

Ideally one would like to compute the substitution rate for each base at any given instant of time, but such a goal is unlikely to ever be achieved. What can be done is to estimate aspects of the substitution rate by grouping bases in terms of time and location on the DNA. The first aspect will be achieved by calculating average rates over a given time period terminating at the present time. While the second issue will be achieved by dividing the genome into partitions, or windows, that will reflect the variation. To calculate the spatial variation of the substitution rate the genome is divided into Z partitions, where a given partition is denoted by the index γ. Note that a summary of the used notation is given in Tab. 6.1. Moreover, the model assumes that the substitution rate over any window γ is constant, but that these rates can vary between windows. The three functions further below will be of primary interest for the following investigation:

- $m_\gamma(t)$: The substitution rate of partition γ at time t.
- $m(t) = \frac{1}{Z}\sum_\gamma m_\gamma(t)$: The genome-wide averaged substitution rate at time t.

- $\tau_\gamma(t) = m_\gamma(t) - m(t)$: The variation of the substitution rate of partition γ from the genome mean.

Note that the last quantity is the value which will be estimated. However, this is only possible up to a constant factor. While the substitution rate and its variation is discussed as a function of time, it is impossible to actually determine those value for a specific point in time. Instead, the average over certain time periods is considered. In general, the time-averaged value of a function $f(t)$ over the period (t_1, t_2) is denoted by:

$$\overline{f} = \frac{1}{t_2 - t_1} \int_{t_1}^{t_2} f(t)\ dt$$

In the following we reference a timeline in which the modern genomes occur at time 0, with negative time values denoting the past. As mentioned in Sec. 6.1 the calculations are built on an analysis of repeat families: sets of interspersed repeats that share a common progenitor. As source of information on modern instances of each family, as well as the reconstruction of each family's common ancestor sequence the RepeatMasker [152] is used. Throughout this Chapter, the index α represents a given repeat family and t_α denotes the age of repeat family α. Thus, t_α is the positive number such that repeat family α was inserted at time $-t_\alpha$. In the following analysis we will often need to consider the time-averaged value of some function $f(t)$ over the time that repeat family α has existed in the genome, i.e., over the time period $(-t_\alpha, 0)$. This will be denoted by $\overline{f}_\alpha$. Subject of our investigation is $\overline{\tau}_\gamma$, the value $\tau_\gamma(t)$ averaged over time. The interest in $\overline{\tau}_\gamma$ derives from observation 1 in Sec. 6.1 on p. 75, namely that the determination of the absolute substitution rate is not necessary. From this observation it also follows that we need only to estimate this value up to a constant factor. Estimating $c\overline{\tau}_\gamma$ for some constant c is considerably easier then the estimation of $\overline{m}_\gamma$ itself. This results in a reduction of the complexity of the presented model.

Let us assume that the substitution rate of a base is memoryless and independent of the base's neighbors, allowing us to model the problem with continuous, non-stationary Markov chains. Conceptually, each base position is represented by a single chain, whereas the parameters are fixed for chains within a partition but varying between partitions. These chains consist of four states representing the possible contents of the base position. Here, the states are numbered states from 1 to 4 and define the correspondence as: $A\hat{=}1$ (adenine), $C\hat{=}2$ (cytosine), $G\hat{=}3$ (guanine), and $T\hat{=}4$ (thymine). Since our analysis is based on data extracted from interspersed repeats, a model for the propagation of the repeat's base substitutions is needed. The initial model assumes a star phylogeny in which each family was active for a brief time – resulting in the creation of numerous copies that are essentially identical at the time the family becomes inactive. It has been reported that 90% of all repeat families are conform to the phylogenic star model [141]. In Sec. 6.7 we will show that while the formulation makes this assumption, the presented model can tolerate considerable deviations from the assumed repeat model.

In the following a master equation is derived, Eq. (6.6), that allows to relate $\overline{\tau}_\gamma$ to data produced by the RepeatMasker [152]. The nucleotide content of a specific partition γ is modeled by a series of identical continuous Markov chains. Consider the probability that this

chain occupies a given state at time t is denoted by the four component row-vector $p_\gamma(t)$. Thus, $[p_\gamma(t)]_i$ is the probability that in partition γ and at time t the chain occupies state i. Equivalently, $[p_\gamma(t)]_i$ can be regarded as the probability that a randomly selected base from partition γ at time t is in state i. Since $p_\gamma(t)$ represents a probability distribution, is must satisfy $\sum_i [p_\gamma(t)]_i = 1$ for any t. A Markov chain for partition γ is defined by a state-transition rate matrix that depends on time t and is represented by $R_\gamma(t)$. For $i \neq j$, the value $[R_\gamma(t)]_{ij}$ is the rate at which state i will undergo a state transition to state j. By the theory of time continuous Markov processes this leads to

$$\frac{d}{dt} p_\gamma(t) = p_\gamma(t)\ R_\gamma(t)\ . \tag{6.1}$$

In order to ensure that $p_\gamma(t)$ remains a probability distribution, $\sum_j \frac{d}{dt} [p_\gamma(t)]_j = 0$ must be satisfied and therefore $\sum_j [R_\gamma(t)]_{ij}$ must vanish. This is ensured by setting the diagonal elements $[R_\gamma(t)]_{ii}$ to a negative value such that each row of $R_\gamma(t)$ sums to zero. These elements represent the rate at which the chain will leave state i. It then follows that for any given t_0 and $t > t_0$:

$$p_\gamma(t) = p_\gamma(t_0)\ \exp\left(\int_{t_0}^{t} R_\gamma(t')\ dt'\right)\ . \tag{6.2}$$

The expression $\exp\left(\int_{t_0}^{t} R_\gamma(t')dt'\right)$ in Eq. (6.2) is a 4×4 matrix that connects the state of a chain at t_0 to a state at t and will be denoted by Q. In particular, we are interested in the matrix connecting the states at a time $-t_\alpha$ when repeat-family α was copied into the genome and today ($t = 0$). This quantity is defined by

$$Q_{\alpha\gamma} = \exp\left(\int_{-t_\alpha}^{0} R_\gamma(t')\ dt'\right)\ . \tag{6.3}$$

By observation 2 in Sec. 6.1 on p. 75, the relative rates of substitutions for the individual bases are constant in time and space. In other words, while $R_\gamma(t)$ as whole is time-dependent, any ratio of its components $[R_\gamma(t)]_{ij} \,/\, [R_\gamma(t)]_{i'j'}$ is constant in time and not dependent on location. This approximation allows us to assume the existence of a time-independent relative rate matrix q such that

$$R_\gamma(t) = m_\gamma(t)\ q\ , \tag{6.4}$$

where the local mutation rate $m_\gamma(t)$ is a scalar function which describes the over-all dependence of $R_\gamma(t)$ on time and space. The ratio of two elements of q thus represents the relative probabilities of the corresponding substitution rates. This implies that q is fixed only up to a common multiplicative factor. More precisely, while the value of the product $m_\gamma(t)\ q$ is fixed, q might be multiplied by factor c whereas the impact of c is compensated by setting $m_\gamma(t)/c$. As with matrix $R_\gamma(t)$ it must be ensured that $q_{ii} = -\sum_{j \neq i} q_{ij}$. Thus, all diagonal elements of q are dependent quantities. It follows from strand-symmetry that of the twelve off-diagonal elements only six are independent. Here, strand-symmetry is the assumption that the substitution rate of each transition on one strand is the same on the complementary

strand of the DNA, e.g., the rate of $A \to C$ is assumed to be the same than $T \to G$, since T is the complementary base of A, and G that of C. These remaining substitution rates are referred to as $q_1, \ldots, q_6$. Since q can only estimated up to a constant factor, the previously discussed freedom is fixed by setting $q_1 = 0.05$. This rate reflects the transition $A \to C$ and $T \to G$. Now, we observe from Eq. (6.4) that

$$\begin{aligned} \int_{-t_\alpha}^{0} R_\gamma(t')\, dt' &= q \int_{-t_\alpha}^{0} m_\gamma(t')\, dt' = q \int_{-t_\alpha}^{0} \big(m(t') + \tau_\gamma(t')\big)\, dt' \\ &= qt_\alpha\, (\overline{m}_\alpha + \overline{\tau}_{\alpha\gamma}) = qt_\alpha\, \overline{m}_\alpha\, \left(1 + \overline{\tau}_{\alpha\gamma}/\overline{m}_\alpha\right), \end{aligned} \tag{6.5}$$

where $m_\gamma(t) = m(t) + \tau_\gamma(t)$ and recalling that $\overline{\tau}_{\alpha\gamma}$ is $\tau_\gamma(t)$ the averaged substitution rate variation over the period $(-t_\alpha, 0)$. Combining Eq. (6.3) and Eq. (6.5) we finally arrive at the central equation which manifests the used evolutionary model for the investigated non-coding DNA. This equation reads

$$Q_{\alpha\gamma} = \exp\left(qt_\alpha\, \overline{m}_\alpha\, \left(1 + \overline{\tau}_{\alpha\gamma}/\overline{m}_\alpha\right)\right). \tag{6.6}$$

The left hand side of this equation refers to a set of matrices derived from the RepeatMasker data, one matrix for every repeat type α in each partition γ. Of course, no matrix can be established if a particular repeat family does not occur in a certain partition. If M is the number of repeat families and Z the number of partitions, maximal $Z \cdot M$ matrices $Q_{\alpha\gamma}$ are available. This set of matrices is the input used to estimate on the right hand side of Eq. (6.6): (i) the independent components of q, (ii) the M values of $t_\alpha \overline{m}_\alpha$, and (iii) the actual local mutation rate patterns $\overline{\tau}_{\alpha\gamma}/\overline{m}_\alpha$. Finally, from Eq. (6.5) can be seen that only time-averaged mutation-rates $\overline{\tau}_{\alpha\gamma}$ can be estimated.

6.3. Applying the Model to Sequence Data

Application of Eq. (6.6) to sequence data requires three steps: extracting repeat families through RepeatMasker, computing a maximum-likelihood fit of $Q_{\alpha\gamma}$ to the repeat data, estimating q, t_α for each repeat family, and $\overline{\tau}_{\alpha\gamma}$. The data obtained from the RepeatMasker provides the reconstructed ancestor of each repeat family, as well as a pair-wise alignment between each modern instance and the family's reconstructed ancestor. Alignment positions involving gaps are discarded. For each repeat family α and partition γ the following quantities are defined:

- $k_{\alpha\gamma}$: A 4×4-matrix such that $[k_{\alpha\gamma}]_{ij}$ is the total number of bases which started in state i at time $-t_\alpha$ and ended in state j at time 0, for each partition γ.
- The four dimensional vector $N_{\alpha\gamma}$: $[N_{\alpha\gamma}]_i = \sum_j [k_{\alpha\gamma}]_{ij}$ is the number of chains that were in state i at time $-t_\alpha$.

Using the RepeatMasker output the matrices $k_{\alpha\gamma}$ are obtained by counting the number of transitions from the consensus sequence to the aligned sequence. Moreover, each matrix $k_{\alpha\gamma}$

is a realization of a multinomial distribution, which is due to the counting process. In order to gain an estimate of $Q_{\alpha\gamma}$ a maximum-likelihood fit is applied in the following. Since $k_{\alpha\gamma}$ obeys a multinomial distribution and since the counts are independent with respect to the partition γ and the repeat family α, the likelihood reads

$$\mathcal{L} = \prod_{\alpha\gamma} \prod_{i} [N_{\alpha\gamma}]_i! \prod_{j} \frac{\left([Q_{\alpha\gamma}]_{ij}\right)^{[k_{\alpha\gamma}]_{ij}}}{[k_{\alpha\gamma}]_{ij}!} . \tag{6.7}$$

Therefore an estimate of $[Q_{\alpha\gamma}]_{ij}$ is given by searching for those values for $[Q_{\alpha\gamma}]_{ij}$ that maximize $\mathcal{L}$. Since the logarithm is a monotonous function, it is more convenient to maximize $\ln \mathcal{L}$ rather than $\mathcal{L}$. Furthermore, the additional constraint that $\sum_j [Q_{\alpha\gamma}]_{ij} = 1$ has to be taken into account which can be achieved using a Lagrange multiplier λ. This leads to the following necessary condition for the maximum

$$\frac{\partial}{\partial [Q_{\alpha\gamma}]_{ij}} \Big[\ln \mathcal{L} + \lambda \, \big(\sum_k [Q_{\alpha\gamma}]_{ik} - 1 \big) \Big] = 0 . \tag{6.8}$$

After the removing terms which are independent of $[Q_{\alpha\gamma}]_{ij}$, Eq. (6.8) can equivalently be formulated by

$$\frac{\partial}{\partial [Q_{\alpha\gamma}]_{ij}} \Big([k_{\alpha\gamma}]_{ij} \ \ln [Q_{\alpha\gamma}]_{ij} + \lambda \, [Q_{\alpha\gamma}]_{ij} \Big) = 0 .$$

This equation has the unique solution

$$[Q_{\alpha\gamma}]_{ij} = \frac{[k_{\alpha\gamma}]_{ij}}{[N_{\alpha\gamma}]_i} , \tag{6.9}$$

where λ is determined by demanding that the constraint $\sum_j [Q_{\alpha\gamma}]_{ij} = 1$ is satisfied. Moreover, the second derivative of $\ln \mathcal{L}$ with respect to $[Q_{\alpha\gamma}]_{ij}$ yields $-[k_{\alpha\gamma}]_{ij}/([Q_{\alpha\gamma}]_{ij})^2$ which leads after the insertion of Eq. (6.9) to $-([N_{\alpha\gamma}]_i)^2/[k_{\alpha\gamma}]_{ij}$. Since this expression is negative, the sufficient condition for a maximum of $\mathcal{L}$ is satisfied. Therefore, the matrices $Q_{\alpha\gamma}$ can be estimated using Eq. (6.9) which is accessible by the data obtained from the RepeatMasker.

The next step is to extract q and $t_\alpha \overline{m}_\alpha$ from $Q_{\alpha\gamma}$. This is done by considering the limiting case where $Z = 1$, thereby reducing the entire genome to single partition γ'. As there can be no variation across a single sample, it follows that $\overline{\tau}_{\alpha\gamma'} = 0$. Thus, Eq. (6.6) reduces to

$$Q_{\alpha\gamma'} = \exp\left(q \ t_\alpha \overline{m}_\alpha\right) . \tag{6.10}$$

Because there is only one partition, the index γ' is omitted in the following if the case $Z = 1$ is considered. For each of the M repeat families, now M 4×4-matrices Q_α are determined from Eq. (6.9) and thus $16 \cdot M$ data points are obtained. These data points are used to simultaneously calculate the five undetermined components of the matrix q, as well as the set of M scaled times $t_\alpha \overline{m}_\alpha$. This is done by a multidimensional fit of these $M + 5$ parameters to the $16 \cdot M$ data points of the matrices Q_α using the model described by Eq. (6.10).

The last step is to break the genome into Z partitions and estimate the local substitution rate pattern $\overline{\tau}_{\alpha\gamma}$ with the help of Eq. (6.6). Let us rewrite Eq. (6.6) as $Q_{\alpha\gamma} = \exp\left(q x_{\alpha\gamma}\right)$,

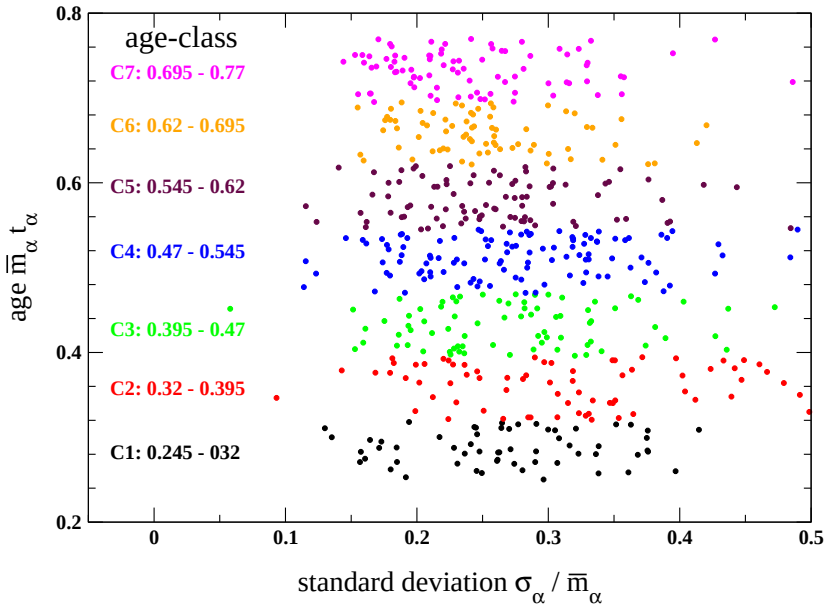

Figure 6.1: Shown is the standard deviation of the substitution rate pattern $\sigma_\alpha/\overline{m}_\alpha$ against the age of the repeat family $t_\alpha\ \overline{m}_\alpha$. Age classes $C_1, C_2, ..., C_7$ are defined by dividing the time interval into seven equally sized time segments, starting from $t_\alpha\ \overline{m}_\alpha = 0.245$ and ending at $t_\alpha\ \overline{m}_\alpha = 0.77$.

and calculate the best fits for $x_{\alpha\gamma}$ keeping q and $t_\alpha \overline{m}_\alpha$ fixed to the values determined by the previous step. The estimate of $\overline{\tau}_{\alpha\gamma}/\overline{m}_\alpha$ is then extracted from

$$\overline{\tau}_{\alpha\gamma}/\overline{m}_\alpha = \frac{x_{\alpha\gamma}}{t_\alpha \overline{m}_\alpha} - 1\ . \tag{6.11}$$

Note that if there was no copy of repeat-family α in, e.g., partition γ, $\overline{\tau}_{\alpha\gamma}/\overline{m}_\alpha$ cannot be computed for this partition. Thus, the actual amount of data for $\overline{\tau}_{\alpha\gamma}/\overline{m}_\alpha$ is slightly less than $M \cdot Z$ data points. To improve the statistics, $\overline{\tau}_{\alpha\gamma}/\overline{m}_\alpha$ is averaged over several sets of repeat families α. Because $\overline{\tau}_{\alpha\gamma}/\overline{m}_\alpha$ is time-averaged over the interval $(-t_\alpha, 0)$, this average should be limited to repeats of roughly the same age. Therefore, each repeat family α is assigned to one of the seven time classes $C_1, \ldots, C_7$ based on the estimated family age $t_\alpha \overline{m}_\alpha$. Moreover, the time classes where chosen such that roughly the same amount of repeat families are in each class. Extremely old and young repeats are therefore excluded. Figure 6.1 shows $t_\alpha \overline{m}_\alpha$ against the standard deviation $\sigma_\alpha/\overline{m}_\alpha$ of $\overline{\tau}_{\alpha\gamma}$, as defined in Tab. 6.1. Here, the seven age classes are coded by a distinct color. In total, the repeat families produce a signal around $\sigma_\alpha/\overline{m}_\alpha = 0.25$. The relative substitution rate pattern for each time class is estimated by averaging over all M_i members of the time-class

$$\overline{\tau}^i_\gamma/\overline{m} = \frac{1}{M_i} \sum_\alpha \overline{\tau}_{\alpha\gamma}/\overline{m}_\alpha\ . \tag{6.12}$$

To simplify the notation, the age-class index i is dropped in $\overline{m}$ for the expression above. In addition, the time t_i represents the average age of time-class C_i in our scaled units. The seven

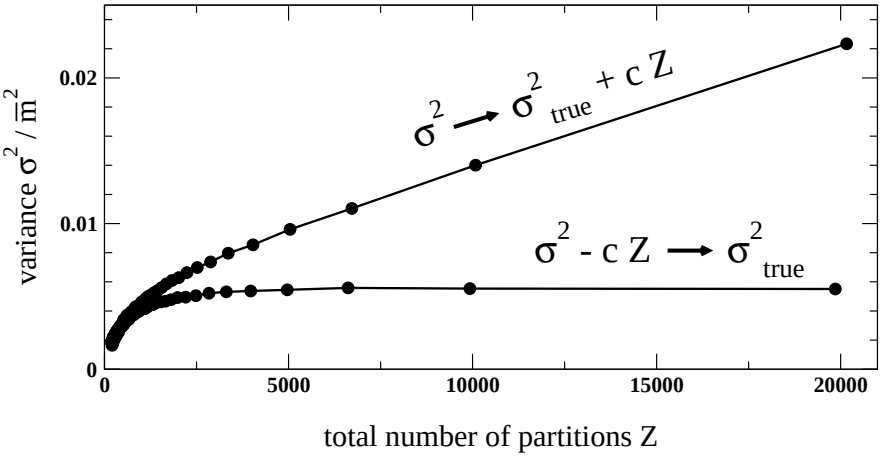

Figure 6.2: Dependence of the variance of the substitution rate pattern $\sigma^2/\overline{m}^2$ with respect to the number of used partitions Z. This relationship is exemplary shown for the time class C_6. The effect of uncorrelated observational noise superimposed on the data becomes visible by the straight line of the upper curve for $Z > 3000$. If the effect of the noise is corrected, a pronounced plateau arises (lower curve), showing that an increase of resolution beyond $Z > 3000$ does not substantially affect the underlying true variance $\sigma^2_{\text{true}}/\overline{m}^2$ of the pattern.

sets of values $\overline{\tau}^i_\gamma/\overline{m}$ are local rates averaged over time-periods of different length. This set yields information about the time dependence of the substitution rate pattern. In some cases an average over all seven age classes is needed. The resulting substitution rate pattern is then denoted by $\overline{\tau}_\gamma/\overline{m}$. In other cases we are interested in investigating the relation between the pattern and the repeats from which it is calculated. In these cases, two or more mutually exclusive subsets out of the M different repeat-families are defined and averaged over each subset as done in Eq. (6.12). Note that at the highest spatial resolution possible for the human genome, $Z = 22000$ or a partition size of approximately 150 kb (kilo base pairs), each partition is occupied by representatives from at least 10 different repeat families of each time-class and mostly more than 50. Since the estimated substitution rate pattern is strongly corrupted by observational noise, the underlying signal is reconstructed using a noise filtering approach. This procedure and its theoretical justification is subject of the following section.

6.4. Reconstruction of the Underlying Substitution Rate Pattern

Methods used to generate the raw data, e.g., the RepeatMasker, the RepBase reconstructions of the repeat's consensus sequence, and the genome sequencing, are not completely accurate. Errors introduced in generating these data will be reflected as random noise in $\overline{\tau}^i_\gamma/\overline{m}$. As this noise is independent of the actual signal it is possible to filter it out. Figure 6.2 both demonstrates the existence of this noise and demonstrates how to construct the filter. The top curve shows the variance $\sigma^2/\overline{m}^2 = Z^{-1}\sum_\gamma(\overline{\tau}^{i=6}_\gamma/\overline{m})^2$ for age-class C_6 as a function of

the number of used partitions Z. For the remaining section we suppress the scale parameter $\overline{m}$ for sake of clarity. In order to understand the shape of the curves in Fig. 6.2, let us assume that the genome has been divided into Z_0 partitions and that the signals in two neighboring partitions are uncorrelated. Let $Z = kZ_0$, where k is a positive integer, it then follows from the independence of the signals that $\sigma^2(Z) = k\ \sigma^2(Z_0)$. Since $k = Z/Z_0$ we arrive at $\sigma^2(Z)/Z = \sigma^2(Z_0)/Z_0$. Thus, for a noisy signal, $\sigma^2(Z)$ is a constant multiple of Z. However, in the upper curve of Fig. 6.2 the true underlying substitution rate pattern is contaminated with noise. If Z is large enough the underlying pattern becomes independent of Z, since further increasing the resolution no longer affects the average signal per partition. Here, the assumption is used that a characteristic length scale ΔL exists for the substitution rate pattern, such that the variation of the pattern is approximately constant on smaller length scales than ΔL. Thus, the variance of the noise free signal σ^2_{true} is constant. Hence, for a sufficiently large Z we expect to find

$$\sigma^2(Z) = \sigma^2_{\text{true}} + cZ\ ,$$

where c is constant. This is consistent with Fig. 6.2, where the upper curve straightens out at $Z \approx 3000$. This is also observed for each other time class. For $Z > 3000$ the unknown constant c can be estimated by a linear fit to the remaining data points, allowing us to calculate $\sigma^2(Z)_{\text{true}}$. This estimate of the variance for the underlying substitution rate pattern $\sigma^2(Z)_{\text{true}}$ is of great importance in order to optimize the noise-filtering process described further below. The shape of $\sigma^2(Z)$ for $Z < 3000$ can be explained as follows. Imagine that ΔW is the length of the interval over which the substitution rate pattern is evaluated. If $\Delta W > \Delta L$ then the calculated value represents an average over partitions where the pattern is not constant, thus introducing inaccuracies that result in a diminished estimate of the variance. Thus only if $\Delta W < \Delta L$ a faithful representation of $\overline{\tau}^{i=6}_{\gamma}$ is obtained and therefore a correct estimate of the variance. A further reduction of ΔW will have no effect on the results. From these results we can conclude that the characteristic length scale of the substitution rate pattern is approximately 1 Mb , corresponding to $Z = 3000$. Partition sizes larger than 1 Mb are yielding a coarse grained signal, whereas partition sizes less than 1 Mb produce identical results. This effect is demonstrated in Fig. 6.3. Here, the noise filtered substitution rate variation pattern $\overline{\tau}^{i=6}_{\gamma}/\overline{m}$ is shown for different partition sizes. As expected, hardly any effects are visible on the results using $Z = 22000$ partitions (black line) or $Z = 5000$ partitions (red line). But if $Z = 300$ partitions are used (blue line) the curve collapses toward the genome average, smearing out the fine structure of the pattern. Moreover, the same analysis technique shows that the necessary resolution size of 1 Mb holds for the mouse genome as well. Now, a completely adaptive noise filtering procedure is described to reconstruct the underlying signal.

Let us first designate the unfiltered mutation rate pattern as y_γ, which can be decomposed into two parts: the true signal τ_γ, and the noise contribution ϵ with variance σ^2. The noise ϵ is assumed to be independent with respect to the partition index γ. To simplify the notation the overline symbols are also omitted for the remainder of this section. Hence,

$$y_\gamma = \tau_\gamma + \epsilon\ . \tag{6.13}$$

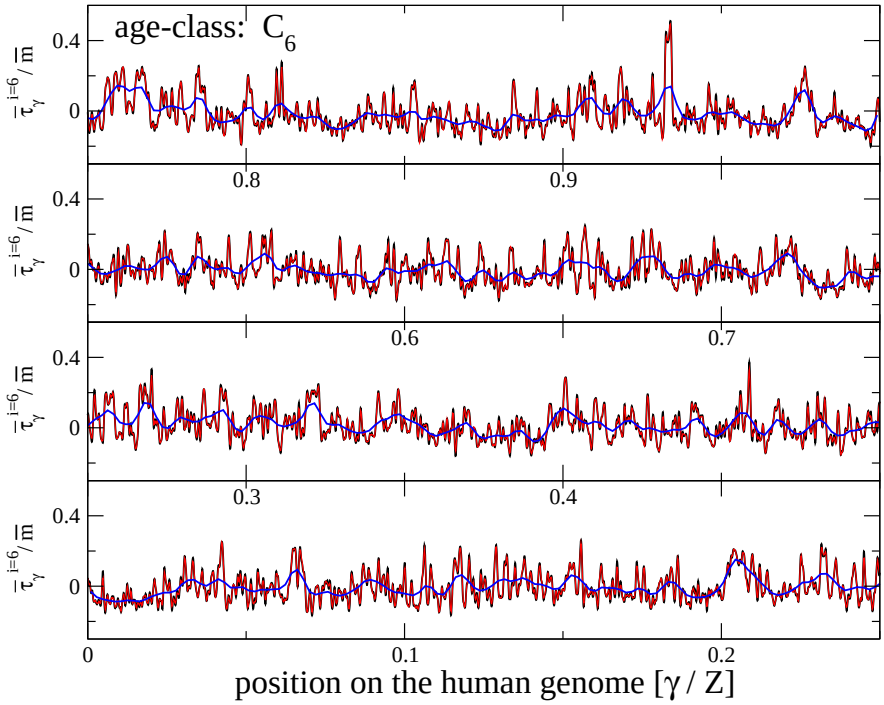

Figure 6.3: A graph showing the substitution rate $\overline{\tau}_\gamma^{i=6}/\overline{m}$ for age-class C_6 against its position. All 22 chromosomes of the human genome are linked together: the first partition $\gamma = 1$ is located on chromosome 1, while $\gamma = Z$ refers to the last partition located at the end of chromosome 22. If $\overline{\tau}_\gamma^{i=6}/\overline{m} = 0$ the corresponding partition γ has a substitution rate equal to the genome average; as $\overline{\tau}_\gamma^{i=6}$ increases (decreases), we find partitions with higher (lower) substitution rates. Each curve represents a different resolution: the genome was broken into $Z = 22000$ partitions for the black line, into $Z = 5000$ partitions for the red line, and into $Z = 300$ partitions for the blue line.

To estimate τ_γ on the basis of y_γ the data must be smoothed in order to remove the variation induced by the noise. This is possible if the true signal τ_γ is a smooth curve. The smoothing technique used to achieve the noise reduction has the following property: let $\mathbf{y} = (y_1, \ldots, y_Z)^t$ be the data vector defined by Eq. (6.13), where the superscript t denotes the transposition. The estimate for the signal $\hat{\tau} = (\hat{\tau}_1, \ldots, \hat{\tau}_Z)^t$ at each location γ is then given by

$$\hat{\tau} = S\mathbf{y}, \tag{6.14}$$

where S is a $Z \times Z$ matrix. Kernel smoothers, such as the running mean, are frequently used for this purpose, see e.g. [155]. Here, we decided to use smoothing splines, which are asymptotically equivalent to kernel smoothers [156]. The advantage of smoothing splines is that the reconstruction of sharply peaked signals is more accurate than using a kernel method. Some examples and comparisons to alternative smoothing procedures can be found in [157, 158].

Now, let us for a moment consider that the partition index γ is a continuous variable, permitting an interpolation between the partitions. By assuming that the unknown signal τ_γ in Eq. (6.13) is at least twice continuously differentiable, an additional term is added to the

usual least-squares function to penalizes the roughness of the estimate. Hence, the complete functional yields

$$\mathcal{L}(g) = \underbrace{\sum_{\gamma=1}^{Z} \frac{(y_\gamma - g_\gamma)^2}{\sigma^2}}_{least-squares} + \underbrace{\xi \int \left[\frac{d^2 g_\gamma}{d\gamma^2}\right]^2 d\gamma}_{penalty} \tag{6.15}$$

which has to be minimized with respect to g in order to obtain an estimate of τ_γ in equation (6.13). The smoothing parameter $\xi \geq 0$ determines the amount of smoothing, ranging from zero leading in interpolation to infinity enforcing linear regression. The observational error σ is often unknown, but it can be absorbed in the smoothing parameter by using $\tilde{\xi} = \xi\sigma^2$. Therefore, $\sigma = 1$ can always be assumed without loss of generality. The minimization of equation (6.15) within the class of twice continuously differentiable functions and vanishing second derivative at the boundary leads to natural cubic smoothing splines. Reinsch [159] showed that $\hat{\tau}_\gamma = \arg\ \min_g\{\mathcal{L}(g)\}$ are piecewise cubic polynomials which fit together such that the second derivative is continuous at the joints. An algorithm to calculate the parameters of these polynomials is given in [159, 160]. The crucial point of every smoothing method is the selection of the optimal smoothing parameter ξ balancing the variance and the squared bias of the reconstructed signal.

To find this optimal value for the smoothing parameter, suppose that $\hat{\tau}_{\xi,\gamma}$ is an estimate of the signal τ_γ that depends on the smoothing parameter ξ. Then the mean-squared error (MSE)

$$\mathrm{MSE}(\xi) = Z^{-1} \sum_{\gamma=1}^{Z} (\hat{\tau}_{\xi,\gamma} - \tau_\gamma)^2 \tag{6.16}$$

is an appropriate measure the quality of the reconstructed signal with respect to smoothing parameter ξ. Minimizing $\mathrm{MSE}(\xi)$ gives the optimal smoothing parameter, but the definition of the MSE still contains the unknown signal τ_γ. To deal with this unknown, we estimate MSE first. Thus, a minimization of the estimated MSE score with respect to ξ yields an estimate of the optimal smoothing parameter. This can be done by cross validation: let $\hat{\tau}^{(-i)}_{\xi,\gamma=i}$ be the estimated signal for partition i, whereas the i-th observation y_i is left out in the smoothing procedure. An estimate of MSE is then given by the cross validation score

$$\mathrm{CV}(\xi) = Z^{-1} \sum_{i=1}^{Z} \left(y_i - \hat{\tau}^{(-i)}_{\xi,\gamma=i}\right)^2 .$$

As shown in [160], the cross validation score is equivalent to

$$\mathrm{CV}(\xi) = Z^{-1} \sum_{i=1}^{Z} \left(\frac{y_i - \hat{\tau}_{\xi,\gamma=i}}{1 - S_{ii}(\xi)}\right)^2 .$$

Hence, $\hat{\tau}^{(-i)}_{\xi,\gamma=i}$ need not be calculated explicitly – an insight which considerably reduces the computational costs. But there is a weak point in this construction: consider a point y_i with

a strong influence on $\hat{\tau}_\gamma$. Due to the calculation of CV, leaving out y_i will significant effect the score. In order to correct this, these points should be weighted differently. An appropriate weighting leads to generalized cross validation introduced by Craven and Wahba [161]:

$$\mathrm{GCV}(\xi) \quad = \quad \frac{Z^{-1}\sum_{i=1}^{Z}\left(y_i - \hat{\tau}^{(-i)}_{\xi,\gamma=i}\right)^2}{\left(1 - Z^{-1}\mathrm{tr}\, S(\xi)\right)^2} \ , \tag{6.17}$$

where $\mathrm{tr}\, S(\xi)$ denotes the trace of S. The minimum of the GCV-score [162, 160] can be found with aid of standard nonlinear minimization routines, see e.g. [14]. Since the quality of every estimate depends on the quality of the data, the estimation of the optimal smoothing parameter is rather unstable if the data are too noisy. This might be a particular problem for the younger age classes. Therefore, an upper bound ξ_{max} is provided, which is chosen such that the variance of the reconstructed signal is consistent with the estimated variance of the underlying substitution rate pattern $\sigma^2(Z)_{\mathrm{true}}$.

6.5. The Effect of an Elevated C_pG Dinucleotide Substitution Rate

So far, a model for the evolution of non-coding DNA has been proposed containing six parameters. This model is referred to as the six-parameter model. In App. A we formulate an alternate seven-parameter model, where the seventh parameter, q_{C_pG}, accounts for the possibility of a C_pG methylation – a common effect that leads to higher rates of C_pG to T_pG or C_pA substitutions. The subscript p here indicates that the corresponding dinucleotides have been methylated. Methylation offers the possibility for passing information to the offspring without altering the sequence of the genome and provides an important mechanism to bequeath information to the next generation. Especially the methylation of the CG dinucleotides in the promoter region of a gene controls the protein synthesis of the corresponding coding region. Moreover, Arndt et al. argues that substitutions occurring in these sites are as much as 40 times higher than the rate of single-nucleotide substitutions [141]. Hence, ignoring this factor could reduce the accuracy of the estimations. It is shown in the following that the accuracy is not diminished, even with a C_pG substitution rate as high as predicted in [141]. The six-parameter model's failure to account for the C_pG substitution rates makes little difference to the final results. More precisely, it absorbs the actual value of q_{C_pG} into the estimation of q_6 and thus reducing the hypermutability of the C_pG dinucleotides to an effective rate q_6.

If the substitution rate of a base is dependent on its neighbors, then the state of a chain is no longer adequately described by $p(t)$. A more complex joint distribution $p(i, j, k; t)$ is needed, which denotes the probability that, at time t, a given chain is in state j and that its left and right neighbors are in state i and k respectively. For the 64 dimensional vector with components $p(i, j, k; t)$ a master equation, Eq. (A.5), is derived in App. A. Since this model contains seven parameters it is referred to as seven-parameter model to distinguish between the model presented in Sec. 6.2. This model is equivalent to the model formulated

			Analysis	
Rate	Transition	actual	C_pG: 0%	C_pG: 12.5%
q_1	$A \to C$ and $T \to G$	0.05	0.05	0.05
q_2	$A \to T$ and $T \to A$	0.05	0.052	0.048
q_3	$C \to G$ and $G \to C$	0.05	0.050	0.046
q_4	$C \to A$ and $G \to T$	0.05	0.052	0.050
q_5	$A \to G$ and $T \to C$	0.15	0.15	0.14
q_6	$G \to A$ and $C \to T$	0.15	0.19	0.27
q_{C_pG}	$C_pG \to C_pA$ and $C_pG \to T_pG$	2		

Table 6.2: Results on the consistency of model and simulation: The third column specifies the substitution rates actually taken in the seven-parameter model, while columns 4 to 5 present the results predicted by the six-parameter model in the presence of elevated C_pG substitution rates, showing the effect on a genome with an initial 0% C_pG content, and the effect on a genome with an initial 12.5% C_pG rate respectively.

and studied by Arndt et al. [153]. Note that the seven-parameter model reduces to the six-parameter model if the rate q_{CpG} is set to zero. If on the other hand $q_{C_pG} \neq 0$ then the seven-parameter model shows a richer dynamics, such that the reduced description in Eq. (6.2) can only be considered as an approximation. The quality of this approximation is studied in App. A by comparing the estimated age t_α in the six-parameter model with the actual values used in the simulation of the seven-parameter model. This offers the opportunity to study the expected error in the estimation of the transition matrix q and $t_\alpha \overline{m}_\alpha$. Table 6.2 shows resulting estimates for q under two conditions: first, when initial C_pG content is 0%, and second, when it is 12.5%. In both cases we assume that transition substitutions (q_5, q_6) occur at three times the rate of transversion substitutions $(q_1, \cdots, q_4)$, and use the prediction of Arndt et al. that C_pG dinucleotides experience a forty-fold increase in substitution rates [141]. The estimated versus actual values of q are presented in Tab. 6.2, keeping in mind that q is computed only up to a constant factor and hence results can be arbitrarily scaled. Under both conditions the estimations of q_1 through q_5 are accurate, whereas q_6 is overestimated in proportion to the initial C_pG content. The overestimation of q_6 is due to the fact that it is the only rate which is directly relevant to C_pG related substitution. This is because rate q_6 governs exactly the two transitions affected by the $C_pG \to C_pA$ and $C_pG \to T_pG$, namely $G \to A$ and $C \to T$. So by adapting rate q_6 to the data, at least some of the effects of the enhanced C_pG-specific rates can be taken into account.

Concerning the estimation of $t_\alpha\ \overline{m}_\alpha$, we find again that $t_\alpha\ \overline{m}_\alpha$ is subject to overestimation proportional to the initial C_pG content on the genome. With an initially small C_pG content very accurate estimates of $t_\alpha\ \overline{m}_\alpha$ are obtained, while a C_pG content of 12.5% leads to as much as a 20% overestimation in $t_\alpha\ \overline{m}_\alpha$, see App. A for more details. Mammalian genomes have fairly low C_pG content ($\approx 1\%$), and hence the estimates using the six-parameter model are expected to be quite accurate. More importantly, the results justify the technique of removing C_pG cites before performing the computations – a method frequently used but whose validity have been disputed in [141]. Having thus justified this technique, after blocking-out all C_pG

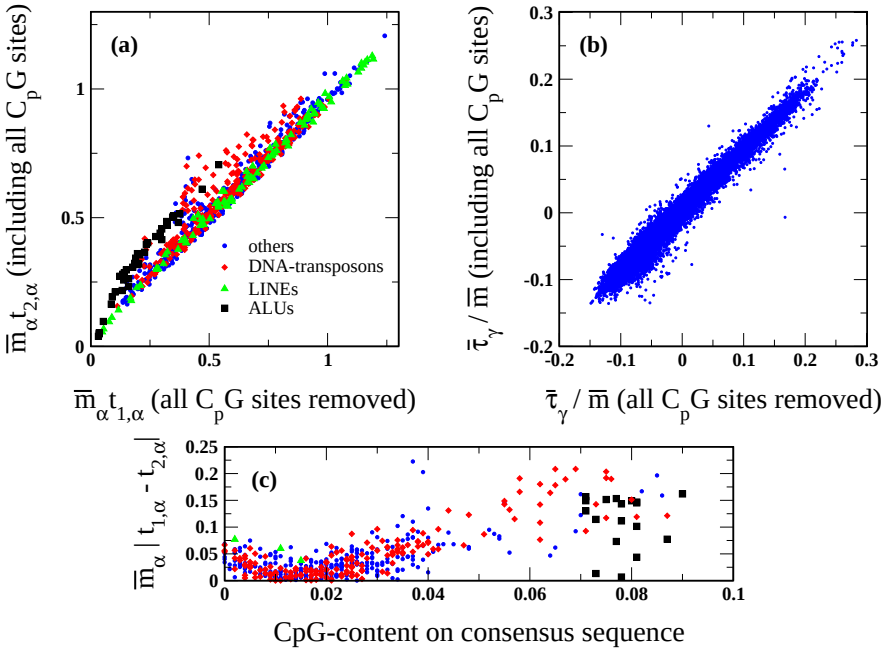

Figure 6.4: The effect of an enhanced C_pG transition rate (b) on the local substitution rate $\overline{\tau}_\gamma/\overline{m}$ for the human genome, and (a) on the estimation of age t_α $\overline{m}_\alpha$ of repeat-family α. The values on the y-axis shows the original output using the full sequence, whereas the quantities on the x-axis showing the same quantity, but now computed with consensus sequences where all C_pG sites are removed. Three major types of the repetitive elements, ALUs (black squares), LINEs (red diamonds), and DNA-transposons (green triangles) are distinguished in (a). An error estimate allowing to assess the impact of the elevated C_pG decay is graphed against the C_pG content of the consensus is shown in (c). Again, the three types of repetitive elements are distinguished for this graph.

sites from the consensus sequence, $t_\alpha\overline{m}_\alpha$ and $\overline{\tau}_\gamma/\overline{m}$ are estimated and compared with the results where all C_pG site are still present. The results are shown in Fig. 6.4a for $t_\alpha\overline{m}_\alpha$ and in in Fig. 6.4b for $\overline{\tau}_\gamma/\overline{m}$. As expected the estimated of $\overline{\tau}_\gamma/\overline{m}$ are highly correlated, having a correlation coefficient of $r = 0.98$. The primary effect of neglecting the C_pG-specific transitions is introducing noise to the data. Our previous results showed that the values on the x-axis of Fig. 6.4a should be pretty close to the true age of the repeats families while values on the y-axis suffer from the C_pG effect. Considering the three major repeat types, ALUs (black squares), LINEs (green triangles), and DNA-transposons (red diamonds) we observe that the age of the ALUs tend to be overestimated, while estimates based on LINEs are fairly accurate. In Fig. 6.4c the error of ignoring the hypermutability of the C_pG sites is plotted with respect to the C_pG content of the consensus sequence for each repeat-family. The error is measured by the modulus of the difference between the age estimates having the C_pG sites removed and not. According to the numerical analysis, this graph shows a high error for most of the repeats having a high C_pG content in its consensus sequence. At a C_pG content of about 0.015, Fig. 6.4c has a minimum. However, this minimum might be explained by the fact that the six-parameter model is calibrated to gain the best description of the data. Thus, $t_\alpha\overline{m}_\alpha$ for repeat families with the lowest C_pG content are slightly biased as

well. Since the genome-wide estimation of time $t_\alpha \overline{m}_\alpha$ is inaccurate for some repeat families, the partition-wide estimation $x_{\alpha\gamma}$ is likely to suffer from the same deficiency. Because $\overline{\tau}_\gamma / \overline{m}$ is the ratio of quantities having the same source of inaccuracy, the errors will tend to cancel.

Hence, the use of the six parameter model can be justified by the statements given above. The effect of ignoring higher C_pG substitution rates are mostly absorbed in the rate matrix q, thus these values might be considered as effective rates. Further, we find that a pre-processing step of removing C_pG sites is justified and will improve results if the loss of data points can be tolerated. Additionally, the use of the seven-parameter model as done in [153, 163, 164, 141] is not recommended due to the following criticism: first, a massive lost in resolution has to be taken into account since 64 dimensional probability distributions have to be considered. This strongly affects the noise reduction process since the smallest feasible resolution to obtain reliable results is around 1 Mb. Second, when a GC dinucleotide is formed, its methylation is not obligatory and might also be different throughout the entire population. However, the methylation state of the DNA and its evolution is not accessible by the sequence data itself. A more realistic model incorporating the methylation of the DNA is therefore situated somewhere between the six and the seven-parameter model.

6.6. Results for the Age of the Repeats $t_\alpha \overline{m}_\alpha$ and the Transition Matrix q

The presented model is applied to sequence data of human, mouse, rat, chimpanzee and dog, allowing inter-species comparisons of the derived quantities. Looking at the time span of the repeat families $t_\alpha \overline{m}_\alpha$, values between 0 and roughly 1.1 are obtained, where the scaled time 1.1 corresponds to the oldest available set of repeats. For a subset of these repeats our estimates for the age are compared with those computed by Khan et al. [165], as shown in Figure 6.5. This comparison yields that a linear relationship within the interval $t_\alpha \ \overline{m}_\alpha \in [0, 0.6]$ holds, from which may be concluded that $\overline{m}_\alpha = \frac{1}{t_\alpha} \int_{-t_\alpha}^{0} m(t)\ dt$ is approximately constant in time. Thus, $\overline{m}_\alpha \approx \overline{m}$, where the actual value of $\overline{m}$ can be extracted from the slope of the straight line in Fig. 6.5 and yields $\overline{m} = 6.5 \times 10^{-3}$/Myr. However, the time independence of $\overline{m}$ is only confirmed for the last 90 Myr and for the human genome. Later it will be shown that a significant acceleration of the total substitution rate took place for the rodent lineage after its speciation from the human lineage. It is therefore convenient to use our scaled units. Only if needed a conversion to the physical time is proceeded. However, if we assume that the total substitution rate is constant for the whole observed time period and for the human genome, the age oldest repeat family is roughly 170 Myr.

Figure 6.6 summarizes the results of our multidimensional data fitting procedure when applied to the human genome. It shows the $16 \cdot M$ data points of the matrices Q_α for the entire genome. Each matrix Q_α can be related to the scaled time $t_\alpha \ \overline{m}_\alpha$, allowing to display the time dependence of the 16 components of Q_α. Each graph in Fig. 6.6 corresponds to one of the 16 components of Q_α and thus to a specific type of transition. Let us start the discussion with the diagonal elements. Note that a $i \to i$ transition can be interpreted in the following way:

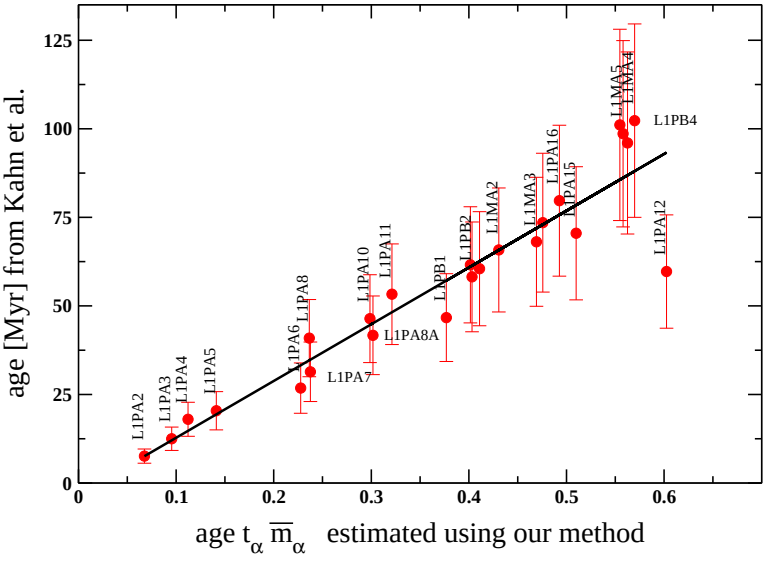

Figure 6.5: The estimate of the age for some transposable elements of the LINE type. For this specific type the largest overlapping set of the age estimates obtained by Khan et al. [165] is compared with the derived age using the presented method. As shown by the black line, a linear relationship holds between both estimates. Additionally, this relation provides a conversion of our scaled units to the physical time within the observed range.

either the probability that base i has not changed at all, or that it has changed but substituted back to its original base. All diagonal entries must have a value of one at $t_\alpha \overline{m}_\alpha = 0$. For $t_\alpha \overline{m}_\alpha = 1$, both the $A \to A$ and the $T \to T$ transition are having a probability of about 0.8, while for $C \to C$ and $G \to G$ one obtains roughly 0.6. Therefore, with a probability of 80% an A or T in the ancestor sequence about 160 million years ago is still A or T in today's genome. However, for G and C bases this probability is only 60%. Analyzing the first row of the Fig. 6.6 reveals that from remaining probability of 20% base A has experienced a transition to C with a probability of 5%, to G with 10%, and to T with a probability of 5% at time $t_\alpha \overline{m}_\alpha = 1$. The remaining rows of the figure can be interpreted accordingly. Note that transitions (green lines) have much larger substitution probabilities than transversions (red lines). In addition, the assumed strand-symmetry is visible by complementary substitutions, e.g., $A \to G$ like $T \to C$, having the same probabilities. In total, Fig. 6.6 illustrates the quality of the fitting procedure and can be regarded as a first indication that the four-state neighbor-independent substitution model, Eq. (6.10), seems to adequately capture the main features of the data.

Returning to the rate matrix q, the six rate constants $q_1, \cdots, q_6$ are calculated for the following species: human (hg18), mouse (mm8), chimpanzee (pt2), rat (rn3), and dog (cf2). Note that the used abbreviation of the species, e.g., hg18 for human, relates to current builds obtained from the UCSC genome browser [166]. An overview of the rates is given in Tab. 6.3 and reveals that there are almost no variations between the four transversion substitution rates, $q_1, \cdots, q_4$ within and between the species. However, the transition substitution rate

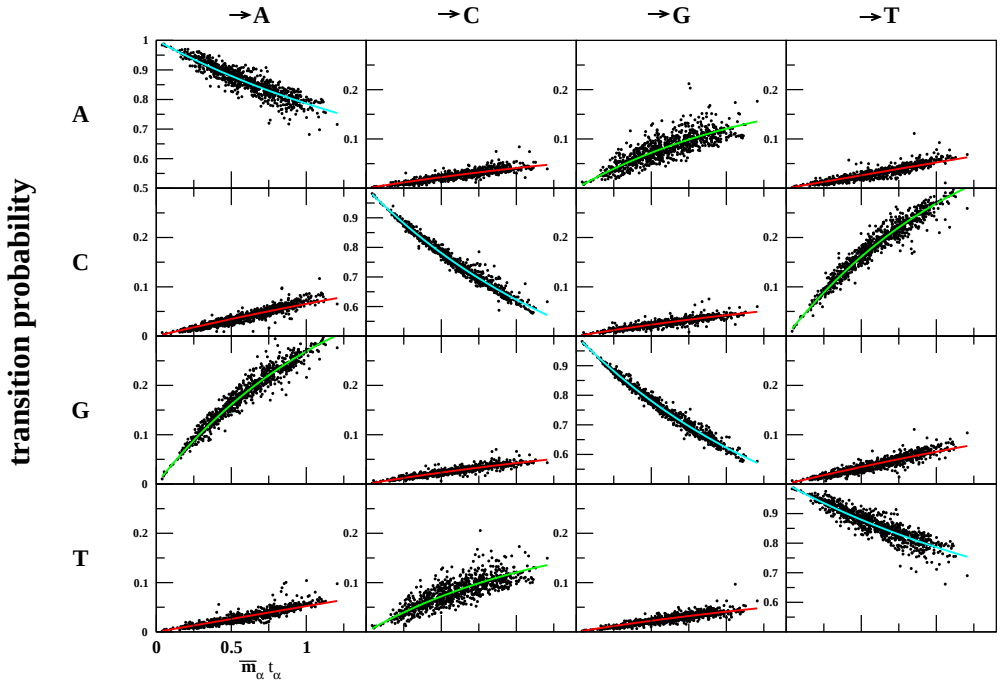

Figure 6.6: Substitution probabilities for each repeat family of the human genome and all possible state transitions. All probabilities are genome-wide averaged ($Z = 1$). The data points are representing the components of the matrices Q_α versus the age $t_\alpha \overline{m}_\alpha$. Model fits using Eq. (6.10) are shown by the solid lines, where the transversion substitutions are represented by the red line and the transition substitutions by the green line.

is about a factor of three larger than the average transversion rate but is again almost identical for all five species. Larger differences are observable for q_6, which varies between 0.31 and 0.39. As explained in Sec. 6.5, the C_pG-specific transitions are absorbed into rate q_6. In fact, this rate is substantially higher than the others which is mostly due to the described hypermutability of the C_pG sites. However, differences in q_6 for mouse/rat and chimp/human are probably due to a different overall C_pG content, e.g., 0.94 % on the human

rate	transition	hg18	mm8	pt2	rn3	cf2
q_1	$A \to C$ and $T \to G$	0.05	0.05	0.05	0.05	0.05
q_2	$A \to T$ and $T \to A$	0.05	0.05	0.05	0.04	0.05
q_3	$C \to G$ and $G \to C$	0.05	0.05	0.05	0.05	0.05
q_4	$C \to A$ and $G \to T$	0.07	0.07	0.07	0.06	0.06
q_5	$A \to G$ and $T \to C$	0.17	0.16	0.17	0.16	0.16
q_6	$G \to A$ and $C \to T$	0.39	0.32	0.39	0.31	0.34

Table 6.3: Comparison of the six transition rates $q_1, \cdots, q_6$, where the analysis is based on the genomes of human (hg18), mouse (mm8), chimpanzee (pt2), rat (rn3), and dog (cf2). All abbreviations are consistent with the used genome builds obtained from the UCSC genome browser [166].

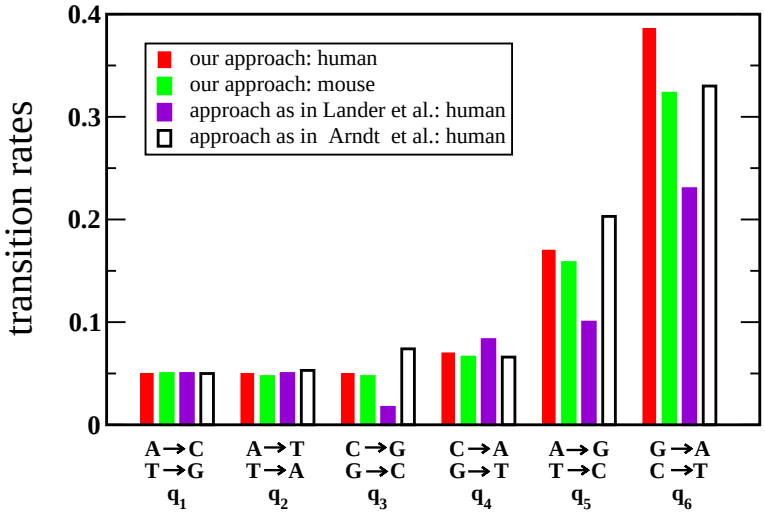

Figure 6.7: The estimated relative substitution rates for each of the six substitutions. A comparison of the result obtained by Lander et al. [137], by the Arndt et al., and the proposed method is shown. Apart from slight deviations, the predictions are leading to a similar conclusion with respect to relative transversion and transition substitution rates. In order to obtain a meaningful comparison, all predictions are scaled to possess an equal rate q_1.

and 0.83 % on the mouse genome. In Sec. 6.8, this issue is discussed in detail since it plays an important rôle for the equilibrium GC content of the genome. Despite the small C_pG induced differences in q_6 the rates for the five species are showing a remarkable agreement; pointing to a fundamental process of substitution, at least for mammals. Besides the presented estimates for the substitution rates, other estimates have been discussed in the literature. These are the rates obtained by Arndt et al. [163] or Lander et al. [137]. In Fig. 6.7 these values are compared with our estimates, whereas the rates where scaled such that q_1 possesses the same value for each estimate. The largest deviations occur in the rates obtained by Lander et al. with respect to the others. However, the results of Arndt et al. and ours are fairly close together. But the picture that transitions occur about three times higher than transversions does not change. Unfortunately, other rate estimates for other species than the human are not available in the literature.

Returning to the age of the repeats, the estimates of t_α $\overline{m}_\alpha$ for the human genome is compared with the corresponding values calculated for another species. This is possible since many repeat families were introduced into the genome before the speciation of both species, i.e., the time where two lineages separated, thus having homologous copies on the genomes. Let t_s designate the speciation time of two species, and define ancestral repeats as those repeats having an age $t_\alpha > t_s$, they hence were inserted at a time before $-t_s$. The age estimates for these ancestral repeats common to the mouse and human genome are shown in Fig. 6.8a. This process is repeated to obtain the same data for chimpanzee versus human, dog versus human, and for rat versus human. To avoid undue scattering of the data we use only ancestral families that have accumulated a total length of least 100 kb on both genomes.

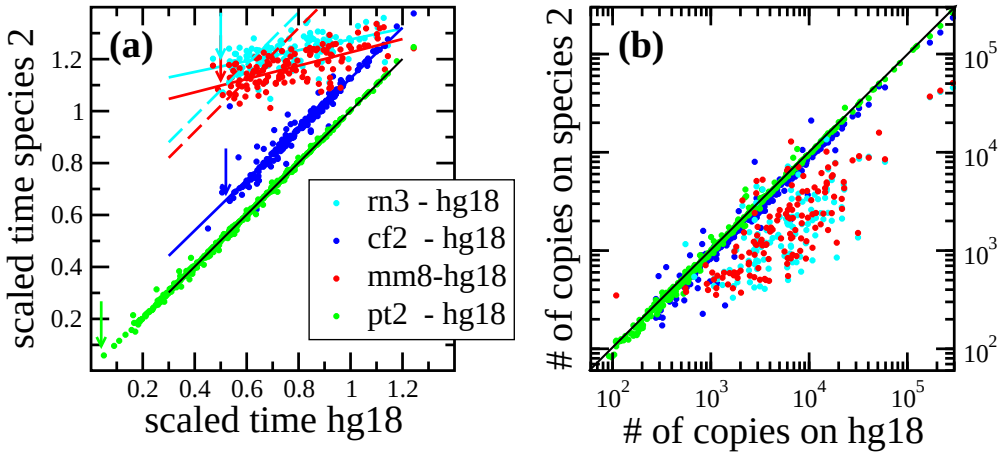

Figure 6.8: Inter-species comparison of the age of ancestral repeats. (a) Shown is the age of ancient repeats common to the genomes of mouse and human (red dots), chimp/human (green dots), dog/human (blue dots) and rat/human (turquoise dots). This is realized by plotting $t_\alpha \overline{m}^\alpha_{\text{species2}}$ on the y-axis versus $t_\alpha \overline{m}^\alpha_{hg}$ of the human genome on the x-axis. Arrows mark the speciation time with reference to the scaled time relating to the human genome. Dashed lines are regressions, where a slope of one is fixed as explained on p. 95. Same repeat families and species as in (a) are shown in (b), but now the total number of repeat copies on each genome is correlated.

Since the repeats were inserted before the speciation of the species a straight line is expected, which can accordingly be found in Fig. 6.8a, solid lines. The slope a and the intercept b can be determined using a least-squares fit to the data:

			a	b				a	b	
pt2	**vs.**	**hg18** :	0.999	0.002	**mm8**	**vs.**	**hg18** :	0.256	0.97	(6.18)
cf2	**vs.**	**hg18** :	0.976	0.15	**rn3**	**vs.**	**hg18** :	0.209	1.07	.

A sharp edge on a line parallel to the y-axis is visible from which we can roughly estimate the speciation time for each pair of species. From the age of the youngest common repeat we find four speciation times $\overline{m}^{t_s}_{hg} t_s$ indicated by arrows in the Fig. 6.8a. Because the speciation times using the scaled units are below 0.6, they can safely be related to the physical time using $\overline{m} = 6.5 \times 10^{-3}$/Myr, as discussed on p. 90. We obtain

pt2	**vs.**	**hg18** :	0.04	$\rightarrow$ 6 Myr	**mm8**	**vs.**	**hg18** :	0.5	$\rightarrow$ 77 Myr	
cf2	**vs.**	**hg18** :	0.52	$\rightarrow$ 80 Myr	**rn3**	**vs.**	**hg18** :	0.5	$\rightarrow$ 77 Myr	. (6.19)

Note that the speciation time of rat and mouse with respect to the human lineage must be equal because the separation of these species occurred significantly after the speciation with the human lineage.

Let us now consider the linear relationship we observe in Fig. 6.8a. Next, it is mathematically shown that the slope of these straight lines must be equal to one. This is fairly the case for the chimpanzee and the dog. However, this is not the case for the rat and the mouse. Further below, possible explanations are given after the slope-one condition has been derived.

In order to simplify the notation the following analysis is performed for the mouse and human genomes, but we also could have used any other pair of species. Recalling Eq. (6.3) from Sec. 6.2, let us rewrite this equation by the slightly more general expression:

$$Q(t_1, t_2) = \exp\left(\mathbf{q} \int_{-t_1}^{-t_2} m(t')\ dt'\right), \tag{6.20}$$

where Eq. (6.4) is already inserted. The only difference between the latter expression and Eq. (6.3) is that the endpoint of the used time period is arbitrary rather than zero (present). In general, for mouse and the human genome $Q_m(t_1, t_2)$ is not equal to $Q_{hg}(t_1, t_2)$, where the subscript indicates the species for which the quantity is calculated. It is known, e.g., that the total substitution rate is substantially larger on the mouse genome than the human [167]. However, the reason for that is currently unclear. But if the time points t_1 and t_2 are chosen to lie before the speciation time t_s then both expressions reflect rates on the common ancestor and hence must be equal. The only assumption here is the existence of a common ancestor, thus the basis of the entire theory of evolution. Let $-t < -t_s$ we therefore have

$$Q_m(t, t_s) = Q_{hg}(t, t_s)\ . \tag{6.21}$$

Again, the matrix q is identical for the common ancestor and since the exponential is a one-to-one map, we can infer using Eq. (6.20) and Eq. (6.21) that

$$\int_{-t}^{-t_s} m_m(t')\ dt' = \int_{-t}^{-t_s} m_{hg}(t')\ dt'\ , \tag{6.22}$$

where $m_m(t')$, $m_{hg}(t')$ is the total substitution rate of the mouse, human genome at time t'. Rewriting the integrals in Eq. (6.22) yields

$$\overline{m}_m^t t - \overline{m}_m^{t_s} t_s \quad = \quad \overline{m}_{hg}^t t - \overline{m}_{hg}^{t_s} t_s \tag{6.23}$$

where the super-index at the overline symbol indicates that the average over the period $(-t, 0)$ and $(-t_s, 0)$ is taken. Hence, as long as $-t < -t_s$ we obtain

$$\overline{m}_m^t t = b + \overline{m}_{hg}^t t \tag{6.24}$$

with the constant given by

$$b = \overline{m}_m^{t_s} t_s - \overline{m}_{hg}^{t_s} t_s\ . \tag{6.25}$$

In fact, the presented method provides us with the scaled age $\overline{m}^{t_\alpha} t_\alpha$ of repeat family α. Correlating these ages for two species, as done in Fig. 6.8a yields a linear curve with slope one. Note that the condition $-t_\alpha < -t_s$ is automatically satisfied because repetitive elements before the speciation of the species differ and can therefore not be correlated. Moreover, it should be stressed that the slope-one condition is the consequence of the fact that a common ancestor can have only one substitution rate.

As already mentioned, the slope-one condition is realized for both chimpanzee and dog but is violated for the rat and mouse genome. Here, the slope is a factor 4 to 5 smaller

than expected. Interestingly, if the age of ancient repeats common to mouse and rat are correlated, then one again obtains a regression line with slope-one (data not shown). The naïve conclusion would, e.g., be that a common ancestor of human and rodents did not exist at least for the age interval $(0.5, 1.1)$, yielding that the mouse/human and rat/human speciation time given in (6.19) are artefacts. However, this again is difficult to reconcile with the fact that both genomes have a large number of repeats in common and that the estimate of the speciation time is compatible with other estimates based on different methods, e.g., [138] and [139] estimated 75 Myr as speciation time. A possible, more realistic explanation is that the age of ancient repeat families on the mouse and rat genome is grossly underestimated. It is evident from Figure 6.8a that the age of mouse and rat repeats are close to the border of what can be identified using the RepeatMasker. Repeat families of a age greater than 1.3 have generally undergone too many substitutions to be correctly identified by RepeatMasker. Let us consider a repeat family with copies having a broad time-distribution with a peak at a time much larger than 1.3. A large fraction of copies of this family cannot be found, and those copies that are actually found will certainly belong to just one tail of this distribution. Thus, the RepeatMasker provides us with a truncated set of repeats comprising copies that are much younger than the true family average. Consequently, this truncation leads to a severe underestimation of the age for these repeat families. A possible way to approach this hypothesis is by counting the number of copies of a repeat-family on both genomes which should be close to each other if indeed the repeat-family was copied into the genome of the common ancestor. This is shown in Fig. 6.8b, where we observe that the number of copies of the common repeats on the mouse and rate genome is in fact an order of magnitude smaller than on the human genome. One should keep in mind that the genomes of mouse and rat are about half as long as the human genome. Still, Fig. 6.8b seems to suggest that our explanation might be true and that the estimated scaled times suffer from an artifacts produced by the RepeatMasker software which is not capable of delivering really the complete set of each repeat family on the mouse and rat genome.

If we enforce the slope-one condition in Fig. 6.8a for mouse and rat, the ratio of the average total substitution rate to the reference species can roughly estimated for mouse and rat. However, the same estimate for dog and chimpanzee is quite accurate. The dashed lines in Fig. 6.8a are showing again the linear relationship for the mouse and rat data in the region $\overline{m}^{\alpha}_{hg} t_\alpha < 0.7$ where now the slope of the line is forced to one. The intercept values b in Eq. (6.18) then change to

$$\begin{array}{llll} & & b & \\ \textbf{pt2} \ \textbf{vs.} \ \textbf{hg18}: & 0.002 & \textbf{mm8} \ \textbf{vs.} \ \textbf{hg18}: & 0.52 \\ \textbf{cf2} \ \textbf{vs.} \ \textbf{hg18}: & 0.15 & \textbf{rn3} \ \textbf{vs.} \ \textbf{hg18}: & 0.58 \ . \end{array} \qquad (6.26)$$

By Eq. (6.24) these values are equal to the constant b in Eq. (6.24) and (6.25). Rearranging the latter expression yields

$$\frac{\overline{m}^{t_s}_{\text{species2}}}{\overline{m}^{t_s}_{hg}} = \frac{b}{\overline{m}^{t_s}_{hg} t_s} + 1 \ . \qquad (6.27)$$

Using the speciation times listed in (6.19) and the intercepts shown in (6.26), estimates of

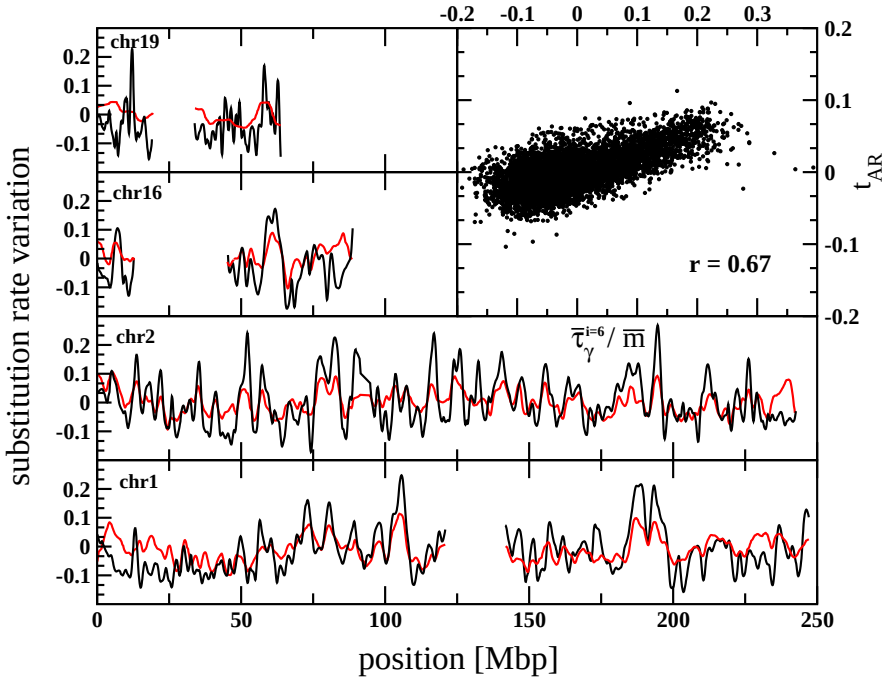

Figure 6.9: In this figure $\overline{\tau}_{\gamma}^{i=6}/\overline{m}$ relating to age-class C_6 (black curve) and filtered t_{AR} (red curve) is shown for four sample chromosomes of the human genome. Breaks in the curves correspond to centromeric regions, highly structured with an extremely low density of the used interspersed repeats. The inset box depicts a whole genome regression of the two aforementioned quantities, resulting in a linear correlation coefficient of $r = 0.67$.

the ratio $\overline{m}^{t_s}_{\mathrm{species2}}/\overline{m}^{t_s}_{hg}$ can therefore be determined from Eq. (6.27):

$$\begin{array}{llllllll} \textbf{pt2} & \textbf{vs.} & \textbf{hg18}: & 1.05 & \textbf{mm8} & \textbf{vs.} & \textbf{hg18}: & 2.04 \\ \textbf{cf2} & \textbf{vs.} & \textbf{hg18}: & 1.29 & \textbf{rn3} & \textbf{vs.} & \textbf{hg18}: & 2.16 \quad . \end{array} \tag{6.28}$$

We can conclude that the averaged total substitution rate over the time period $(-t_s, 0)$ of the mouse and rat is 2 times larger than for the human genome. Moreover, it differs only by a factor of 1.3 for the dog and the chimpanzee has nearly the same averaged total substitution rate than the human.

6.7. Validation of the Model

In this section, the obtained results using the model described in Sec. 6.2 are validated under three different aspects: first, $\overline{\tau}_{\gamma}/\overline{m}$ is compared with another estimate discussed in the literature. Second, a simulation study is performed to check the consistency of the method, and third, two disjointed sets are formed out of the repeat families and $\overline{\tau}_{\gamma}/\overline{m}$ is estimated for both sets. A comparison of those values is done to show the independence of the method with respect to the used repeat families. Let us start by comparing our results to the t_{AR}

statistic described in [142]. The results are shown in Fig. 6.9. After normalizing t_{AR} to reflect variation and applying the same noise filtering technique, Sec. 6.4, a close correlation between the two estimates are found, having a correlation coefficient of $r = 0.67$. In addition, spatially resolved estimates of $\overline{\tau}_{\gamma}^{i=6}/\overline{m}$ (black lines) and the normalized t_{AR} estimates (red lines) are exemplarily shown for chromosome 1, 2, 16, and 22 in Fig. 6.9. It seems that the t_{AR} values are mostly smeared out with respect to $\overline{\tau}_{\gamma}^{i=6}/\overline{m}$. Since, t_{AR} is based on a human/mouse comparison of interspersed repeats, the estimate therefore suffers from inter-species convolutions of multiple species substitution rates. This aspect will be discussed in detail, when the conservation of the substitution rate pattern is addressed in Sec. 6.8.

The second method of verification is a consistency check by a simulation study. To realize this verification, a simulation procedure is developed that accounts for location-varying substitution rates and repeat family insertions. Applying this tool allows us to compare the estimated parameters with the known values. Furthermore, this also allows us to assess the error for the whole procedure. Starting with a random genomic sequence and subjecting it to a series of substitution using pre-specified rates results in a final sequence which is then analyzed using the proposed method. In the formulation of the used model several simplifying assumptions are made, as discussed in Sec. 6.2. This simulation does not validate these assumptions. It rather validates the mathematics based on these assumptions and shows that if the assumptions are true, our estimations are accurate. Questions concerning the validity of these assumptions with respect to mammalian genomes, and the tolerance of the model to deviations from this assumptions, are discussed in Secs. 6.5, and 6.6. The main quantity which needs to be defined is the time dependent local substitution rate

$$m_{\mu}(t) = m(t) + \tau_{\mu} \tag{6.29}$$

where t denotes time, μ represents a base position (running from 1 to N) and $m(t)$ is the genome-wide average of $m_{\mu}(t)$.

The simulated genome is just a sequence of bases, here represented by the genome status array b_{μ} which can take one of the four values $\{1, 2, 3, 4\}$, again corresponding to $A\hat{=}1$, $C\hat{=}2$, $G\hat{=}3$, and $T\hat{=}4$. Initially, $N_0 = 16 \times 10^6$ and the b_{μ}'s are randomly chosen from a uniform distribution. Furthermore the components $p_i(t)$ of the row-vector $p(t)$ are required which specifies the probability of observing one of the four nucleotide basis at a certain site and time t. The whole simulation scheme is based on Eq. (6.1) on page 78,

$$\frac{d}{dt}p_j(t) = \sum_{i=1}^{4} p_i(t) m_{\mu}(t)\ q_{ij}\ . \tag{6.30}$$

Applying the Euler method to obtain an update step Δp_j for each time step Δt and after inserting Eq. (6.29), we obtain

$$\Delta p_j = m(t)\Delta t\ \Big(1 + \tau_{\mu}/m(t)\Big)\ \sum_i p_i\ q_{ij}\ . \tag{6.31}$$

Similar to the simulation of a stochastic differential equation the Euler method is sufficient for this simulation [168]. To simplify the notation scaled times are introduced

$$t^* = m(t)t \quad \text{and} \quad \Delta t^* = m(t)\Delta t\ . \tag{6.32}$$

As usual, $t^* = 0$ refers to the present, while $t^* = -1$ lies in the past and is the largest time we used in our simulation. Thus, the simulated evolution of the synthetic genome starts at $t^* = -1$ and moves towards $t^* = 0$. In principle, time increment Δt^* could be itself a function of t^* if one wishes to include the effect of a variation in $m(t)$. For simplicity a constant global mutation rate $m(t) = m$ is chosen, with a time increment of $\Delta t^* = 5 \times 10^{-3}$. Thus, Eq. (6.31) becomes

$$\Delta p_j = \Delta t^* \left(1 + \tau_\mu / m\right) \sum_i p_i \; q_{ij} \; . \tag{6.33}$$

The simulation now consists of stepping from time -1 to time 0 in increments of Δt^*, inducing base substitutions in each step as follows:

1. Denote the value of genome status array $b_\mu(t^*)$ at position μ by i'.
2. For each $i \in \{1, 2, 3, 4\}$ let $p_i(t^*) = \delta_{i,i'}$.
3. Where for each $j \in \{1, 2, 3, 4\}$ the probability $\Delta p_j(t^*)$ is calculated using Eq. (6.33).
4. For each $i \in \{1, 2, 3, 4\}$ let $p_i(t^* + \Delta t^*) = \delta_{i,i'} + \Delta p_i(t^*)$.
5. Randomly draw the new value for $b_\mu(t^* + \Delta t^*)$ from the set $\{1, 2, 3, 4\}$ using the new probability distribution $\{p_1, p_2, p_3, p_4\}$ at $t^* + \Delta t^*$.

In addition to the simulation of base substitution, random insertion of repeat families into the simulated genome are needed. Moreover, to allow the application of RepeatMasker for the simulation study, 817 repeat consensus sequences from the RepBase [152] are used as potential insertion sequences. At each instance of time new families are inserted whereas the members are randomly chosen from the potential candidates and inserted into the simulated genome at a number of randomly determined locations. By construction, the possibility that a given family member is inserted into an existing copy the same family is not allowed. But it is possible that a repeat family is inserted into a copy of a distinct family. The synthetic genome is divided into 20 chromosomes. Ten new repeat families are inserted into every chromosome starting at time $t^* = -1$, and after every interval of 0.1 time units. The process of insertion is performed by the following steps:

1. Randomly choose a repeat family from the RepBase database. Multiple draws of the same family are not permitted. Each family is copied into every chromosome.
2. For each chromosome, randomly pick a value N_c out of $10 \leq N_c \leq 170$ designating this number to the amount copies for the family to be inserted.
3. Randomly select N_c different insertion sites for each chromosome using a uniform distribution.

Therefore, 10 different families at 10 insertion times are used, resulting in an increase of every chromosome from 16 Mbp to 30 Mbp. Thereby, approximately 50% of the bases in the final

Rate	Transition	actual	estimation
q_1	$A \to C$ and $T \to G$	0.05	0.05 (fixed)
q_2	$A \to T$ and $T \to A$	0.05	0.05±0.01
q_3	$C \to G$ and $G \to C$	0.05	0.05±0.01
q_4	$C \to A$ and $G \to T$	0.05	0.05±0.01
q_5	$A \to G$ and $T \to C$	0.15	0.16±0.02
q_6	$G \to A$ and $C \to T$	0.15	0.17±0.01

Table 6.4: Results on the consistency of model and simulation. The third column shows the actual transition rates used in the simulation, where the corresponding estimates are given in column four. Due the fluctuations introduced by the RepeatMasker the rate estimates are not perfectly reproduced, but an estimation error is visible. Nevertheless, the estimated rates are compatible with the actual values.

simulated genome are part of interspersed repeats. Next, let us specify the substitution rate pattern τ_μ by

$$\tau_\mu = A_0 \ \sin\left(\frac{8\pi\mu}{N}\right) \qquad \text{for} \qquad \mu = 1, \cdots, N \ . \tag{6.34}$$

After every insertion of new repeats into the genome, the array τ_μ is updated to assign values for τ_μ to those sites μ that have newly entered the genome. This was done as follows: If a repeat was copied between location μ' and μ'', then τ_μ for all newly created sites between μ' and μ'' was computed from a linear interpolation between $\tau_{\mu'}$ and $\tau_{\mu''}$. This procedure reflects our central finding that substitution rates depends on the sequence context.

The outcome of the simulations is analyzed by the RepeatMasker, whose output is then subject to the proposed computational method. As explained in Sec. 6.2, the method estimates the age t^*_α for every repeat family, the q-matrix, and most importantly, the local substitution rate $\overline{\tau}_{\alpha\gamma}/m$ in partition γ ($\gamma = 1, \cdots, Z$). All these quantities are compared in the following with the original values that are used as input for the simulation. Table 6.4 summarizes our results for the q-matrix. Here, we observe that all rates are well reproduced. Next, let us consider the estimated age of all repeats copied into the genome. The actual age of a repeat family is determined by the time when it was inserted into the genome. In Fig. 6.10 the estimated age is shown on the y-axis versus its actual age on the x-axis. As mentioned above, 100 different repeat families are copied into the genome, but almost 240 different families are identified by the RepeatMasker. This discrepancy is a result of the insertion of repeats within other repeat families, decreasing the chance that RepeatMasker to find the correct repeat family to the resulting fragments. As it can be seen in Fig. 6.10 the age estimates are fairly accurate for younger repeats, but the scattering increases with age. Additionally, the age of older repeats tend to be underestimated. This effect is probably similar to the underestimation in age for the rodent lineage, as discussed in Sec. 6.6. Moreover, it should be remarked that the time estimation for the real genome data are based on much more mutations. Here, we considered a genome having 600 Mbp while the human genome consists of about 3000 Mbp. It is also noted that a systematic error in the estimation of t_α will also lead to a similar error in $x_{\alpha\gamma} = \overline{\tau}_{\alpha\gamma} + t_\alpha m$. For the estimation of $\overline{\tau}_{\alpha\gamma}$ this quantity is

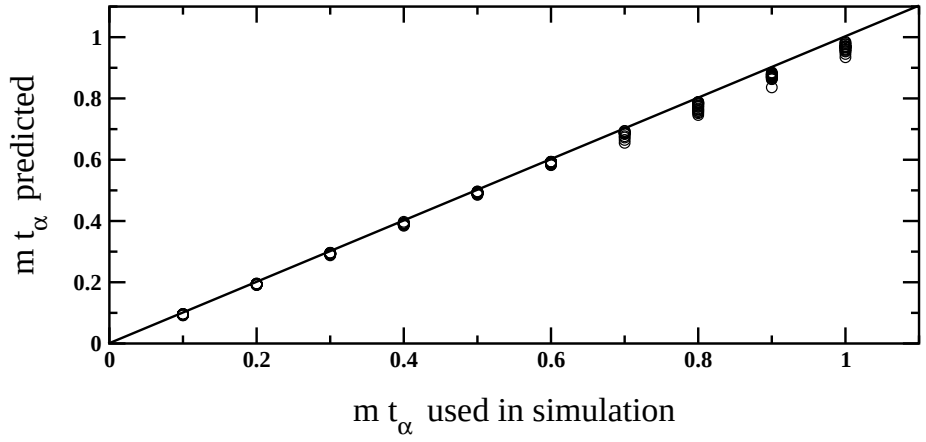

Figure 6.10: Age t_α of repeat family α as estimated by the method (y-axis) versus the true age as used in the simulation (x-axis). The solid line shows the bisecting line allowing to assess derivations originating from the entire estimation procedure. Here, the age of the youngest repeats are accurately estimated, where the age of old repeats tend to be slightly underestimated. This is similar to the derivations from the slope one condition of the rodent lineage, as discussed in Sec. 6.6.

again divided in Eq. (6.11) by t_α. Thus, errors in t_α will partly cancel in the determination of $\overline{\tau}_{\alpha\gamma}$. To check the accuracy of the estimated substitution rate, let us divide the the used time span into ten time slots, $\beta = 1, \cdots, 10$, centered at $t^*_\beta = 0.1, 0.2, \cdots, 1$. Take all N_β repeats having t^*_α within slot β as a basis for predicting the substitution rate pattern for the

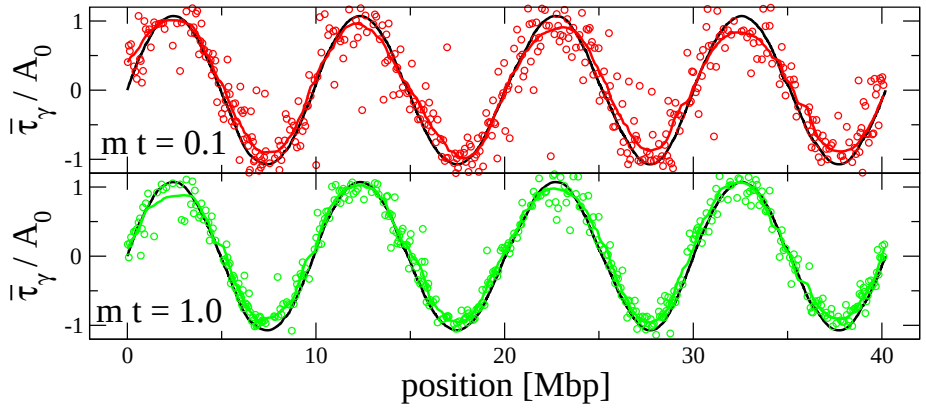

Figure 6.11: The local substitution rate as a function of the position on the simulated genome. Black lines are showing the substitution rate τ_μ/A_0 that has been used in the simulation. The green and red symbols are representing $\overline{\tau}_\gamma/A_0$ the estimated pattern using the proposed method. Here, repeat families belonging to the age class of the youngest repeats $t^*_\beta = 0.1$ (red symbols, upper panel) and of the oldest repeats $t^*_\beta = 1.0$ (green symbols, lower panel) are considered. Solid lines are showing the smoothed curves obtained from filtering procedure. A great accordance of the noise filtered curve and the underlying substitution rate pattern is visible.

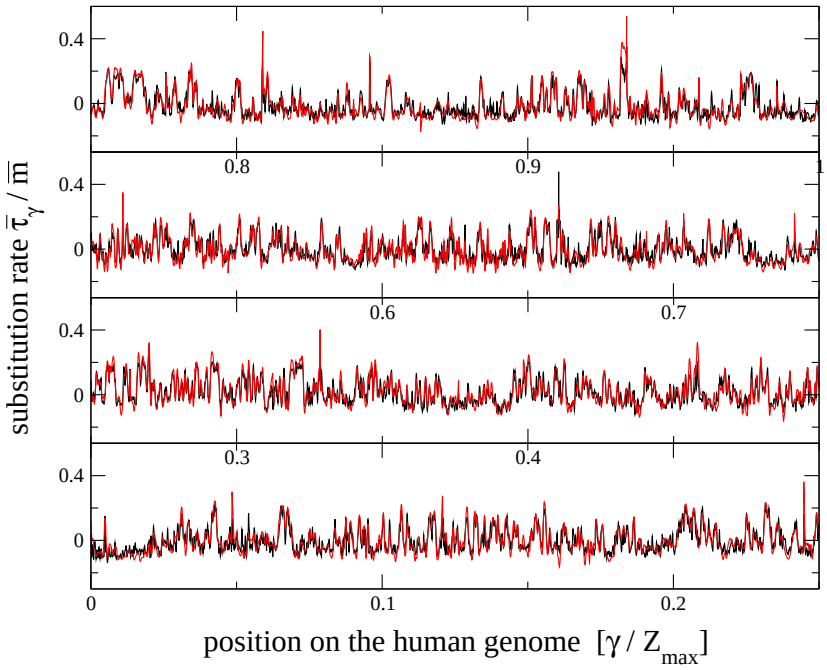

Figure 6.12: Computation of $\overline{\tau}_\gamma/\overline{m}$ using disjoint repeat family sets. Shown is $\overline{\tau}_\gamma/\overline{m}$ against partition position using two disjoint sets of data: repeat families with $\sigma_\alpha/\overline{m}_\alpha \leq 0.24$ (black curve, calculated from 407 repeat families), and repeat families with $\sigma_\alpha/\overline{m}_\alpha > 0.24$ (red curve, also calculated from 407 repeat families). A regression between these two data result in a correlation coefficient of $r = 0.895$.

corresponding time-window. Thus, we have

$$\tau^*_{\gamma,\beta} = \frac{1}{N_\beta} \sum_{\alpha \in \beta} \frac{\tau_\gamma}{m} \, . \tag{6.35}$$

Figure 6.11 shows $\tau^*_{\gamma,\beta}/A_0$ obtained for the age class consisting of the youngest ($t^*_\beta = -0.1$) and of the oldest repeats ($t^*_\beta = -1.0$) respectively. Here, the real underlying input function τ_μ/A_0 defined in Eq. (6.34) is compared with the estimates $\tau^*_{\gamma,\beta}/A_0$. Noise-filtered curves (solid lines) are also shown. These curves are showing a good accordance with the underlying substitution pattern. Furthermore, it verifies that the noise produced by the RepeatMasker is successfully filtered out by the proposed noise reduction procedure, which shows the consistency of the proposed method.

In Section 6.2 a model for the repeat families was suggested based on the short-burst approximation, which in consequence leads to the possibility that the age distribution can be grouped into a phylogenetic tree. However, the following results demonstrate that the model can cope with deviations from this model. This can be accomplished by separating the entire set of repeat families into disjoint subsets of having either a low or a high standard deviation $\sigma_\alpha/\overline{m}_\alpha$ of $\overline{\tau}_\gamma/\overline{m}_\alpha$. Imagine that repeat family α_1 has a significantly broader age distribution than α_2 but both are having approximately the same average age. Then, the age of repeat family α_1 scatters heavier between the partitions than that of family α_2. This enters into

Eq. (6.11) such that $\sigma_\alpha/\overline{m}_\alpha$ fluctuates stronger for α_1 than for α_2. Hence, the aforementioned separation is useful to study effects originating from the possibility of having repeats with a considerable age distribution. Figure 6.12 illustrates this by breaking into repeat families satisfying $\sigma_\alpha/\overline{m}_\alpha \leq 0.24$ (black curve) and $\sigma_\alpha/\overline{m}_\alpha > 0.24$ (red line) and calculating the substitution rate variation pattern for both set. Note that the threshold of 0.24 was chosen such that an equal number for repeat families occur in both sets. This prevents effects due to different sample sizes. Only minor variations between the resulting $\overline{\tau}_\gamma/\overline{m}$ estimates are visible, also reflected by the high correlation coefficient of $r = 0.895$. We thus find basically the same substitution rate pattern regardless of the used subset. From this particular comparison we can also conclude that deviations from the short-burst approximation can be tolerated. Repeat families with a higher σ_α can generally be assumed to have had a longer period of activity and are thus not conform to the underlying model, yet their use seems to have a negligible effect on the final results. In short, the results of our computations are robust with respect to the repeat propagation model. Perhaps more importantly, the signal we determine is independent of the repeats themselves. While repeats provide the data needed to calculate $\overline{\tau}_\gamma/\overline{m}$, not a particular feature of the repetitive elements is calculated but the underlying substitution rate.

6.8. Conservation of $\overline{\tau}_\gamma/\overline{m}$ and its Relation to the GC Isochore Structure

So far, mostly methodological issues and the validation of the approach have been discussed. In this section some new biological insights drawn from the theory are presented. This is accomplished by investigating the conservation of the substitution rate pattern across mammalian species and its relation to the GC isochore structure. Whereas, the GC isochore structure is a common feature to all higher eucaryotic organisms. This structure arises in the GC content, the proportion of the complementary bases guanine and cytosine with respect to the total amount of bases for a given spatial partition of the genome. Like the substitution rate pattern, the GC content is not uniform over the genome, but shows a structure having a similar length scale than $\overline{\tau}_\gamma/\overline{m}$. This structure is called GC isochore structure. Interestingly, for most of the locations the GC content is below 50% and decays exponentially, as shown below.

Let us concentrate on the first issue, the conservation of the substitution rate pattern. We argue that local substitution rate is determined by local sequence content. This conclusion is based on finding an unexpectedly high conservation of the rate pattern both over time and between mammalian species. Consider a counter-assumption: that substitution rate variation is dictated by some global or distant feature, e.g., absolute position on a chromosome, or an external factor affecting the genome in a location-dependent manner. We would then expect any partition γ to have shifted position within or between chromosomes over the course of time, and thus be subjected to varying external influences. When calculating $\overline{\tau}^i_\gamma/\overline{m}$ for older time classes C_i one should get a value representing the average rate to which these older repeats of partition γ have been subjected, resulting in a flattened-out curve. By contrast,

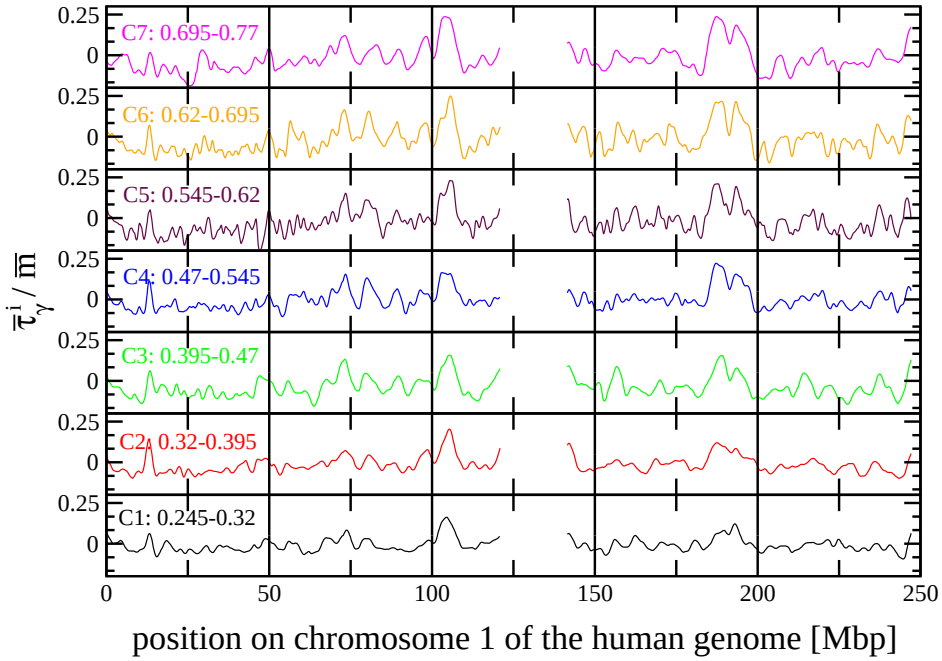

Figure 6.13: A graph showing of the local substitution rate pattern $\overline{\tau}^i_\gamma/\overline{m}$ against genome position of chromosome 1 for the human genome and for the seven time classes ($i = 1, \cdots 7$). Again, due to a lack of sufficient data the centromeric region is left out for the analysis. The conservation of the pattern is apparent from this figure, since prominent features of the curve are preserved during the time course.

younger age classes should produce curves with a more distinct shape. Hence there should be little conservation of $\overline{\tau}^i_\gamma/\overline{m}$ values between time classes. It can be seen from Fig. 6.13 that the above predictions do not hold; the curves derived from older families seem to have a more distinct shape than those derived from newer families. Further, the pattern is clearly conserved: partitions subjected to an above- (below-)average substitution rate tend to stay that way. Given the counter-assumption, it is also expected that lineage-specific rearrangements result in very different $\overline{\tau}^i_\gamma/\overline{m}$ values for homologous partitions on different organisms. We instead find a high conservation, illustrated in Figure 6.14, which compares the $\overline{\tau}^{i=6}_\gamma/\overline{m}$ (age class C_6) curve of human against a reconstruction of that curve using exclusively mouse-derived data. Homologous segments are mapped using the BlastZ alignments provided by the UCSC Browser [166, 169]. In both panels the black curve represents the actual curve for human. The yellow curve represents a mapping of mouse data using the mouse $\overline{\tau}^{i=6}_\gamma/\overline{m}$ values while the red curve is reconstructed from the mouse $\overline{\tau}^{i=2}_\gamma/\overline{m}$ values, derived exclusively from rodent-specific repeat families. A regression of the C_6 reconstructed against actual values results in a correlation coefficient of $r = 0.74$; substituting chimpanzee for mouse results in a correlation coefficient of $r = 0.93$. We also note the distribution of $\overline{\tau}^i_\gamma/\overline{m}$ values is highly conserved between human and mouse for any age class. In short, each prediction following from the counter-assumption is contradicted by the results. Figure 6.13 shows that as we go back in time, the local deviation from the mean substitution rate seems to increase (decrease) in regions where it is already high (low), reflecting an amplifying mechanism that is seem-

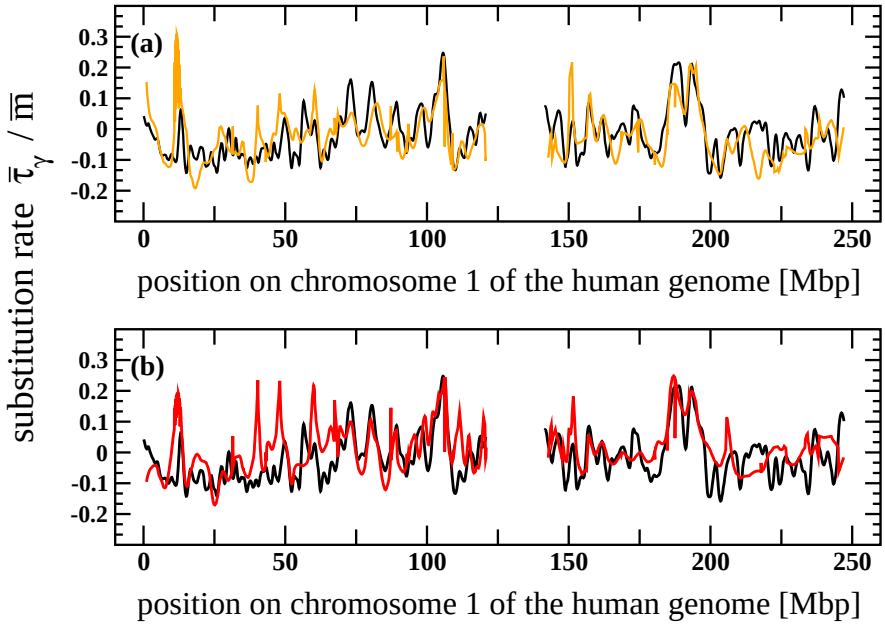

Figure 6.14: In both panels the actual $\overline{\tau}_\gamma^{i=6}/\overline{m}$ curve is shown for the human genome across chromosome 1 (black curves), calculated from repeats inserted between 95 and 108 Myr ago. The yellow curve is the reconstruction derived from mouse repeat data inserted at approximately the same time. Whereas, the red curve is the reconstruction derived from lineage specific mouse repeat data, inserted 49-61 Myr ago.

ingly incompatible with the genome experiencing large-scale sequence rearrangements. These apparently conflicting facts can be reconciled only if local characteristics of the nucleotide sequence are the main cause of variations in substitution rate. The local sequence environment of each partition is conserved, thus not affected, e.g., by any genomic rearrangement, as chromosomal rearrangements occur in blocks significantly larger than this length scale. Consequently, the substitution rate variation is conserved over time and between lineages.

Now, let us consider the second issue, namely the relation of $\overline{\tau}_\gamma/\overline{m}$ to the GC isochore structure and its decay. The matrix q allows us to derive a relationship between local substitution rate and local GC content and to show that the GC content of the mammalian genome will eventually reach an equilibrium value, denoted GC^* following Meuiner and Deuret [170]. Recall that rows and columns of q are ordered corresponding to A, C, G, and T. Using, e.g., Tab. 6.4, p. 99 to assign each $q_1, \cdots, q_6$ to its individual transitions, the full q matrix can be represented by

$$\mathbf{q} = \begin{pmatrix} -(q_1+q_5+q_2) & q_1 & q_5 & q_2 \\ q_4 & -(q_4+q_3+q_6) & q_3 & q_6 \\ q_6 & q_4 & -(q_6+q_4+q_4) & q_3 \\ q_2 & q_5 & q_1 & -(q_2+q_5+q_1) \end{pmatrix}. \quad (6.36)$$

For the following, we are not interested in the time-evolution of each base individually, but of the GC content as a whole. Thus, reduce our description and investigate just the two

probabilities for the GC and the AT content of partition γ,

$$\begin{aligned} p_\gamma^{AT} &= [p_\gamma]_{i=1} + [p_\gamma]_{i=4} \\ p_\gamma^{GC} &= [p_\gamma]_{i=2} + [p_\gamma]_{i=3} \ . \end{aligned} \tag{6.37}$$

In this reduced model, our master equation (6.1) does not change its form, but the vector p_γ in this equation is now replaced by the two-component vector $\hat{p}_\gamma = (p_\gamma^{AT}, p_\gamma^{GC})$. Due to symmetry of q, which is induced by the assumed strand-symmetry it is possible to collapse q to the 2×2 rate matrix of the two-state system:

$$\hat{q} = \begin{pmatrix} -(q_1 + q_5) & q_1 + q_5 \\ q_4 + q_6 & -(q_4 + q_6) \end{pmatrix} \tag{6.38}$$

and equation (6.4) becomes

$$\hat{R}_{\gamma,t} = m_\gamma(t)\ \hat{q} \ . \tag{6.39}$$

Repeating the same steps as in Sec. 6.2 leads to an expression for the temporal and spatial evolution of the GC, as well as the AT content. This allows to calculate the steady state of the GC content in partition γ by setting the left hand side of the two dimensional version of Eq. (6.3) equals zero. Denoting this steady state by GC_γ^*, its value yields

$$\begin{aligned} GC_\gamma^* &= \frac{\left[\hat{R}_{\gamma,t}\right]_{2,1}}{\left[\hat{R}_{\gamma,t}\right]_{1,2} + \left[\hat{R}_{\gamma,t}\right]_{2,1}} = \frac{m_\gamma(t)\ (q_1 + q_5)}{m_\gamma(t)\ \ (q_1 + q_5 + q_4 + q_6)} \\ &= \frac{q_1 + q_5}{q_1 + q_4 + q_5 + q_6} \ . \end{aligned} \tag{6.40}$$

Hence, the equilibrium value of the GC content is independent of γ, and we have

$$GC^* = \frac{q_1 + q_5}{q_1 + q_4 + q_5 + q_6} \ . \tag{6.41}$$

for each γ and for the genome as a whole. Note the implication of Eq. (6.41) when considered in the context of an elevated C_pG dinucleotide substitution rate. The model under discussion does not explicitly account for these elevated rates. However, it has been shown that it implicitly accounts for this rate by returning an elevated estimation of q_6 in proportion with the effect of the C_pG-specific pair transitions. This extra contribution depends on the initial C_pG content of the genome. If the initial C_pG content is increased, q_6 is increased proportionately, hence GC^* is underestimated when the initial C_pG content is particularly high. Applying Eq. (6.41) to the estimations of q yields

$$\begin{aligned} \textbf{human:} \quad & GC^* = 0.324 \\ \textbf{mouse:} \quad & GC^* = 0.349 \quad . \end{aligned}$$

Conservation of q implies that GC^* should be conserved between organisms. In practice our estimates differ because the model does not explicitly account for elevated C_pG substitution rates, as mentioned above.

In order to study the decay of the GC content to GC^* and its relation to the substitution rate pattern, let us define $p_\gamma^{GC,ex}(t)$ to be the difference between the actual GC content of partition γ and the equilibrium value GC^*. This value is called excess GC content. Next, let us look at how the GC content is changing over time on a partition-by-partition basis. Using $\hat{q}$ instead of q we obtain similar to Eq. (6.2), p. 78:

$$\hat{p}_\gamma(0) \;=\; \hat{p}_\gamma(-T)\;\exp\left(\hat{q}\;\overline{m}_\gamma T\right) \tag{6.42}$$

Given $\hat{q}$ from Eq. (6.38), it is straight forward to calculate the (left) eigenvectors and eigenvalues of $\hat{q}$. From there we can find a matrix B such that $\hat{q} = B^{-1}\;\lambda_D\;B$, where

$$\lambda_D = \begin{pmatrix} -\lambda & 0 \\ 0 & 0 \end{pmatrix} \tag{6.43}$$

and

$$\lambda = q_1 + q_4 + q_5 + q_6 \tag{6.44}$$

with 0 and $-\lambda$ being the two eigenvalues of $\hat{q}$. By substituting $\hat{q} = B^{-1}\;\lambda_D\;B$ into Eq. (6.42) and performing some algebraic manipulations we obtain

$$p_\gamma^{GC}(0) \;=\; GC^* + \;\left(p_\gamma^{GC}(-T) - GC^*\right)\;\exp\left(-\lambda\;\overline{m}_\gamma T\right)\,. \tag{6.45}$$

Since $p_\gamma^{GC,ex}(t) = p_\gamma^{GC}(t) - GC^*$ and by substituting this expression into equation (6.45) one arrives at

$$\begin{aligned} p_\gamma^{GC,ex}(0) \;&=\; p_\gamma^{GC,ex}(-T)\;\exp\left(-\lambda\overline{m}_\gamma T\right) \\ &=\; p_\gamma^{GC,ex}(-T)\;\exp\left(-\lambda T\;\overline{m}\;\overline{\tau}_\gamma/\overline{m}\right)\;\exp\left(-\lambda T\;\overline{m}\right)\,, \end{aligned} \tag{6.46}$$

where $\hat{q}T\;\overline{m}\;(1+\overline{\tau}_\gamma/\overline{m})$ is similar to Eq. (6.5), p. 79, but averaged over T. Equation (6.46) therefore manifests the exponential decay toward GC^*. Taking the logarithm of this equation, we obtain the linear relationship

$$\ln p_\gamma^{GC,ex}(0) = \left(\ln p_\gamma^{GC,ex}(-T) - \lambda T\;\overline{m}\right) - \lambda T\;\overline{m}\;\overline{\tau}_\gamma/\overline{m}\,. \tag{6.47}$$

Thus, a logarithmic plot of $p_\gamma^{GC,ex}(0)$ against $\overline{\tau}_\gamma/\overline{m}$ should result in a line with intercept $b = \ln p_\gamma^{GC,ex}(-T) - \lambda T\;\overline{m}$ and slope $s = \lambda T^* = \lambda T\;\overline{m}$. In Fig. 6.15, $\overline{\tau}_\gamma/\overline{m}$ is regressed against the GC content for human and mouse, finding the predicted exponential relation and an apparent convergence value of GC content to the predicted GC^* values. Whereas, in Fig. 6.16 the linear relationship in Eq. (6.47) of $\ln p_\gamma^{GC,ex}(0)$ against $\overline{\tau}_\gamma/\overline{m}$ is shown for human (top panel) and mouse (bottom panel). An almost perfect correlation is found with correlation coefficients as high as $r_s = -0.84$ for human and $r_s = -0.81$ for mouse, significantly higher than previously reported [141, 142]. Note that the subscript in r_s indicates that Spearman's rank correlation coefficient is used, which is robust in the presence of outliers. In the center panel we account for interaction between the generating data by regressing the human $\overline{\tau}_\gamma/\overline{m}$ values against the GC-content values calculated from the inter-repeat sequences. The results are essentially unchanged, with $r_s = -0.81$. Finally, these regressions allow us to estimate the constants b and s:

$$\begin{array}{lll} \textbf{human:} & b = -2.601 \pm 0.002 & s = -7.16 \pm 0.03 \\ \textbf{mouse} & b = -2.724 \pm 0.002 & s = -6.72 \pm 0.02 \end{array} \tag{6.48}$$

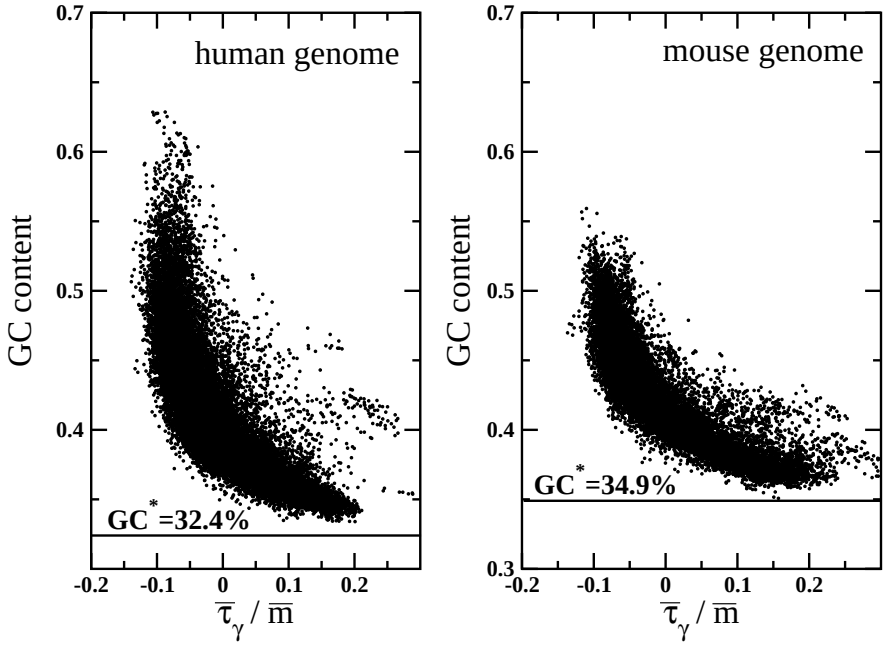

Figure 6.15: GC content versus local substitution rate on the human and mouse genome. The GC content in partition γ was correlated with $\overline{\tau}_\gamma/\overline{m}$, the averaged substitution rate in partition γ. An exponential decay toward the equilibrium GC content GC^* is clearly visible.

It can be seen that the genome-wide GC content is decreasing at approximately the same rate in both human and mouse, showing the expected consistency that validates the main assumptions of our model. If the matrix q were not independent of time and location, or if there was a lineage specific effect, we should have found different rates. The small differences in $s = \lambda T\ \overline{m}$ we still observe is likely due to a C_pG effect. Because of the strength of the correlation between $p_\gamma^{GC,ex}(0)$ and $\overline{\tau}_\gamma/\overline{m}$, one can take the inverse route and apply $\overline{\tau}_\gamma/\overline{m} = (b - \ln p_\gamma^{GC,ex}(0))/s$ to estimate $\overline{\tau}_\gamma/\overline{m}$ from the local GC content.

To summarize, it has been shown that the GC content decays exponentially with the substitution rate as the rate-determining factor. As this factor depends on location, we can directly observe this decay by plotting local GC content against local substitution rate, Fig. 6.15. While we cannot conclude any causal relationship, let us note that if rate variation were the determining factor of GC content variation, then this relationship predicts the formation of an isochore structure when starting with an ancestor genome that had a uniform GC content. Alternatively, GC content could be the sequence characteristic determining substitution rate that we previously argued must exist.

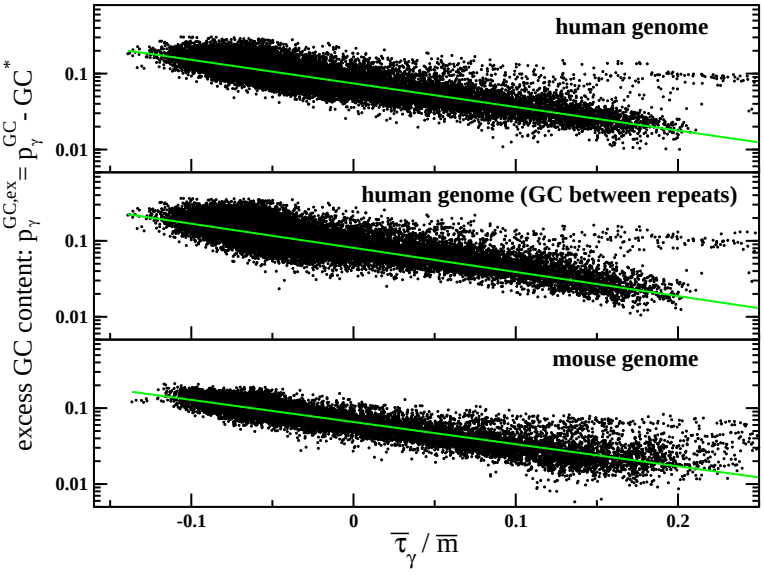

Figure 6.16: A logarithmic plot of the excess GC content $p_\gamma^{GC,ex}$ versus the local substitution rate $\overline{\tau}_\gamma/\overline{m}$ on the human (top panel) and mouse (bottom panel) genome. The graph in the center panel shows again the GC content on the human genome versus local substitution rate. Where the only difference between the upper panel is that the GC content now computed from genome regions between the repetitive elements. In fact, the results are basically the same form the inter-repeat region than for the whole partition. Thereby, the effect we see is not an artefact of the repeats and therefore provides a substantial understanding of the GC isochore structure.

6.9. Possible Cause of the Variation

Before discussing a possible mechanism which is capable to explain the findings above and other results from the literature, a few additional issues about molecular evolution need to be introduced. First, single nucleotide polymorphisms (SNPs) are variations of the DNA at a single nucleotide level and within a population of a species. About 90% of all genetic variation between members of a population are related to SNPs. They play, e.g., an important rôle in the development of certain diseases and are therefore thoroughly studied for designing new drugs. However, the density of SNPs varies within the genome. The major difference between the discussed substitution rate and the SNPs is that substitutions for calculating $\overline{\tau}_\gamma^i/\overline{m}$ must have been fixed in the population, whereas SNP are accounting for substitutions within the population. Second, biased gene conversion (BGC) is attached to the recombination process, where already existing variations between the genomes of the parents are shuffled and passed to the offspring. This process allows to achieve a higher biodiversity for the entire population. Mutations occurring during the recombination may lead to a mismatch (bases on both strands of the double helix are not complementary) at a certain position of the DNA. This mismatch, is fixed with preference to G or C which is termed BGC. Again, the intensity of the recombination process is not uniform over the genome. Finally, the exon density is the amount base pairs for a given spatial partition on the genome corresponding to exons. Exons

are sequences of a gene which can be translated into a protein, therefore is a substantial part of coding DNA which is exposed to selective pressure. The used repetitive elements are of non-coding DNA. However, there is no ultimate evidence that these regions are not under selection. Here, selection refers to the procedure that certain substitutions, especially those in coding regions, may lead to changes which are lethal or causing diseases and are not fixated in the population. There are therefore regions in the genome which are sensitive to substitutions in a sense that changes influences the function of the organism; such changes are suppressed by the evolution. These regions are said to be under selective pressure. Other regions, however, are insensitive to substitutions such that the substitution rate turns out to be higher than in regions with selection. This substitution rate is called neutral.

It has been debated whether the variation in substitution rate and GC content is a product of variations in mutation rates, variation in selective pressure or BGC [147, 170, 148, 171, 172]. In light of previous studies, our results lead to a new conjecture: that substitution rate variation is caused by fluctuations in the efficiency of DNA repair mechanisms, that rate variation drives isochore structure formation and GC decay, and that the decay is in part slowed by BGC. First let us investigate the correlation between $\overline{\tau}^i_\gamma/\overline{m}$ and exon density, SNP density, and recombination rates. After controlling for GC content we find no evidence of a correlation between $\overline{\tau}_\gamma$ and exon density ($r_s = -0.01$ at a p-value of 0.18). Since the exon density can be regarded as a measure for the amount of protein coding regions, this result indicates that $\overline{\tau}_\gamma$ is rather a neutral substitution rate. From a multiple regression of $\overline{\tau}^i_\gamma/\overline{m}$ on SNP density and the deCODE recombination rate [173], we find partial correlation coefficients of $r_s = 0.40$ and $r_s = -0.41$ respectively ($p \ll 10^{-6}$, data size: $N = 2629$). The values of the q matrix imply a high substitution bias towards $GC \to AT$ substitutions, but a stronger bias must exists at the mutation level. Filipski suggests that the efficiency of DNA repair varies along the genome [174], an idea that is consistent with our results and would account for the positive correlation with SNP density. Paired with our previous argument this would imply that the efficiency of the DNA repair mechanism was determined by local sequence content. However, Lipatov et al. have recently argued that a fixation bias must be partly responsible for the variation [172], either in the form of BGC or some unknown selection pressure on neutral DNA. Duret et al. [175] have observed a higher segregation of $AT \to GC$. SNPs, implying a fixation bias for GC pairs. It is difficult to distinguish between the effects of BGC and selection on fixation bias, as BGC is mathematically equivalent to weak directional selection [176], but we observe the following. BGC, the simpler explanation, has the effect of correcting $GC \to AT$ mutations at a rate proportional to the recombination rate. If there is a heavy bias towards $GC \to AT$ mutations, then BGC would eliminate a high percentage of mutations in areas of high recombination, thus accounting for the negative correlation between substitution rate and recombination rate as well as reducing the bias towards $GC \to AT$ substitutions. Continuing with this model, it is tempting to identify the mutational bias reflected in q as both the cause of GC content decay and the sole determining factor of the target GC equilibrium value GC^*. The substitution rate pattern $\overline{\tau}^i_\gamma/\overline{m}$ would then dictate the local rate at which the decay occurs and defines the isochore structure. BGC's tendency to correct GC mutations also implies an effect of BGC on GC content, resulting in the positive correlation between recombination rates and GC content observed

in Meuiner and Duret [170]. Such a model provides a simple explanation for both structural features that is consistent with other studies in the literature.

6.10. Conclusion

In this Chapter a model for the substitution rate variation is formulated, validated, and applied to five mammalian genomes. Consequently a computational method is established which allows us to examine the substitution rate relative to the genome mean in time and location on the genome. Therefore, the method allows to study the rate variation in detail to understand the underlying causes and its relation to other evolutionary and genomic features. Moreover, in quantifying the rate variation it is also possible to calculate ages for various repeat families which has been validated by results presented in other works. The model relies on the assumption that a time and location invariant relative rate matrix q can be introduced. On the other side the entire substitution rate pattern can be absorbed into a single function capturing the time and location dependency of the involved mutation process. This assumption has been validated by observing basically the same matrices q for several different mammalian genomes, where deviations can be explained by the possibility that the methylation state of the genome might have changed after the speciation of the species. With the additional application of a statistical noise reduction technique the underlying rate variation pattern can be extracted. In addition, a method is presented to predict the range over which the substitution rate can be regarded as being roughly constant. This characteristic length scale is about 1 Mb for human and mouse. Finally, it is shown that effects from an elevated C_pG dinucleotide substitution rate can safely be ignored.

As biological implications of the presented theory, the conservation of the substitution rate pattern and its relation to other genomic features such as the GC content have been discussed. The GC content also changes with location to form an isochore structure that appears to be decaying over time [147, 170, 177]. Elucidating the causes of these variations is important in understanding the structure and function of the genome. It has been shown that the pattern of variation in substitution rate is conserved between species and over time. This suggests that local sequence content is the primary determinant of local substitution rates. We also showed that the variation in substitution rate has a precise negative exponential relationship to GC composition. This correlation is considerably stronger than previously reported [141, 142]. An extension of the model allows us to estimate both the equilibrium GC-point to which the mammalian genome is evolving and the rate at which it is progressing to that point. Moreover, it can be seen that these features are also conserved between species. As a whole, we shed considerable new light on the causes of both features as well as providing the most accurate method to date for quickly predicting local substitution rates.

7

Summary

The aim of this thesis is to apply concepts of statistical physics and non-linear dynamics to problems arising in the life sciences. Applying tools and concepts from physics to cope with the complexity of living organisms is mainly triggered by the enormous advance of measurement techniques in molecular biology. Thus, the goal of this endeavor is to build up mathematical models to uncover underlying principles.

In this thesis, the development of theoretical methods and its application to measured data is addressed, where Chapter 2, 3, and 4 solely deals with the development of such methods. More detailedly, the problem of detecting phase synchronization between two non-linear self-sustained oscillating systems is examined in Chapter 2. If there is no adequate model for the underlying oscillators and the coupling between them, one would like to infer phase synchronization on the basis of empirical data. This can only be achieved using an appropriate statistical test procedure which is as process independent as possible. As shown analytically, this is feasible if the mean phase coherence is used as measure for phase synchronization. However, the only restriction on the data generating processes is that they have to satisfy the mixing condition. This restriction is due to the fact that the phase difference of the oscillators converges to a drift diffusion process with respect to the Skorohod metric, which is referred to as functional central limit theorem. From the drift diffusion process, the distribution of the test statistics for phase synchronization is then derived analytically. In fact, this distribution contains two parameters: the mean angular velocity and the diffusion constant. In order to apply the derived test to data, these parameters have to be estimated from the measurements itself. A reliable procedure to estimate the mean angular velocity and the diffusion constant is thus derived. To underline the relevance of the statistical test, its performance on simulated data is discussed. These simulations clearly shows, that the derived test meets the general requirements of a proper statistical test and is in addition powerful to discriminate phase synchronized systems from unsynchronized after the test has achieved its asymptotic accuracy.

Due to the functional central limit theorem the mixing property plays an important rôle in order to derive a test statistic for phase synchronization. However, it is argued in Chapter 3 that mixing of the processes is also necessary to avoid a spurious phase synchronization between independent systems, even in the limit of infinite data. In spectral analysis, a similar effect occurs if the mixing condition is not fulfilled. It is shown, that the power-spectrum is no longer a continuous function, but the presence of delta-distributions arise. Here, the resolvent function of the Frobenius-Perron operator determines this behavior. Namely, poles of the resolvent function which are close to the unit circle are producing pronounced resonances in the power-spectrum. For the bivariate spectral analysis, a loss of mixing results in a spurious coherency. Therefore, mixing is crucial for synchronization, spectral and cross-spectral analysis. A deterministic chaotic system which shows effects that can be explained by a loss of mixing is the Rössler system. An alternative explanation of the observed irregular behavior is the occurrence of finite size effects, since only finite trajectories of the system can be used in a numerical study. To discriminate these two possibilities an approximation to the phase dynamics of the Rössler oscillator is derived. The results obtained from this approximation strongly suggests that the aforementioned irregular behavior is due to finite size effects.

Many real-word networks can be represented by graphs. In Chapter 4, a limit theorem for the degree distribution of growing networks is derived. This result is based on a measure for the statistical dependencies between finite subgraphs of the network. Analogue to mixing of dynamical systems as discussed in Chapters 2 and 3, the asymptotical vanishing of statistical dependencies between the subgraphs is referred to as strong mixing for complex networks. If the decay of these dependencies is sufficiently fast while the network is growing, the degree distribution converges to a scale-rich distribution. Since the conditions to obtain a scale-rich degree distribution are rather strict, the predominate occurrence of scale-free graphs is thus suggested by this limit theorem.

In contrast to the previous Chapters, the developed theoretical methods are also applied to measured data in Chapter 5 and 6. The problem of estimating parameters in ordinary differential equations (ODE) is addressed in Chapter 5. This particular problem is of great importance if only phenomenological models in terms of ODEs are at hand to describe the dynamical behavior of the system. Due to the high degree of complexity, biochemical reactions of intra-cellular processes can only be modeled using such phenomenological models. Here, reaction rates and initial concentrations are unknown parameters. In order to estimate these parameters from measurements, the method of multiple shooting is proposed in Chapter 5. It is shown that this method clearly outperforms the standard approach in terms of stability. Additionally, a mathematical analysis of the method shows that the computational effort is not exploding if rather large systems are considered. Beside the estimation of unknown parameters, multiple shooting can be consulted to select the best model out of a set of alternative models. The chosen application exemplarily shows this procedure, where the phosphoinositide 3-kinase (PI3K) pathway of biochemical reactions is taken into account. Paired with an a priori analysis, it is shown that the current picture of this pathway is incomplete. Motivated by a possible extension which is discussed in the literature, the data can finally be explained by introducing a feed-forward loop to the model. The result

further shows that this feed-forward loop cannot consist of a single protein but rather a small reaction network. The identification of this unknown part of the PI3K pathway needs further experiments to obtain a deeper insight into this important component of cellular signal processing.

The rate of evolution in mammalian DNA is an important, but poorly understood component of genomic structure. Chapter 6 is devoted to the calculation of the substitution rate variation across mammalian genomes. It is confirmed that the substitution rate is not constant over a genome, but fluctuates around the genomic average. It is shown that the characteristic length scale of this fluctuation is about 1×10^6 base pairs. Since the calculation of the substitution rate pattern is based on single species interspersed repeats which entered the genome at different points of time, the temporal evolution of the substitution rate pattern can also be studied. This is possible for the last 150×10^6 years. An interspecies comparison of the substitution rate reveals that the observed pattern is highly conserved, even though the total substitution rate (genomic average) is about a factor of two higher for the rodent lineage. The genome averaged rates at which the individual bases undergo changes are almost identical across the species. This indicates that there is a fundamental process of substitution, at least in the genomes of mammals. Furthermore, it is known that epigenetic changes by methylation of the DNA strongly influences the substitution rate of guanine-cytosine dinucleotide base pairs. This leads to the introduction of nearest neighbor interactions into the proposed model which is used to calculate the substitution rate pattern. However, it is shown by numerical simulations and by the sequence data itself that effects due to these nearest neighbor interactions do not significantly influence the estimate of the substitution rate variation. Besides the variation in the substitution, a secondary structure arises in the genome; the local content of guanine and cytosine base pairs (GC content). It is shown that it is possible to predict the GC content using the substitution rate pattern. Finally, correlations with other genomic features, such as the recombination rate and the exon density leads to new insights in the mechanisms behind the substitution rate variation.

Appendix

A

Effect of Neglecting the Higher Substitution Rate of C_pG Sites

As introduced in Sec. 6.5 a frequently occurring mutation process in the mammalian genome is a neighbor-dependent substitution of C_pG to T_pG/C_pA. In [141], Arndt et al. argue that these substitutions occur at a rate of approximately 40 times larger than the other substitutions. In this Appendix a model extension is derived taking this elevated substitution rate into account. This model is named seven-parameter model and is equivalent to the model proposed by Arndt et al. [153]. Then, it is demonstrated that ignoring the elevated C_pG substitution rate does not substantially affect our results, using the neighbor independent six-parameter model introduced in Sec. 6.2.

In following, it is more convenient to use $p(i;t)$ instead of $[p(t)]_i$ as defined in Section 6.2, allowing us to rewrite Eq. (6.1) and Eq. (6.4) as

$$\begin{aligned} \frac{d}{dt}p(j;t) &= \sum_{i=1}^{4} p(i;t)[R(t)]_{ij} \\ &= \sum_{i=1}^{4} p(i;t)m(t)\ [q]_{ij} \end{aligned} \tag{A.1}$$

Since we are only focusing on the estimation of t_α $\overline{m}(t)$ the partition index γ is dropped. Using the new notation, Eq. (6.2) reads

$$p(j;0) = \sum_{i=1}^{4} p(i;-t_\alpha)\ [Q_\alpha]_{ij}\ , \tag{A.2}$$

where $[Q_\alpha]_{ij}$ is defined in Eq. (6.10). Now, the complete seven-parameter model will be formulated and 4×4 matrices $[Q_\alpha]_{ij}$ are computed using the extended model. This then

enables us to quantify the effect of neglecting the C_pG substitution rates in the six parameter model.

For setting up the seven-parameter model the distribution $p(i,j,k;t)$ is needed, describing the probability that a given chain is in state j given that its left or right neighbor is in state i or k at time t. The conditional distribution $p(j|i,k;t)$ reflects the time evolution of the center base given that the left base i and the right base k are known. It is further assumed that the left base can only interact indirectly with the right base. The joint distribution can therefore be written as

$$p(i,j,k;t) = p_L(i|j;t)\ p(j|i,k;t)\ p_R(k|j;t)\ , \tag{A.3}$$

where the conditional distribution $p_L(i|j;t)$ is the probability of finding base i at the left position given that the center position is occupied by j. The quantity $p_R(k|j;t)$ is defined equivalently for the right position. To study the dynamics of $p(i,j,k;t)$ Eq. (A.3) is differentiated with respect to t and yields

$$\begin{aligned}\frac{d}{dt}p(i,j,k;t) &= \frac{d}{dt}p_L(i|j;t)\ p(j|i,k;t)\ p_R(k|j;t) \\ &\quad + p_L(i|j;t)\ \frac{d}{dt}p(j|i,k;t)\ p_R(k|j;t) \\ &\quad + p_L(i|j;t)\ p(j|i,k;t)\ \frac{d}{dt}p_R(k|j;t)\ . \end{aligned}\tag{A.4}$$

Let $[q]_{ij}$ be the known rate matrix for the single nucleotide substitution process, with its six independent rate parameters $q_1,\ldots,q_6$, and let $q_7 = q_{C_pG}$ be the additional rate of the accelerated C_pG substitutions to either CA or TG (rates which should be equal due to strand symmetry). Setting up the equations that determine the time dependence of $p(j|i,k;t)$, $p_R(k|j;t)$ and $p_L(i|j;t)$ is straightforward if we start from Eq. (A.1) and add just the C_pG related transitions with their special rate q_{C_pG}. We obtain:

$$\begin{aligned}\frac{d}{dt}p_L(i|j;t) &= \sum_{l=1}^{4} m(t)\ [q]_{li}\ p_L(l|j;t) + m(t)\ q_{C_pG}\ (\delta_{4,i}\delta_{3,j} - \delta_{2,i}\delta_{3,j})\ p_L(2|j;t) \\ \frac{d}{dt}p(j|i,k;t) &= \sum_{l=1}^{4} m(t)\ [q]_{lj}\ p(l|i,k;t) + m(t)\ q_{C_pG}\ (\delta_{2,i}\delta_{1,j} - \delta_{2,i}\delta_{3,j})\ p(3|i,k;t) \\ &\quad + m(t)\ q_{C_pG}\ (\delta_{4,j}\delta_{3,k} - \delta_{2,j}\delta_{3,k})\ p(2|i,k;t) \\ \frac{d}{dt}p_R(k|j;t) &= \sum_{l=1}^{4} m(t)\ [q]_{lk}\ p_R(l|j;t) + m(t)\ q_{C_pG}\ (\delta_{1,k}\delta_{2,j} - \delta_{3,k}\delta_{2,j})\ p_R(3|j;t)\ . \end{aligned}$$

Inserting the last three equations into Eq. (A.4) yields the full 64-dimensional master equation for the joint distribution $p(i,j,k;t)$ of the seven-parameter model:

$$\begin{aligned}\frac{d}{dt}p(i,j,k;t) &= \textstyle\sum_{l=1}^{4}\big(m(t)\ [q]_{li}\ p(l,j,k;t) + m(t)\ [q]_{lj}\ p(i,l,k;t) + m(t)\ [q]_{lk}\ p(i,j,l;t)\big) \\ &\quad + m(t)\ q_{C_pG}\ (\delta_{2,i}\delta_{1,j} + \delta_{4,i}\delta_{3,j})\ p(2,3,k;t) \\ &\quad + m(t)\ q_{C_pG}\ (\delta_{2,j}\delta_{1,k} + \delta_{4,j}\delta_{3,k})\ p(i,2,3;t)\end{aligned}$$

$$- 2m(t)\ q_{C_pG}\ (\delta_{2,i}\delta_{3,j} + \delta_{2,j}\delta_{3,k})\ p(i,j,k;t)\ . \tag{A.5}$$

This expression is equivalent to the model formulated in [153].

After setting up the seven-parameter model, the effect of ignoring C_pG-specific transitions can now be studied. The six-parameter model describes the time-evolution of the four components $p(i;t)$, while Eq. (A.5) describes the time-evolution of the 64 component vector $p(i,j,k;t)$. If q_{C_pG} is zero both systems of equations produce identical results. Equation (A.5) then simplifies to Eq. (A.1), a reduction that can be formally achieved by summing over the probabilities associated with the bases flanking the central base

$$p_M(j;t) = \sum_{i,k=1}^{4} p(i,j,k;t)\ . \tag{A.6}$$

This equation describes the procedure to reduce the 64 component vector $p(i,j,k;t)$ to a four component vector $p_M(j;t)$, which is suitable for our purpose. If $q_{C_pG} \neq 0$ then Eq. (A.5) shows a slightly different dynamics. In general $p_M(j;t)$ is not equal to $p(j;t)$ and the reduced description in Eq. (A.1) can only be considered as an approximation of Eq. (A.5). The quality of this approximation depends both on the ratio of q_{C_pG} to the six other rates and on the relative occurrence of C_pG sites on the genome. The effects of this approximation can be examined by the following procedure:

1. Pick a point in the past, say $-t_\alpha$, as the starting point and choose values for the seven transition rates q_1 to q_7.
2. Choose an initial probability $p(i,j,k;-t_\alpha)$.
3. Integrate the system of differential equations in Eq. (A.5) and compute distribution $p(i,j,k;0)$.
4. Use Eq. (A.6) to marginalize $p(i,j,k;-t_\alpha)$, $p(i,j,k;0)$ and obtain $p_M(j;-t_\alpha)$, $p_M(j;0)$.
5. Use $p_M(j;-t_\alpha)$ and $p_M(j;0)$ in Eq. (A.2) to obtain the matrix $[Q_\alpha]_{ij}$.
6. Apply the six-parameter model to estimate t_α $\overline{m}_\alpha$ and q from $[Q_\alpha]_{ij}$ for comparison against the known values as chosen in step 1.

Values of t_α were sampled from the interval $(0,2]$ at fixed-length intervals. For q typical typical values occurring in mammalian genomes are chosen. The four rates $q_1,\ldots,q_4$ relating to transversion substitutions are set to 0.05 and 0.15 for those relating to the two transition substitutions, q_5, q_6. According to Arndt et al. [141] we use $q_7 = q_{C_pG}$ to be equal to 2, which is 40 times higher than the rate at which transversions occur. Next, the initial distributions have to be specified. For simplicity let us assume that the left and right base having the same distribution $p_{RL}(i;-t_\alpha)$. Now, the joint distribution is calculated, allowing each possible value for the center base, thus $p(i,j,k;-t_\alpha) = p_{RL}(i;-t_\alpha)\ p_{RL}(k;-t_\alpha)\ \delta_{j,l}$. Following this we experiment with assigning values to $p_{RL}(i;-t_\alpha)$ in three different ways: first, it is chosen randomly, where the formation of C_pG sites at position one and two, or at position two and

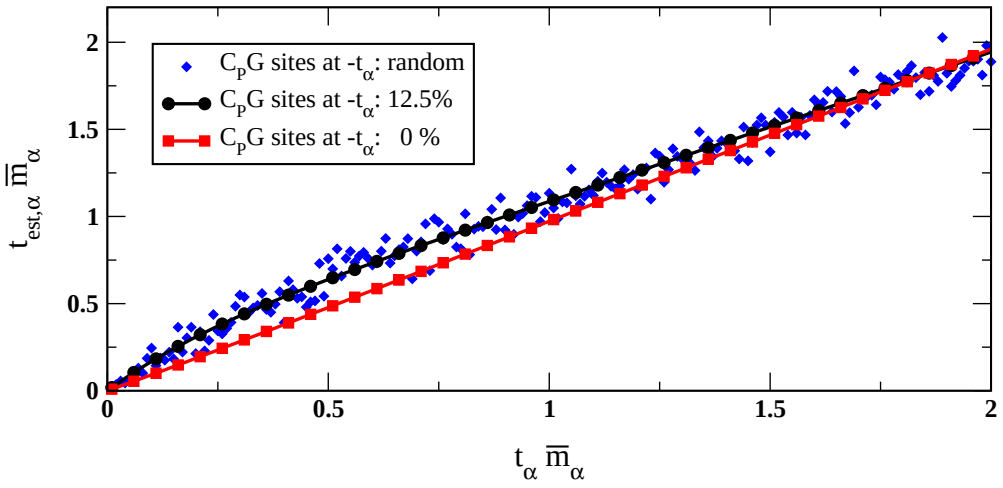

Figure A.1: Validity of the six-parameter model ignoring the C_pG-specific transition rate by comparing the true age $t_\alpha\ \overline{m}_\alpha$ of repeat family α with the estimate $t_{est,\alpha}\ \overline{m}_\alpha$ using the six-parameter model. Three different types of initial probabilities were chosen for the solution of Eq. (A.5) corresponding to a model genome on which C_pG sites occur with a probability of 0%, red squares, 12.5%, black circles, and with a randomly chosen initial probability, blue diamonds.

three, was systematically suppressed, see red squares in Fig. A.1. Second, $p_{RL}(i;-t_\alpha)$ was set to 1/4, so that the probability for a C_pG pair at each possible position is 12.5%, black circles in Fig. A.1, and third, $p_{RL}(i;-t_\alpha)$ was randomly chosen using a uniform distribution, blue diamonds in Fig. A.1.

Figure A.1 shows that for an initial C_pG content of 12.5% the age is mostly overestimated. Thus, neglecting the elevated C_pG substitution rate in the six-parameter model leads to a systematic over-estimation of the repeat age, especially for repeats of intermediate age $t_\alpha\overline{m}_\alpha = 0.5$. On the other hand, if all C_pG sites are initially removed then hardly any effect remains, only a very small deviation from the bisecting line can be observed. In the case of the randomly chosen initial probability, the data points are scattered around the smooth curves of high and zero initial C_pG content. The main message of Fig. A.1 is that ignoring the C_pG-specific transitions leads to a time estimation error up to 20% for an initial C_pG content of 12.5%. However, the actual C_pG content on the human genome is about one percent, but was presumably somewhat higher 120 Myr ago. More importantly the estimate for the age is almost perfect if all C_pG sites are initially removed from the data. Further C_pG sites which are formed during the evolutionary span are not significantly affecting our results. This finding suggests the method to examine the effect an accelerated C_pG decay using the real sequence data by the following procedure: compare the original results with those obtained after excluding all C_pG-sites from the ancestral consensus sequences, as presented in Sec. 6.5.

References

1. J. Knight. Bridging the culture gap. Nature, 419:244–246, 2002.

2. E. Kritikou, B. Pulverer, and A. Heinrichs. All systems go! Nature Cell Biol., 8:S3, 2006.

3. U. Parlitz, A. Pikovsky, M. Rosenblum, and J. Kurths. Schwingung im Gleichtakt. Physik Journal, 5:33–40, 2006. (in german).

4. A.S. Pikovsky, M.G. Rosenblum, and J. Kurths. Synchronization - A Universal Concept in Nonlinear Sciences. Cambridge University Press, Cambridge, 2001.

5. S. Boccaletti, J. Kurths, G. Osipov, D. Valladares, and C. Zhou. The synchronization of chaotic systems. Phys. Rep., 366:1–101, 2002.

6. M.G. Rosenblum, A.S. Pikovsky, and J. Kurths. Phase synchronization of chaotic oscillators. Phys. Rev. Lett., 76:1804–1807, 1996.

7. M.G. Rosenblum, A.S. Pikovsky, and J. Kurths. From phase to lag synchronization in coupled chaotic oscillators. Phys. Rev. Lett., 78:4193, 1997.

8. L. Kocarev and U. Parlitz. Generalized synchronization, predictability, and equivalence of unidirectionally coupled dynamical systems. Phys. Rev. Lett., 76:1816, 1996.

9. L.M. Pecora and T.L. Carrol. Synchronization in chaotic systems. Phys. Rev. Lett., 64:821, 1990.

10. M.G. Rosenblum, J. Kurths, C. Schäfer, and P.A. Tass. Na. In F. Moss and S. Gielen, editors, Handbook of Biological Physics, volume 4 of Neuro-informatics, pages 279–321. Elsevier, Amsterdam, 2001.

11. P. Tass, M.G. Rosenblum, J. Weule, J. Kurths, A. Pikovsky, J. Volkmann, A. Schnitzler, and H.J. Freund. Detection of $n : m$ phase locking from noisy data: Application to magnetoencephalography. Phys. Rev. Lett., 81:3291, 1998.

12. A.G. Rossberg, K. Bartholomé, H.U. Voss, and J. Timmer. Phase synchronization from noisy univariate signals. Phys. Rev. Lett., 93:154103, 2004.

13. F. Mormann, K. Lehnertz, P. David, and C.E. Elger. Mean phase coherence as a measure for phase synchronization and its application to the EEG of epilepsy patients. Physica D, 144:358–369, 2000.

14. W.H. Press, B.P. Flannery, S.A. Saul, and W.T. Vetterling. Numerical Recipes. Cambridge University Press, Cambridge, 1992.

15. C. Allefeld and J. Kurths. An approach to multivariate phase synchronization and its application to event-related potentials. Int. J. Bif. Chaos, 14:417–426, 2004.

16. C. Allefeld and J. Kurths. Testing for phase synchronization. Int. J. Bif. Chaos, 14:405–416, 2004.

17. D. Gabor. Theory of communication. Journal I.E.E., 93:429–457, 1946.

18. B. Boashash. Interpreting and estimating the instantaneous frequency of a signal–part I: Fundamentals; part II: Algorithms and applications. Proc. IEEE., 80:519–568, 1992.

19. A.V. Oppenheim and R.W. Schafer. Digital Signal Processing. Prentice-Hall, Englewood Cliffs, NJ, 1975.

20. O.E. Rössler. An equation for continuous chaos. Phys. Lett., 57A:397–398, 1976.

21. M. Rosenblatt. Markov Processes. Structure and Asymptotic Behavior. Springer, 1970.

22. P. Embrechts, C. Klüppelberg, and P. Mikosch. Modelling Extremal Events for Insurance and Finance. Springer, Berlin, 1997.

23. P. Billingsley. Convergence of Probability Measures. Wiley, New York, 1968.

24. F. Merlevède and M. Peligrad. The functional central limit theorem under the strong mixing condition. Ann. Prob., 28:1336–1352, 2000.

25. P. Billingsley. Probability and Measure. Wiley, 1995.

26. H.R. Künsch. The jackknife and the bootstrap for general stationary observations. Ann. Statist., 17:1217–1241, 1989.

27. M. Peifer, B. Schelter, B. Guschlbauer, B. Hellwig, C.H. Lücking, and J. Timmer. On studentising and blocklength selection for the bootstrap on time series. Biometr. J., 47:346–357, 2005.

28. P.J. Brockwell and R.A. Davis. Time Series: Theory and Methods. Springer, 1987.

29. M.B. Priestley. Spectral Analysis and Time Series. Academic Press, 1989.

30. M. Winterhalder, B. Schelter, J. Kurths, A. Schulze-Bonhage, and J. Timmer. Sensitivity and specificity of coherence and phase synchronization analysis. Phys. Lett. A., 356:26–34, 2006.

31. K. Huang. Statistical Mechanics. Wiley, 1987.

32. A. Lasota and M.C. Mackey. Chaos, Fractals and Noise - Stochastic Aspects of Dynamics. Springer, 1994.

33. D. Ruelle. Thermodynamic Formalism. Addison-Wesley, 1978.

34. D. Ruelle. Resonances of chaotic dynamical systems. Phys. Rev. Lett., 56:405–407, 1986.

35. M. Pollicott. Meromorphic extensions of generalised zeta functions. Invent. Math., 85:147–164, 1986.

36. J.D. Farmer. Spectral broadening of period-doubling bifurcation sequences. Phys. Rev. Lett., 47:179–182, 1981.

37. M. Khodas and S. Fishmann. Relaxation to the invariant density for the kicked rotor. Phys. Rev. E, 62:4769–4783, 2000.

38. S. Fishmann and S. Rahav. Relaxation and noise in chaotic systems. In P. Garbaczewski and R. Olkiewicz, editors, Lecture Notes in Physics, pages 165–192. Springer, 2002.

39. E.J. Hannan. Multiple Time Series. Wiley, 1970.

40. J. Timmer, M. Lauk, W. Pfleger, and G. Deuschl. Cross-spectral analysis of physiological tremor and muscle activity. I. Theory and application to unsynchronized EMG. Biol. Cybern., 78:349–357, 1998.

41. J. Timmer, M. Lauk, S. Häußler, V. Radt, B. Köster, B. Hellwig, B. Guschlbauer, C.H. Lücking, M. Eichler, and G. Deuschl. Cross-spectral analysis of tremor time series. Int. J. Bif. Chaos, 10:2595–2610, 2000.

42. D.M. Halliday, J.R. Rosenberg, A.M. Amjad, P. Breeze, B.A. Conway, and S.F. Farmer. A framework for the analysis of mixed time series/point process data – Theory and application to the study of physiological tremor, single motor unit discharges and electromyograms. Prog. Biophys. molec. Biol., 64:237–278, 1995.

43. T. Yalçınkaya and Y.-C. Lai. Phase characterization of chaos. Phy. Rev. Lett., 79:3885–3888, 1997.

44. J. Crutchfield, J.D. Farmer, N. Packard, R. Shaw, G. Jones, and R.J. Donnelly. Power spectral analysis of a dynamical system. Phys. Lett., 76A:1–4, 1980.

45. Y.-C. Lai, D. Armbruster, and E.J. Kostelich. Intermittency in chaotic rotations. Phys. Rev. E, 62:R26, 2000.

46. A. Pikovsky and M. Rosenblum. Comment on "Intermittency in chaotic rotations". Phys. Rev. E., 64:058203, 2001.

47. Y.-C. Lai, D. Armbruster, and E.J. Kostelich. Reply to "Comment on 'Intermittency in chaotic rotations'". Phys. Rev. E, 64:058204, 2001.

48. V.S. Anishchenko, T.E. Vadivasova, G.A. Okrokvertskhov, and G.I. Strelkova. Correlation analysis of deterministic and noisy chaos. Dyn. Chaos in Radiophys. and Electr., 48:824–835, 2003.

49. V.S. Anishchenko, T.E. Vadivasova, G.A. Okrokvertskhov, and G.I. Strelkova. Correlation analysis of dynamical chaos. Physica A, 325:199–212, 2003.

50. V.S. Anishchenko, T.E. Vadivasova, J. Kurths, G.A. Okrokvertskhov, and G.I. Strelkova. Autocorrelation function and spectral linewidth of spiral chaos in a physical experiment. Phys. Rev. E, 69:036215, 2004.

51. P. Erdős and A. Rényi. On random graphs. Publ. Math. Debrecen, 6:290–297, 1959.

52. P. Erdős and A. Rényi. On the evolution of random graphs. Publ. Math. Inst. Hungar. Acad. Sci., 5:17–61, 1960.

53. E.N. Gilbert. Random graphs. Ann. Math. Stat., 30:1141–1144, 1959.

54. A.-L. Barabási and R. Albert. Emergence of scaling in random networks. Science, 286:509–512, 1999.

55. A.-L. Barabási, R. Albert, and H. Joeng. Mean field theory for scale-free random networks. Physica A, 272:173–187, 1999.

56. R. Albert and A.-L. Barabási. Statistical mechanics of complex networks. Rev. Mod. Physics, 74:47–97, 2002.

57. B. Bollobás, O. Riordan, J. Spencer, and G. Tusnády. The degree sequence of a scale-free random graph process. Random Struct. Algorithms, 18:279–290, 2001.

58. J.F.F. Mendes and S.N. Dorogovtsev. Evolution of Networks: From Biological Net to the Internet and the WWW. Oxford University Press, Oxford, 2003.

59. R. Albert and A.-L. Barabási. Topology of evolving networks: Local events and universality. Phys. Rev. Lett., 85:5234, 2000.

60. F. Liljeros, C.R. Edling, L.A. Amaral, H.E. Stanley, and Y. Aberg. The web of human sexual contacts. Nature, 411:907–908, 2001.

61. G.D. Birkhoff. Proof of a recurrence theorem for strongly transitive systems. PNAS, 17:650–655, 1931.

62. G.D. Birkhoff. Proof of the ergodic theorem. Proc. Natl. Acad. Sci. USA, 17:656–660, 1931.

63. N.H. Bingham, C.M. Goldie, and J.L. Teugels. Regular Variation. Encyclopedia of Mathematics. Cambridge University Press, 1987.

64. L. de Haan. On regular variation and its application to the weak convergence of sample extremes. CWI Tract **32**. Amsterdam, 1970.

65. E.A. Bender. Asymptotic methods in enumeration. SIAM Review, 16:485–515, 1974.

66. R. Albert, H. Jeong, and A.-L. Barabási. Diameter of the World Wide Web. Nature, 401:130–131, 2002.

67. R. Albert, H. Jeong, and A.-L. Barabási. Attack and error tolerance of complex networks. Nature, 406:378–382, 2000.

68. L. Li, D. Alderson, R. Tanaka, J.C. Doyle, and W. Willinger. Towards a theory of scale-free graphs: Definition, properties and implications. arXiv:cond-mat/0501169v2, 2005.

69. R. Tanaka. Scale-rich metabolic networks. Phys. Rev. Lett., 94:168101, 2005.

70. M.E.J. Newman. Assortative mixing in networks. Phy. Rev. Lett., page 208701, 2002.

71. S. Boccaletti, V. Latora, Y. Moreno, and M. Chavez amd D.-U. Hwang. Complex networks: Structure and dynamics. Physics Reports, 424:175–308, 2006.

72. M. Catanzaro, M. Boguñá, and R. Pastor-Satorras. Generation of uncorrelated random scale-free networks. Phys. Rev. E, 71:027103, 2005.

73. U. Alon. Biological networks: the tinkerer as an engineer. Science, 301:1866–1867, 2003.

74. U. Alon. An Introduction to Systems Biology. Chapman & Hall, 2006.

75. A. Wuchty, Z.N. Oltvai, and A.-L. Barabási. Evolutionary conservation of motif and constituents in the yeast protein interaction network. Nature Genetics, 35:176–179, 2003.

76. A.-L. Barabási and Z.N. Oltvai. Network biology: Understanding the cell's functional organization. Nature Rev. Genetics, 5:101–1114, 2004.

77. M.P.H. Stumpf, C. Wiuf, and R.M. May. Subnet of scale free networks are not scale-free: Sampling properties of networks. PNAS, 102:4221–4224, 2005.

78. P.S. Swain, M.B. Elowitz, and E.D. Siggia. Intrinsic and extrinsic contributions to stochasticity in gene expression. PNAS, 99:12795–12800, 2002.

79. J.M. Haugh and D.A. Lauffenburger. Analysis of receptor internalisation as a mechanism of modulating signal transduction. J. Theor. Biol., 195:187–218, 1998.

80. I. Swameye, T.G. Müller, J. Timmer, O. Sandra, and U. Klingmüller. Identification of nucleocytoplasmic cycling as a remote sensor in cellular signaling by data-based modeling. Proc. Natl. Acad. Sci., 100:1028–1033, 2003.

81. M. Kollmann, L. Løvdok K. Bartholomé, J. Timmer, and V. Sourjik. Design principles of a bacterial signalling network. Nature, 438:504–507, 2005.

82. M. Ali, C. Storey, and A. Törn. Applications of stochastic global optimization algorithms to practical problems. J. Optim. Theo. & Appl., 95:545–563, 1997.

83. Z.B. Zabinsky and R.L. Smith. Pure adaptive search in global optimization. Math. Prog., 53:323–338, 1992.

84. J.R. Banga and W.D. Seider. Global optimization of chemical processes using stochastic algorithms. In C.A. Floudas and P.M. Pardalos, editors, State of the Art in Global Optimization, pages 563–583. Kluwer, Dordrecht, 1996.

85. A. Törn, M. Ali, and Viitanen S. Stochastic global optimization: Problem classes and solution techniques. J. Global Optimization, 14:437, 1999.

86. A.H.G. Rinnooy-Kan and G.T. Timmer. Stochastic global optimization methods. Part I: Clustering methods. Math. Prog., 39:27–56, 1987.

87. J.H. Holland. Adaption in natural and artificial systems. MIT Press, Cambridge, MA, 1992.

88. A.L. Ingber. Very fast simulated re-anealing. J. Math. Comp. Modelling, 12:967–973, 1989.

89. J.R. Banga, C.G. Moles, and A.A. Alonso. Global optimization of bioprocesses using stochastic and hybrid methods. In C.A. Floudas and P.M. Pardalos, editors, Frontiers in Global Optimization, pages 45–70. Kluwer, 2003.

90. J. Stoer and R. Bulirsch. Introduction to Numerical Analysis. Springer, 1993.

91. H.G. Bock. Numerical treatment of inverse problems in chemical reaction kinetics. In Ebert K., Deuflhard P., and Jäger W., editors, Modelling of Chemical Reaction Systems, pages 102–125. Springer, 1981.

92. H.G. Bock. Recent advances in parameter identification techniques for ordinary differential equations. In Deuflhard P. and Hairer E., editors, Numerical Treatment of Inverse Problems in Differential and Integral Equations, pages 95–121. Birkhäuser, 1983.

93. H.G. Bock. Randwertproblemmethoden zur Parameteridentifizierung in Systemen nichtlinearer Differentialgleichungen. PhD thesis, Universität Bonn, 1987.

94. D.R. Cox and D.V. Hinkley. Theoretical Statistics. Chapman and Hall, London, 1994.

95. J. Milstein. Fitting multiple trajectories simultaneously to a model of inducible enzyme synthesis. Math. Biosciences, 40:175–184, 1978.

96. K. Schittkowski. Parameter estimation in systems of nonlinear equations. Num. Math., 68:129–142, 1995.

97. K. Schittkowski. Numerical Data Fitting in Dynamical Systems. Kluwer, 2002.

98. J.I. Ardenghi, M.C. Maciel, and A.B. Verdiell. A trust-region approach for solving a parameters estimation problem from the biotechnology area. Appl. Num. Math., 47:281–294, 2003.

99. O. Richter, P. Nörtersheuser, and W. Pestemer. Non-linear parameter estimation in pesticide degradation. The Science of the Total Environment, 123/124:435–450, 1992.

100. J. Timmer, H. Rust, W. Horbelt, and H.U. Voss. Parameteric, nonparametric and parametric modelling of a chaotic circuit time series. Phys. Lett. A, 274:123–134, 2000.

101. A.D. Stribet, P. Rosenau, A.C. Ströder, and R.J. Strasser. Parameter optimisation of fast chlorophyll fluorescence induction model. Math. & Computers in Sim., 56:443–450, 2001.

102. W. Horbelt, J. Timmer, M. Bünner, R. Meucci, and M. Ciofini. Identifying physically properties of a CO_2 laser by dynamical modeling of measured time series. Phys. Rev. E, 64:016222, 2001.

103. H.H. von Grünberg, M. Peifer, J. Timmer, and M. Kollmann. Variations in substitution rate in human and mouse genomes. Phys. Rev. Lett., 93, 2004.

104. H. Kuhn and A. Tucker. Nonlinear programming. In Proceedings of 2nd Berkeley Symposium on Mathematical Statistics and Probabilistics, pages 481–492. University of California Press, 1951.

105. J.R. Leis and M.A. Kramer. The simultaneous solution and sensitivity analysis of systems described by ordinary differential equations. ACM Trans. on Math. Software, 14:45–60, 1988.

106. J.R. Leis and M.A. Kramer. ODESSA-An ordinary differential equation solver with explicit simultaneous sensitivity analysis. ACM Trans. on Math. Software, 14:61–67, 1988.

107. W. Horbelt. Maximum likelihood estimation in dynamical systems. PhD thesis, University of Freiburg, http://webber.physik.uni-freiburg.de/ horbelt/diss/, 2001.

108. W. Horbelt, J. Timmer, and H.U. Voss. Parameter estimation in nonlinear delayed feedback systems from noisy data. Phys. Lett. A, 299:513–521, 2002.

109. H.U. Voss, M. Peifer, W. Horbelt, H. Rust, and J. Timmer. Identification of chaotic systems from experimental data. In G. Gousebet, editor, Chaos and its Reconstruction, pages 245–286. Nova Science Publishers Inc., New York, 2003.

110. E. Hairer, S.P. Nørsett, and G. Wanner. Solving Ordinary Differential Equations I, Nonstiff Problems. Springer, Berlin, 1993.

111. A. Bellen and M. Zennaro. Numerical Methods for Delay Differential Equations. Oxford Science Publications, 2003.

112. K.E. Brenan, S.L. Campell, and L.R. Petzold. The Numerical Solution of Initial Value Problems in Differential-Algebraic Equations. North-Holland, New York, 1989.

113. C.T. Kelly. Iterative Methods for Optimization. SIAM, 1999.

114. C.H. Bischof, A. Carle, G.F. Corliss, A. Griewank, and P. Hovland. ADIFOR: Generating derivative code from Fortran programs. Scientific Programming, 1:11–29., 1992.

115. A. Griewank, D. Juedes, and J. Utke. Alogorithm 755: ADOL-C: A package for the automatic differentiation of algorithms written in C/C++. ACM Trans. on Math. Software, 22:131–167, 1996.

116. C. Bauer, A. Frink, and R. Kreckel. Introduction to the GiNaC framework for symbolic computation within the C++ programming language. J. Symbolic Com., 33:1–12, 2002.

117. R.J. Hanson and K.H. Haskell. Alogorithm 587: Two algorithms for the linearly constrained least squares problem. ACM Trans. on Math. Software, 8:323–333, 1982.

118. J. Stoer. On the numerical solution of constrained least squares. SIAM J. Numer. Anal., 382:282–411, 1971.

119. A.W. van der Vaart. Asymptotic Statistics. Cambridge University Press, 1998.

120. L. Denis-Vidal, G. Joly-Blanchard, and C. Noiret. Some effective approaches to check the identifiability of uncontrolled nonlinear systems. Math. and Computers in Sim., 57:35–44, 2001.

121. K.R. Godfrey and J.J. DiStefano. III. Identifiability of model parameters. In E. Walter, editor, Identification and system parameter estimation, pages 89–114. Pergamon Press, 1987.

122. L. Ljung and T. Glad. On global identifiability for arbitrary model parameterization. Automatica, 30:265–276, 1994.

123. N. Noykova, T.G. Müller, M. Gyllenberg, and J. Timmer. Quantitative analysis of anaerobic wastewater treatment processes: Identifiability and parameter estimation. Biotech. and Bioengineering, 78:89–103, 2002.

124. K.A. Levenberg. A method for the solution of certain nonlinear problems in least squares. Quart. Appl. Math., 2:164–168, 1944.

125. D.W. Marquardt. An algorithm for least-squares-estimation of nonlinear problems in least squares. SIAM J. Appl. Math., 11:431–441, 1963.

126. S. Schuster, M. Marhl, and T. Höfer. Modelling of simple and complex calcium oscillations. Eur. J. Biochem., 269:1333–1355, 2002.

127. U. Kummer, L.F. Olsen, C.J. Dixon, A.K. Green, E. Bornberg-Bauer, and G. Baier. Switching from simple to complex oscillations in calcium signaling. Biophys. J., 79:1188–1195, 2000.

128. D. Hanahan and R.A. Weinberg. The hallmarks of cancer. Cell, 100:57–70, 2000.

129. B. Vogelstein and K.W. Kinzler. Cancer genes and the pathways they control. Nature Medicine, 10:789–799, 2004.

130. L.C. Cantley. The phosphoinositide 3-kinase pathway. Science, 296:1655–1657, 2002.

131. B. Alberts, D. Bray, and J. Lewis. Molecular biology of the cell. Garland, New York, 2002.

132. Y. Choi, J. Zhang, C. Murga, H. Yu, E. Koller, B.P. Monia, J.S. Gutkind, and W. Li. PTEN, but not SHIP and SHIP2, suppesses the PI3K/Akt pathway and induces growth inhibition and apoptosis of myeloma cells. Oncogene, 21:5289–5300, 2002.

133. T.G. Müller and J. Timmer. Fitting parameters in partial differential equations from partially observed noisy data. Physica D, 171:1–7, 2002.

134. T.G. Müller and J. Timmer. Parameter identification techniques for partial differential equations. Int. J. Bif. Chaos, 14:2053–2060, 2004.

135. T. Lohmann, H.G. Bock, and J.P. Schlöder. Numerical methods for parameter estimation and optimal experimental design in chemical reaction systems. Industial and Engineering Chemistry Research, (31):54–57, 1992.

136. D. Faller, U. Klingmüller, and J. Timmer. Simulation methods for optimal experimental design in systems biology. Simulation, 79:717–725, 2003.

137. E.S. Lander et al. Initial sequencing and analysis of the human genome. Nature, 409(6822):860–921, 2001.

138. R.H. Waterston et al. Initial sequencing and comparative analysis of the mouse genome. Nature, 420:520–562, 2002.

139. R. Gibbs et al. Genome sequence of the Brown Norway rat yields insights into mammalian evolution. Nature, 428:493, 2004.

140. K. Lindblad-Toh et al. Genome sequence, comparative analysis and haplotype structure of the domestic dog. Nature, 438:803, 2005.

141. P.F. Arndt, T. Hwa, and D.A. Petrov. Substantial regional variation in substitution rates in the human genome: importance of GC content, gene density, and telomere-specific effects. J. Mol. Evol., 60:748–763, 2005.

142. R.C. Hardison, K.M. Roskin, S. Yang, M. Diekhans, W.J. Kent, R. Weber, L. Elnitski, J. Li, M.J. O'Connor, D. Kolbe, S. Schwartz, T.S. Furey, S. Whelan, N. Goldman, A. Smit, W. Miller, F. Chiaromonte, and D. Haussler. Covariation in frequencies of substitution, deletion, transposition, and recombination during eutherian evolution. Genome Res., 13:13–26, 2003.

143. D.J. Gaffney and P.D. Keightley. The scale of mutational variation in the murid genome. Genome Res., 15:1086–1094, 2005.

144. N.G. Smith, M.T. Webster, and H. Ellegren. Deterministic mutation rate variation in the human genome. Genome Res., 12:1350–1356, 2002.

145. H. Ellegren, N.G. Smith, and M.T. Webster. Mutation rate variation in the mammalian genome. Curr. Opin. Genet. Dev., 13:562–568, 2003.

146. G. Bernardi. The vertebrate genome: isochores and evolution. Mol. Biol. Evol., 10:186–204, 1993.

147. A. Eyre-Walker and L.D. Hurst. The evolution of isochores. Nat. Rev. Genet., 2:549–555, 2001.

148. A. Khelifi, J. Meunier, L. Duret, and D. Mouchiroud. GC content evolution of the human and mouse genomes: Insights from the study of processed pseudogenes in regions of different recombination rates. J. Mol. Evol., 62:745–752, 2006.

149. H.N. Kazazian. Mobile elements: Drivers of genome evolution. Science, 303:1626–1632, 2004.

150. J.W. Fondon and H.R. Garner. Molecular origins of rapid and continous morphological evolution. PNAS, 101:18058–18063, 2004.

151. A. Smit. The origin of interspersed repeats un the human genome. Curr. Opin. Genet. Dev., 6:743–748, 1996.

152. Repeat information was derived from the RepeatMasker Tool http://repeatmasker.org and RepBase library http://www.girinst.org. Human repeat information was extracted by RepeatMasker v. 3.1.2 and RM database version 20051025. Chimp repeat informtion was extracted by RepeatMasker v. 3.1.3, RM database version 20060120. Mouse repeat information was extracted by RepeatMasker v. 3.1.3, RM database version 20050112. Rat repeat information was extracted by RepeatMasker v. 2003/06/19, RM database version 20030619.

153. P.F. Arndt, C.F. Burge, and T. Hwa. DNA sequence evolution with neighbor-dependent mutation. J. Comput. Biol., 10:313–322, 2003.

154. S.M. Ross. Introduction to Probability Models. Academic Press, San Diego, CA, eigth edition, 2003.

155. W. Härdle. Applied Nonparametric Regression. Cambridge University Press, Cambrige, 1990.

156. B.W. Silverman. Spline smoothing: The equivalent variable kernel method. Ann. Statist., 12:898–916, 1984.

157. A. Buja, T. Hastie, and R. Tibshirani. Linear smoothers and additive models. Ann. Statist., 17:453–555, 1989.

158. T.J. Hastie and R.J. Tibshirani. Generalized Additive Models. Chapman and Hall, London, 1990.

159. C.H. Reinsch. Smoothing by spline functions. Num. Math., 10:177–183, 1967.

160. P.J. Green and B.W. Silverman. Nonparametric Regression and Generalized Linear Models. Chapman and Hall, London, 1994.

161. P. Craven and G. Wahba. Smoothing noisy data with spline functions. Num. Math., 31:377–403, 1979.

162. B.W. Silverman. A fast and efficient cross-validation method for smoothing parameter choice in spline regression. J. American Stat. Ass., 79:584–589, 1984.

163. P.F. Arndt, D.A. Petrov, and T. Hwa. Distinct changes of genomic biases in nucleotide substitution at the time of mammalian radiation. Mol. Biol. Evol., 20:1887–1896, 2003.

164. P.F. Arndt and T. Hwa. Regional and time-resolved mutation patterns of the human genome. Bioinformatics, 20:1482–1485, 2004.

165. H. Khan, A. Smit, and S. Boissinot. Molecular evolution and tempo of amplification of human LINE-1 retrotransposons since the origin of primates. Genome Res., 16:78–87, 2006.

166. W.J. Kent, C.W. Sugnet, T.S Furey, K.M. Roskin, T.H. Pringle, A.M. Zahler, and D. Haussler. The human genome browser at UCSC. Genome Res., 12:996–1006, 2002.

167. S. Kumar and S. Subramanian. Mutation rates in mammalian genomes. PNAS, 99:803–808, 2002.

168. P.E. Kloeden. Numerical Solution of Stochastic Differential Equations. Springer, 1992.

169. S. Schwartz, W.J. Kent, A. Smit, Z. Zhang, R. Baertsch, R.C. Hardison, D. Haussler, and W. Miller. Human-mouse alignments with BLASTZ. Genome Res., 13:103–107, 2003.

170. J. Meunier and L. Duret. Recombination drives the evolution of GC-content in the human genome. Mol. Biol. Evol., 21:984–990, 2004.

171. N. Galtier, G. Piganeau, D. Mouchiroud, and L. Duret. GC-content evolution in mammalian genomes: the biased gene conversion hypothesis. Genetics, 159:907–911, 2001.

172. M. Lipatov, P.F. Arndt, T. Hwa, and D.A. Petrov. A novel method distinguishes between mutation rates and fixation biases in patterns of single-nucleotide substitution. J. Mol. Evol., 62:168–175, 2006.

173. A. Kong, D.F. Gudbjartsson, J. Sainz, G.M. Jonsdottir, S.A. Gudjonsson, B. Richardsson, S. Sigurdardottir, J. Barnard, B. Hallbeck, G. Masson, A. Shlien, S.T. Palsson, M.L. Frigge, T.E. Thorgeirsson, J.R. Gulcher, and K. Stefansson. A high-resolution recombination map of the human genome. Nature Genetics, 31:241–247, 2002.

174. J. Filipski. Correlation between molecular clock ticking, codon usage fidelity of DNA repair, chromosome banding and chromatin compactness in germline cells. FEBS Lett., 217:184–186, 1987.

175. L. Duret, M. Semon, G. Piganeau, D. Mouchiroud, and N. Galtier. Vanishing GC-rich isochores in mammalian genomes. Genetics, 162:1837–1847, 2002.

176. T. Nagylaki. Evolution of a finite population under gene conversion. PNAS, 80:6278–6281, 1983.

177. M.P. Francino and H. Ochman. Isochores result from mutation not selection. Nature, 400:30–31, 1999.

Acknowledgements

I am deeply grateful to Prof. Dr. Jens Timmer for introducing me into the fascinating field of reseach at the interface between physics and biology. He offered me the opportunity to experience a dynamic reseach environment. His numerous encouraging hints and vital guidance gave me confidence and support throughout the entire period.

I am sincerely thankful to Prof. Dr. Hans-Hennig von Grünberg for the intensive and stimulating discussions. His open-minded and humorous attitude greatly enriched my work.

I wish to thank Dr. Christian Fleck and Dr. Markus Kollmann for their pleasant assistance and exciting discussions.

For fruitful collaboration I would like to thank

- Björn Schelter and Matthias Winterhalder for the joined work on the statistics for the mean phase coherence and the mixing properties of the Rössler system.
- Dr. John Karro and Prof. Dr. Ross Hardison for the tight collaboration on the quantification and interpretation of the substitution rate variation.
- HD Dr. Ursula Klingmüller and Christian Schröter for the analysis of the PI3K pathway.
- Dr. Eva Balsa-Canto and Dr. Julio Banga for their contributions to the parameter estimation in ODEs.

I am especially grateful to Florian Geier who patiently explained me all the biological details.

A very special thank to all members of Prof. Jens Timmer's group for the nice and pleasant working atmosphere.

For proof-reading I would like to express my great gratitude to Kilian Bartholomé.

I like to thank Franziska Münch for handling all the administrative work.

I am thankful to the "Deutsche Forschungsgemeinschaft" and the "Bundesministerium für Bildung und Forschung" for financial support.

For her patience and unflagging help I am sincerely thankful to Helga Zuccaro.

Last but not least, I would like to thank my family without whom I would never have got this far.